


11-16-2018

Physical Electronic Properties of Self-Assembled 2D and 3D Surface Mounted Metal-Organic Frameworks

Radwan Elzein

University of South Florida, relzein@mail.usf.edu

Follow this and additional works at: <https://scholarcommons.usf.edu/etd>

 Part of the [Condensed Matter Physics Commons](#), [Electrical and Computer Engineering Commons](#), and the [Nanoscience and Nanotechnology Commons](#)

Scholar Commons Citation

Elzein, Radwan, "Physical Electronic Properties of Self-Assembled 2D and 3D Surface Mounted Metal-Organic Frameworks" (2018). *Graduate Theses and Dissertations*.
<https://scholarcommons.usf.edu/etd/8111>

This Dissertation is brought to you for free and open access by the Graduate School at Scholar Commons. It has been accepted for inclusion in Graduate Theses and Dissertations by an authorized administrator of Scholar Commons. For more information, please contact scholarcommons@usf.edu.

Physical Electronic Properties of Self-Assembled 2D and 3D Surface Mounted Metal-Organic
Frameworks

by

Radwan Elzein

A dissertation submitted in partial fulfillment
of the requirements for the degree of
Doctor of Philosophy in Electrical Engineering
Department of Electrical Engineering
College of Engineering
University of South Florida

Major Professor: Rüdiger Schlaf, Ph.D.
Alberto Sagüés, Ph.D.
Shengqian Ma, Ph.D.
Alex Volinsky, Ph.D.
Jing Wang, Ph.D.
Arash Takshi, Ph.D.

Date of Approval:
October 29, 2018

Keywords: Photoemission Spectroscopy, Density of States, Molecular Electronics, Electronic Structures, Thin Films

Copyright © 2018, Radwan Elzein

DEDICATION

I dedicate my doctoral dissertation to my father Fawzi Elzein who served the purpose of education as a school principle and educator for forty-two years, and my mother Layla Siblany, who both supported me throughout the long years to pursue my educational needs. This dissertation certainly would not have been possible without the love, trust, and encouragement of my parents. I would like to extend this dedication to my family, my wife, Dr. Rasha Khalife, and my lovely daughter, Roselle Elzein.

ACKNOWLEDGMENTS

I would like to thank my major advisor Prof. Rüdiger Schlaf for his genuine research ideas, kind support, and insightful guidance, Prof. Shengqian Ma, and Prof. Inna Ponomareva for their collaboration. I am thankful to the chair of my dissertation defense, Prof. Anna Pyayt, and my committee members, Prof. Alberto Sagüés, Prof. Shengqian Ma, Prof. Jing Wang, Prof. Arash Takshi, and Prof. Alex Volinsky for their research inputs and their time spent to read my dissertation. A special appreciation to the graduate school for the dissertation fellowship award, and to Prof. Thomas Weller and the judging faculty members of Electrical Engineering Department for the teaching excellence award.

I would like to thank Prof. Weller, Prof. Wang, Prof. Andrew Hoff, and Dr. Alexandro Castellanos for the teaching assignments. I would like to thank the director of Nanotechnology Research and Education Centre, Mr. Robert tuffs, Dr. Yusuf Emirov, Mr. Richard Everly, Dr. Jay Bieber, and Dr. Abishek Dey for their technical supports during my teaching duties and research time.

I would like also to thank Dr. Sam Perez, Dr. Juan Castro, and Mrs. Shraddha Pandey as teaching colleagues for their cooperation throughout the teaching assignments. A special thanks to all former members at the Surface Science Laboratory, foremost Dr. Jhon Figaro, Dr. Zhi Li, Dr. Michael Schaefer, Dr. Eric Tridas, and Dr. Matt Wolak for their tremendous collaborations and professional work relationships, and to my colleagues at the college of engineering and science departments at USF.

TABLE OF CONTENTS

LIST OF TABLES	iii
LIST OF FIGURES	iv
ABSTRACT.....	ix
CHAPTER 1: INTRODUCTION.....	1
1.1 Introduction.....	1
1.2 Dissertation Outline	4
1.3 Charge Transfer and Electronic Properties of MOFs	5
CHAPTER 2: SURFACE MOUNTED METAL-ORGANIC FRAMEWORKS.....	7
2.1 Overview.....	7
2.2 SURMOF Synthesis.....	7
2.2.1 Self-Assembly of Monolayers	7
2.2.2 SURMOFs Synthesis	10
2.3 SURMOF Preparation	11
CHAPTER 3: EXPERIMENTAL METHODOLOGY	13
3.1 Incubation Procedure	13
3.2 Photoemission Spectroscopy	14
3.2.1 Physical Principle.....	14
3.2.2 Photoemission Process.....	17
3.2.3 The Electron Mean Free Path	18
3.3 X-ray Photoelectron Spectroscopy (XPS)	20
3.3.1 Basic Principles of X-ray Photon Generation.....	20
3.3.2 Spectrometer	21
3.4 Low Intensity X-ray Photoemission Spectroscopy (LIXPS).....	23
3.5 Ultraviolet Photoemission Spectroscopy (UPS).....	24
3.6 Inverse Photoemission Spectroscopy (IPES).....	26
3.7 UHV Multi-Chamber Analysis System	27
3.8 Experimental Variability of Photoemission Measurements	29
CHAPTER 4: ADVANCED PHOTOEMISSION SPECTROSCOPY INVESTIGATIONS WITH DFT CALCULATIONS ON THE SELF-ASSEMBLY OF 2D METAL- ORGANIC FRAMEWORKS NANO THIN FILMS	31
4.1 Abstract.....	31
4.2 Introduction.....	32
4.3 Experimental and Simulation Sections	35

4.3.1	Materials	35
4.3.2	Sample Preparation	35
4.3.3	DFT Calculations on the Electronic Structure	38
4.4	Results.....	38
4.4.1	XPS Measurements.....	38
4.4.2	LIXPS, UPS, and IPES Measurements.....	44
4.5	Discussion.....	47
4.6	Conclusion	55
4.7	Acknowledgments	55
CHAPTER 5: ENERGY LEVEL ALIGNMENTS AND MODIFICATION OF INTERFACIAL ELECTRONIC STRUCTURES OF 2D AND 3D SURMOFS.....		56
5.1	Abstract.....	56
5.2	Introduction.....	57
5.3	Experimental Section.....	60
5.3.1	Materials: MOF Materials and Synthesis	60
5.3.2	Deposition Technique	60
5.3.3	In-situ Film Preparation	61
5.3.4	Direct and Inverse PES System	61
5.3.5	2D MOF Experiment	62
5.3.6	3D MOF Experiments.....	62
5.4	Results and Discussion	65
5.4.1	Work Function Measurements by LIXPS.....	65
5.4.1.1	Work Function Measurements of 2D SURMOFS.....	65
5.4.1.2	Work Function Measurements of 3D SURMOFS.....	66
5.4.2	UPS and IPES Measurements.....	70
5.4.2.1	Valence and Conduction Bands of 2D SURMOFS.....	71
5.4.2.2	Energy Band Diagram of 2D SURMOFS	74
5.4.2.3	Valence and Conduction Bands of 3D SURMOFS.....	76
5.4.2.4	Energy Band Diagram of 3D SURMOFS	81
5.4.3	Interfacial and Surface Chemistry Characterizations	83
5.4.3.1	XPS of 2D SURMOFS.....	83
5.4.3.2	XPS of 3D SURMOFS.....	88
5.4.4	Crystal Structure Characterization.....	94
5.4.4.1	Grazing-Incidence X-ray Scattering of 2D MOFS.....	94
5.4.4.2	Grazing-Incidence X-ray Scattering of 3D MOFS.....	96
5.5	Conclusion	98
5.6	Acknowledgments	99
CHAPTER 6: CONCLUSIONS AND FUTURE OUTLOOK.....		100
6.1	Conclusions.....	100
6.2	Future Outlook.....	101
REFERENCES		103
APPENDIX A: COPYRIGHT PERMISSIONS.....		111

LIST OF TABLES

Table 1	Comparison between the resultant work function values from LIXP-, IPE, and UP-spectra measurement of 2D and 3D SURMOFs obtained from Exp A (S1-S4), and Exp B (S1-S3)	69
---------	---	----

LIST OF FIGURES

Figure 1	Scheme of SAM of alkanethiolates designed on a gold surface.....	10
Figure 2	Schematic representation for the synthesis and formation of the 2D and 3D MOFs	11
Figure 3	(a) Schematic diagram for the SURMOF growth sequence on functionalized Si surface by repeated immersion cycles in the metal ion solution, followed by L1 or L2 incubation to construct 2D MOF film (II), by incorporating pillaring linkers P1 or P2, a 3D thin film can be built	12
Figure 4	Sketch of typical direct PES setup with two light sources of X-ray gun and He I-UV discharge lamp	15
Figure 5	Sketch showing the energy level relations in PE process produced when photons impinged on the sample, producing kinetic energy distribution shifted by photons of energy $\hbar\nu$	16
Figure 6	Sketch of typical inverse PES setup with electron gun and photon detector	17
Figure 7	Sketch of the PES as a three-step process: 1) Photoexcitation of electrons, 2) transport to the surface with production of secondary electrons, 3) penetration the surface and escape into the vacuum.....	18
Figure 8	Electron mean free path as their function of their kinetic energy for various metals	19
Figure 9	Principle of operation.....	21
Figure 10	XPS survey spectra of sputtered Au film showing the count rate of photoelectrons as a function of binding energy	22
Figure 11	Au 4f core level XPS spectra of sputtered Au film	23
Figure 12	LIXPS spectra of sputtered clean Au film	24
Figure 13	The characteristic of high-resolution UP-spectrum of Au surface showing the secondary edge cutoff at high binding energy, the inelastic scattered electrons, valence band structure, and fermi level positioned at 0 eV	26

Figure 14	IPES of Au film showing the onset of conduction band state coincides with the fermi level	27
Figure 15	Simplified schematic of the UHV multi-chamber analysis system used for direct and inverse PES measurements on SURMOF	28
Figure 16	The multi-chamber deposition and characterization systems	28
Figure 17	Schematic depiction of the growth sequence: MOF films were grown in three incubation cycles on a MP SAM-terminated gold substrate	37
Figure 18	Computed structures of MOF molecules connected to Cu paddle wheels	38
Figure 19	C 1s, N 1s, O 1s, Au 4f, S 2p, and Cu 2p core level XPS spectra measured before and after step-by-step incubation on the functionalized Au substrate (A) in the $\text{Cu}(\text{NO}_3)_2$ solution, then in the TCPP solution for three cycles sequentially, (B) in both the $\text{Cu}(\text{NO}_3)_2$ and the TCPP solution for three cycles sequentially, and (C) only in a TCPP solution for two cycles	43
Figure 20	LIXPS and UP spectra before and after step-by-step incubation of sputter cleaned Au functionalized substrate in: (A) in the metal ion $\text{Cu}(\text{NO}_3)_2$ then in the organic ligands TCPP for three cycles sequentially, (B) in both the metal ion and the organic ligand solution for three cycles sequentially, and (C) only in a TCPP solution for two cycles	46
Figure 21	DOS comparison between the experimental and computational results	48
Figure 22	DOS comparison between the experimental UPS, IPES, and computational results	49
Figure 23	Computed structure of CuTCPP connected to Cu paddle wheels: a) HOMO orbital with spin-up, b) HOMO orbital with spin-down, c) LUMO orbital with spin-up, and d) LUMO orbital with spin down	50
Figure 24	Electronic structure of the interface of the MOF (CuTCPP) 2D thin film grown on Au functionalized surface as determined from the UP-, IPE- and LIXP-spectra measurements	52
Figure 25	SEM image of MOF thin film after third immersion cycle	53
Figure 26	FIB image of MOF thin film after the third immersion cycle	54
Figure 27	Out-of-plane GIXRD of MOF thin film showing (002) and (003) (top spectrum diffractions assumed from the MOF, and SAM respectively	54

Figure 28	Schematic depiction of idealized 2D and 3D SURMOF growth sequence in a glove box: Films were grown by incubation on Mpy SAM-terminated Au surfaces	64
Figure 29	LIXPSa was measured before (single lines) and LIXPSb after (dashed line) UPS measurements after incubation of the functionalized Au surface in: Cu(OAc) ₂ , and then in the corresponding organic ligand or pillaring linker solutions	66
Figure 30	LIXPSa was measured before (single lines) and LIXPSb after (dashed line) UPS measurements after incubation of the functionalized Au surface in: Cu(OAc) ₂ , and then in the corresponding organic ligand or pillaring linker solutions	68
Figure 31	Comparison between the resultant work function values from LIXP-, IPE, and UP-spectra measurement of 2D and 3D SURMOFs obtained from Exp A (S1-S4), and Exp B (S1-S3).....	70
Figure 32	UP- and IPE spectra of 2D SURMOFs for four different samples grown on prefunctionalized Au surfaces.....	73
Figure 33	Electronic structures at the interface of Exp A	74
Figure 34	Electronic structures at the interface of Exp A	76
Figure 35	UP- and IPE spectra of 3D MOF films showing the HOMO and LUMO regions after third incubation cycle located above and below Fermi edge, respectively	77
Figure 36	UP spectra of 3D SURMOF thin film of Exp B: S1	78
Figure 37	UP spectra of 3D SURMOF thin film of Exp B: S2.....	79
Figure 38	UP spectra of 3D MOF thin film in Exp B: S3.....	80
Figure 39	Energy band diagram of 3D MOF thin film of Exp B: S1, (Metal ion: Cu(OAc) ₂ , Organic ligand: TCPP, Pillaring linker: Pz) grown on Au prefunctionalized surface as determined from the UP-, IPE- and LIXP-spectra measurements	81
Figure 40	Energy band diagram of 3D MOF thin film of Exp B: S2, (Metal ion: Cu(OAc) ₂ , Organic ligand: TCPP, Pillaring linker: Bipy) grown on Au prefunctionalized surface as determined from the UP-, IPE- and LIXP-spectra measurements	82
Figure 41	Energy band diagram of 3D MOF thin film of Exp B: S3, (Metal ion: Cu(OAc) ₂ , Organic ligand: CoTCPP, Pillaring linker: Bipy) grown on Au prefunctionalized surface as determined from the UP-, IPE- and LIXP-spectra measurements	82

Figure 42	Au 4f, C 1s, and Cu 2p core level XPS spectra of 2D SURMOF measured after incubation the prefunctionalized Au substrate in the Cu(OAc) ₂ solution, then in the corresponding organic ligand solution for three to six cycles sequentially	85
Figure 43	S 2p core level XPS spectrum measured after incubation the Au substrates in 4-mercaptopyridine solution	86
Figure 44	N 1s, and O 1s core level XPS spectra of 2D SURMOF thin film measured after incubation the prefunctionalized Au substrate in the Cu(OAc) ₂ solution, then in the corresponding organic ligand solution for three to six cycles sequentially	87
Figure 45	Au 4f, C 1s, and Cu 2p core level XPS spectra of 3D SURMOF thin film measured after incubation the prefunctionalized Au substrate in the Cu(OAc) ₂ solution, then in the corresponding organic ligand solution (TCPP) with the incorporation of pillaring linker solution (Pz) for three cycles sequentially	89
Figure 46	N 1s, and O 1s core level XPS spectra of 3D SURMOF measured after incubation the prefunctionalized Au substrate in the Cu(OAc) ₂ solution, then in the corresponding organic ligand solution (TCPP) with the incorporation of bridging ligand solution (Pz) for three cycles sequentially	90
Figure 47	Au 4f, C 1s, and Cu 2p core level XPS spectra of 3D SURMOF thin film measured after incubation the prefunctionalized Au substrate in the Cu(OAc) ₂ solution, then in the corresponding organic ligand solution (TCPP) with the incorporation of pillaring linker solution (Bipy) for four cycles sequentially	91
Figure 48	N 1s, and O 1s core level XPS spectra of 3D SURMOF thin film measured after incubation the prefunctionalized Au substrate in the Cu(OAc) ₂ solution, then in the corresponding organic ligand solution (TCPP) with the incorporation of bridging ligand solution (Bipy) for three cycles sequentially	92
Figure 49	Au 4f, C 1s, and Cu 2p core level XPS spectra of 3D SURMOF measured after incubation the prefunctionalized Au substrate in the Cu(OAc) ₂ solution, then in the corresponding organic ligand solution (CoTCPP) with the incorporation of bridging ligand solution (Bipy) for three cycles sequentially	93
Figure 50	N 1s, and O 1s core level XPS spectra of 3D SURMOF thin film measured after incubation the prefunctionalized Au substrate in the Cu(OAc) ₂ solution, then in the corresponding organic ligand solution (CoTCPP) with the incorporation of pillaring linker (Bipy) for three cycles sequentially	93
Figure 51	Grazing-incidence in-plane X-ray scattering of 2D MOF thin film of Exp A, S4	95

Figure 52	(a) Grazing-incidence out-of-plane X-ray scattering of 2D MOF film of Exp A, S4.....	95
Figure 53	Projections of the expected crystal structure of the 2D MOF thin film (Exp A, S4) on the (a) ab plane, and (b) ac plane.....	96
Figure 54	(a) Grazing-incidence (a) in-plane, and (b) out-of-plane X-ray scattering of 3D SURMOFs of Exp B, S1, S2, and S3.....	97
Figure 55	Projections of the expected crystal structure of the 3D MOF thin film (Exp B, S2) on the (a) ab plane, and (b) ac plane.....	97
Figure 56	Projections of the expected crystal structure of the 3D MOF thin film (Exp B, S3) on the (a) ab plane, and (b) ac plane.....	98

ABSTRACT

Metal-organic frameworks stand at the frontiers of molecular electronic research because they combine desirable physical properties of organic and inorganic components. They are crystalline porous solids constructed by inorganic nodes coordinated to organic ligands to form 1D, 2D, or 3D structures. They possess unique characteristics such as ultrahigh surface area crystal lattices up to $10000 \text{ m}^2\text{g}^{-1}$, and tunable nanoporous sizes ranging from 0.2 to 50 nm. Their unprecedented structural diversity and flexibility beyond solid state materials can lead to unique properties such as tailorable electronic and ionic conductivity which can serve as interesting platforms for a wide range of electronic applications from photonics, sensors, and energy harvesting/storage devices such as photovoltaics, thermoelectrics, supercapacitors to data storage systems like memristors.

Despite the significant growth of MOF materials during the past two decades, the fundamental understanding of the resultant electronic and ionic structures at the interface of these hybrid materials are still largely unexplored, and the lack of these properties are the basic requirements for elucidating the physics and chemistry of the devices—The exquisite role of physical electronic properties is crucial for the construction of energy band diagrams of MOF thin films, and is key to achieve further advancement in the development of elaborated devices that require tunability and control over functionality. With this motivation, powerful surface science techniques (e.g. direct and inverse photoemission spectroscopy) have been engaged in this dissertation, which provided useful guidelines to access and study the electronic and chemical structures (e.g. valence and conduction bands, and core electrons) at the internal interface of the

individual hybrid constituents of MOF films. This is achieved using a combination of low intensity X-ray photoelectron spectroscopy (LIXPS), ultraviolet photoelectron spectroscopy (UPS), X-ray photoelectron spectroscopy (XPS), and inverse photoelectron spectroscopy (IPES). Furthermore, the density of states obtained from DFT calculations agreed well with the photoemission spectra measurements of the fabricated 2D MOF thin film. Energy level alignment was achieved by judicious selection of various organic ligands in 2D MOF architectures, whereas further incorporation of various pillaring linkers in the 3D MOFs have modified the HOMO and LUMO energy levels as suitable conducting medium for hole or electron transport.

The fundamental study delivered in this dissertation gives a unique feedback by tailoring the electronic properties of the fabricated 2D to 3D MOF thin films. These crucial properties at the interface offer very important understanding and breakthrough in MOFs as functional and tunable electronic materials.

CHAPTER 1: INTRODUCTION

1.1 Introduction

Since the prime examples of electronic devices by about 1943 such as vacuum-tube electronics, solid-state amplifiers, oscillators, and the technology could be advanced if controlling the conductivity of other elaborated devices was achieved[1]. It was until December 1947, when a solid-state inorganic transistor was discovered at Bell Laboratories by Shockley Bardeen, and Brattain enabling the production of electronic components on a millimeter scale utilizing electron currents in doped semiconductor crystals with reservoirs of electrons (n-type), or holes (p-type) that can execute the useful tasks accomplished by vacuum tubes. Since then, research and advancement in digital electronics are strongly linked to Moore's law resulting in a reduction in size but increase of physical complexity governing devices down to 10 nm in size in 2018. However, Moore's foresaw the rate of progress would reach saturation due to physical size limitation because inorganic semiconductors are optimized to the edges of the theoretical limits performance that is governed by quantum uncertainties to make transistor hopelessly unreliable[2] and expected to end in 2025[2-5] and the International Roadmap For Devices and Systems suggested the exploration of alternative routes to the device improvement via heterogenous integration of new technologies to enable a new "More Moore" scaling paradigm, and "beyond CMOS" technology based on novel materials and physics.

Molecular electronics[6-9] is conceptually different from conventional solid-state semiconductor electronics[10] can overcome the critical limits of miniaturization of electronic components and have attracted a growing interest since the discovery of electron tunneling through

an organic monolayer by Kun and Mobius in 1971[11], followed by gedankenexperiment of the molecular rectifying diodes by Aviram and Ratner in 1974[12] by using molecular orbital calculations that show a molecular system comprising donor-spacer-accepter structure allow electron transfer under external electric field which exhibits similar behavior of the p-n junction of a solid state electronic device. Hence after, discoveries within molecular electronic field reporting molecular-scale devices form single molecules to monolayers have elaborated from this philosophy.

Metal-organic frameworks witnessed a growth for the last two decades as attractive candidate for solid-state semiconductors. The benefits behind MOFs considered as emerging new class of unique electronic/photonic materials because they take advantage of conventional organic and inorganic semiconductors in addition to the ordered nanoporous solids that can be doped to alter the ionic or conductive properties of these materials. Referring back to Richard Feynman's statement in 1959 that "there's plenty of room at the bottom", henceforth by exploiting the extremely large surface area and the tunable pore size ranging from 0.2 to 50 nm, can open up opportunities for multidisciplinary scientific research such as discovery of their electronic and ionic properties at the interface, which lead to study their novel electronic transport phenomena which can be realized in various technological devices requiring tunability and functionality.

The advancement and development of organic semiconductive materials and the realization of successful molecular electronic devices such as organic field effect transistors, electroluminescent devices, solar cells, sensors, memories, and thermoelectrics started from their basic study of their physical electronics at the metal/organic/metal interfaces[13] because they have strong impact on the electrical properties. Despite the significant growth of MOF materials and applications, their physical electronic property at the interface are still largely unexplored. The

role of these electron properties is essential for the construction of energy band diagrams of SURMOFs, which can reveal important feedback about the growth process at the interface, and the scientific foundation of metallosupramolecules to wire electronic devices. Hence, powerful surface science techniques such as photoemission spectroscopy are engaged in this dissertation which provided useful guidelines to access and study the band energy levels which is essential of semiconductor device performance. The structure of most MOFs lacks a delocalized electronic structure either through bond delocalization or by π stacking. For this reason, they act as insulators. However, for applications that require electronic transport, it is essential to employ what properties are for organic materials that enable to conduct electricity. The choice of porphyrin molecules as conductive organic ligands that have small band gap values is an important condition to sustain electrical conductivity, whereas ligands with large band gaps will impart insulating properties. For certain applications, the porphyrin ligand can also exist in radical anion or cation form, and redox effective atoms can be used to dope the materials and perhaps can increase the number of charge carriers and therefore improve the conductivity.

Among a variety of organic conductive ligands presented in literature,[14-16] porphyrin molecules[17, 18] were chosen in this dissertation as attractive candidates in building conductive MOF nano thin films on functionalize Au surfaces due to their diverse rigid molecular structures, large physical dimensions, functionalization, tunability, metalation core, stability, and excellent host for guest confinements within the pores. They can form nanoarchitectures with two distinct conductivity states. In turn, SURMOFs based on porphyrin can be employed in wide variety of molecular nanoelectronic applications due to the important characteristics of their semiconductive and redox properties which compromise π - cation radicals and multiple cationic states and its capability to transport and store charges for extended periods. In this work, porphyrin paddlewheel

frameworks were synthesized by Liquid-phase epitaxy (LPE) using free base and metalated conductive organic ligands (5,10,15,20-tetrakis(4-carboxyphenyl) porphyrin) MTCPP (M= Cu, Co, or Ni), and paddlewheel Secondary Building Units (SBU) based on $\text{Cu}(\text{NO})_3$ and $\text{Cu}(\text{OAc})_2$ were incorporated to construct 2D SURMOF. Whereas, further integration of various organic pillaring linkers such as Pyrazine (Pz) or 4,4'-Bipyridine (Bipy) between the 2D frameworks led to the generation of 3D SURMOFs with remarkable change in electronic properties. Eventually, the information obtained from the physical electronic experiments can be employed in the design of molecular electronic devices such as field effect transistors, photovoltaics, sensors, and memristors.

1.2 Dissertation Outline

This dissertation is focused on gaining a comprehensive understanding of the electronic structures and the energy level alignment of the fabricated MOF thin films and it is structured as follows:

Chapter 1 discusses the research motivation of conductive MOFs as potential candidate for electronic devices. This chapter highlights some of conductive MOF materials reported in literature and describes the significance of photoemission study on porphyrin-based MOFs.

Chapter 2 describes the mechanism behind the self-assembly of monolayers, as well as 2D and 3D metal-organic framework thin films on suitable functionalized wafer surfaces.

Chapter 3 describes the incubation procedure and the self-assembly of the SAM, and that of the MOFs, and focuses on theoretical, and experimental methodologies behind the electronic structure characterizations by direct and inverse PES that gave a direct access to the energy band diagrams of the investigated materials. The multichamber analysis system was leveraged for the PES investigations of the targeted materials.

Chapter 4 discusses the direct and inverse PES investigations of self-assembly of 2D MOF thin film. The physical electronic structures of frontier energy levels were obtained and agreed well with DFT calculations. The growth at the interface of multilayers was investigated by XPS. The PES demonstrated sustained electronic properties as the MOF layers grow in thicknesses.

Chapter 5 discusses the HOMO and LUMO energy level alignments at the 2D and 3D SURMOFs' interface. The electronic structures particularly the resultant transfer band gaps were changed by various metalloporphyrin based ligands as demonstrated in 2D MOF thin films, and by incorporating pillaring linkers with different length, a further tuning of the transfer band gap was observed in 3D MOF thin films.

Chapter 6 summarizes the findings behind the physical electronic properties of MOF thin films as functional electronic materials as presented in this study and proposing the future work.

1.3 Charge Transfer and Electronic Properties of MOFs

A comprehensive understanding of the physical electronic properties of MOF thin films can provide a useful guideline for the design and performance of the chosen material as a suitable candidate for specific devices. Hence, an access to energy band diagrams, opens up avenues for new physical applications. Grau-Crespo et al. carried out a theoretical study through band structure calculations on metal substitution in porphyrin-based MOF, and found out that the control of frontier orbital positions enables tuning the bandgaps in a favorable range (2.0 to 2.6 eV) for efficient absorption of solar light which is important for solar-fuel production.[19]

Tuning the interfacial physical electronic properties can achieve promising energy level adjustments between the heterostructure interface of MOFs, and device metal electrodes with suitable hole or electron transport layers that can facilitate efficient charge carrier flow, and this can enhance the light emission, absorption, and charge retention in molecular electronic devices.

Knowing the additional ionic properties of MOFs can open the field for modern solid state electrochemical devices and advanced memories. The role of suitable self-assembly monolayers (SAM)[20, 21] is to host SBUs on the functionalized wafer surfaces with preferred alignment directions[22, 23] before the organic ligand is offered. The choice of SAM is also very critical to match between the work function of the device metal electrodes and that of the MOF layer to achieve sufficient charge injection from the electrodes. The benefits behind of SAM, that they are efficient surface chemistry and can be also patterned between device electrode, and easy to be tailored for specific applications such as injection, wetting/de-wetting, templating, conductive, or insulating layers, and hence can change the device performance without changing the device structure or materials.

CHAPTER 2: SURFACE MOUNTED METAL-ORGANIC FRAMEWORKS

2.1 Overview

Metal-organic frameworks (MOFs) have witnessed significant research growth during last two decades, as an advanced class of functional porous materials that adapts concepts from crystal engineering to self-assemble highly ordered crystalline nano porous[24] 1D, 2D, or 3D structures.

MOFs are constructed starting with metal holding hubs (secondary building units) and organic ligands and are known for permanent high porosity and massive inner surface area[25]. These properties, along with the exceptional level of structure variability for both organic and inorganic parts make them attractive candidates for wide range applications from catalysis as gas separation[26], gas storage[27], chemical and biological sensing[28], and to energy harvesting and storage systems. Because of their tunable structure and functional groups, those range for MOFs turned into a standout amongst the most developing fields for chemistry and yielded more than 20,000 structures.

In this dissertation, the focus is on the fabrication of solid-state films using conductive MOF materials on functionalized surfaces using SAM well-known as SURMOFs as presented in the following sections.

2.2 SURMOF Synthesis

2.2.1 Self-Assembly of Monolayers

Self-assembly is ubiquitous in chemistry, and biology which creates ordered ensembles of molecules or ordered forms of supramolecules to demonstrate how particles can interact through a balance of attractive and repulsive interactions to produce new noncovalent structures[29-31]

(Van der Waals and columbic interactions, hydrophobic interactions, and hydrogen bonds),[32] The process of self-assembly was discovered in 1946, by Bigelow et al.[30, 33-35] when the formation of well-oriented monolayers by polar organic particles adsorbed onto solid surfaces in non-polar solvents, and it took quite a few years until studies on silane monolayers[36], Sulphur (thiol) self-assembly[37, 38], carboxylic acids around metal oxides, or hydrogen bonding were revealed to form self-assembly on a diversity of surfaces like glass, quartz, silicon, mica, aluminum, and also gold and became applicable to a range of fields of nanoscience and manufacturing.

Self-assembly monolayers (SAMs) are two dimensional highly ordered molecular assembly formed in organized manner mainly with bottom-up approach by chemisorption on appropriate wafer surfaces and are essential prerequisites for the synthesis of MOFs. In essence, they can control the growth and alignment of the guest materials in a highly ordered fashion, are able to modify the surface with desired acceptor-donor properties, are responsible for device performance, and have been used in many research applications including biological sensors, nanoelectronics, electrochemistry, as well as in micro- and nano-electromechanical systems (MEMS, and NEMS, respectively)[39]. Self-assembly is an important technology for semiconductor patterning due to its unique interfacial properties at the nanoscale level. The easy and low-cost manufacturing methods which are applicable to nanoscale surface science help defeating the cutoff set by directed assembly such as photo-, or electron beam- lithography. The fundamental fabrication method of this assembly is based on dilute solutions that undergo a chemical change to produce an ordered molecular pattern through adsorption of a polymer or dynamic surfactant on a solid surface (Figure 1). The composed monolayer compromise 1) a head group usually contains thiol or methyl moieties to provide an active attachment onto the substrate

and possesses flexible attraction towards stabilizing and modifying the interfacial electronic states, 2) a tail-group which comprises of another functional group at the terminal end that defines the surface properties, and 3) Spacer usually an Alkane chain that provides a charge transport between both head and tail groups which is the fundamental backbone of the molecule with defined thickness that is capable to modify the electrical and optical properties of the monolayer.

Several techniques can be used to fabricate SAM thin films via two main approaches. Top-down approach utilizes guided or directed self-assembly of molecules by photo-, ion-, or electron beam- lithography to host precised MOF patterns on a functionalized substrate, and it is typically followed by wet or dry chemical etching to reveal the desired structure at a few 10 nm scale on a small surface area.

Another two different methods used for positional assembly resulting in a single molecule arrangement are atomic force microscopy and scanning tunneling microscopy, however it is a time-consuming process and is not viable for large scale fabrication.

Bottom-up approach allows to molecular self-assembly on a hosting substrate by selectively synthesizing adds atoms or molecules that get rearranged to create the final structure over large surface area. It is performed by dip coating process or by chemical or physical vapor deposition techniques accommodating a nanotechnology scale range from 1-10 nm. Therefore, bottom-up molecular self-assembly is an alternate process to directed self-assembly by photo- or electron beam lithography since it does not require chemical additives like photoinitiators or inhibitors and free from chemical etching step, and most importantly it offers the capacity to organize single molecules at the nanometer scale in a shorter amount of time.

MOFs can be built up on various terminating functional groups (*e.g.*, $-N$, [40] $-NO_2$, $-NH_2$, $-COOH$, and $-OH$ moieties)[41] on various surfaces, and this process is compatible with

vacuum technology and nanofabrication. In this context, the molecule 4-mercaptopyridine molecule which was chosen in all experiments in this dissertation since it forms coordination with the copper paddlewheels from axial positions while facilitating charge transport.

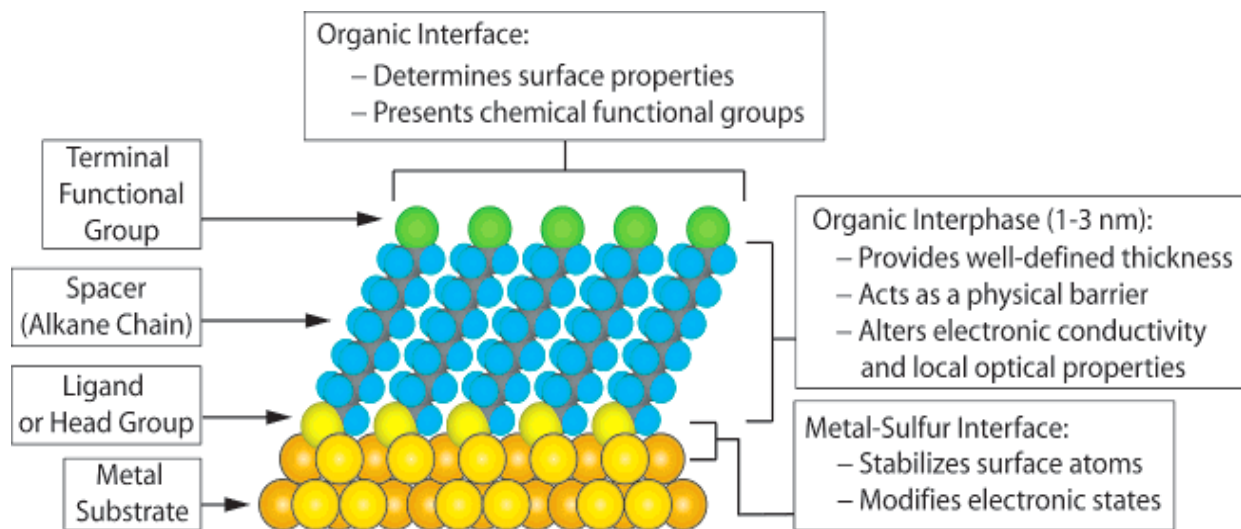


Figure 1 Scheme of SAM of alkanethiolates designed on a gold surface. Adapted with permission from reference [20]. Copyright 2005, American Chemical Society. See Appendix A: Copyright permission.

2.2.2 SURMOFs Synthesis

The fundamental fabrication of MOF thin films on a wide variety of surfaces such as Si, SiO₂, Alumina, graphite, and Au with modified organic surfaces were demonstrated[42]. 2D SURMOFs can be built up initially on functionalized surfaces with carboxylate or pyridine terminations among others, by connecting organic ligands with dicarboxylate sites to form 2D building block by the presence of metal ion $[M_2(COO-L-COO)_2]_n$ (M= Zn, Co, Cu, Ru, and L= ligand)[43] with microporous or mesoporous structures. SURMOFs with three dimensional lattices can be constructed[44] by using pillaring linkers such as Pyrazine[45-47], 4,4'-Bipyridine[48], or 1,4-diazabicyclo[2.2.2]octane (dabco) as depicted in Figure 2, which demonstrates the MOF synthesis by the incorporation of ligand carboxylates and pyridine sites that are coordinated orthogonally to the metal ions.[49]

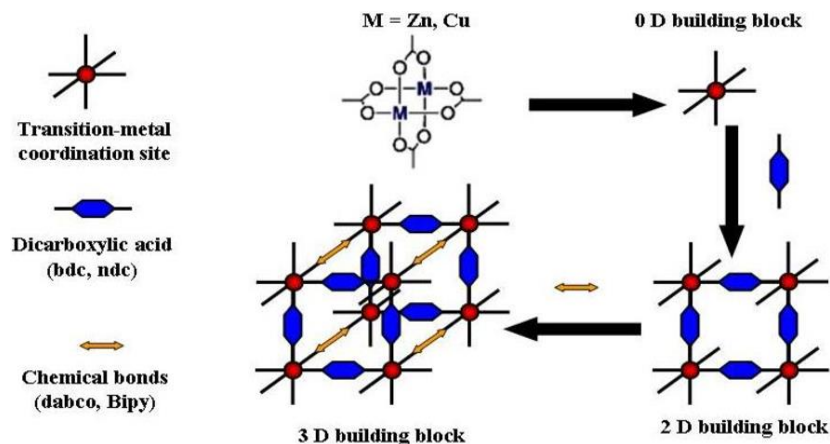


Figure 2 Schematic representation for the synthesis and formation of the 2D and 3D MOFs. Adapted with permission from reference [41]. Copyright 2010, Materials. See Appendix A: Copyright permission.

2.3 SURMOF Preparation

The growth of SURMOFs was demonstrated in literature[50] as depicted in Figure 3. A silicon substrate was modified with suitable self-assembly monolayers of 3-aminopropyl-trimethoxysilane (3-APTMS) thus mimicking the ligands used in normal solvothermal synthesis and provides a template for MOF growth,[21] then the functionalized substrate was immersed in the metal ion solution of zinc acetate, followed by an immersion in the organic ligand solution of L1: 1,2,4,5-tetrakis(4-carboxyphenyl)benzene, or L2: 5,10,15,20-tetrakis(4-carboxyphenyl)porphyrin to construct 2D thin film. By pillaring the metal ions with 5,15-di(4-pyridylacetyl)-10,20-diphenyl or 4,4'-Bipyridine, a 3D thin film can be obtained. Alternative synthetic methods were introduced by Stock and Biswas[51] including conventional solvothermal, electric heating, electrochemistry, microwave heating, mechanochemical, and ultrasonic. Those techniques were detailed by Ahn and co-workers[52].

In this dissertation, SURMOFs were growing epitaxially in a layer by layer fashion based on the synthetic procedure described in the previous section, the application of self-assembled conductive MOF structures was demonstrated in the chapter 4 using conductive organic ligands

(MTCPP, where M: free metal, Cu, Co, or Ni) which served as the backbones of the 2D frameworks with the metal ion dicopper paddlewheels. To exert electronic properties, pillaring linkers (i.e. Pyrazine or 4,4'-Bipyridine) were introduced to form the 3D MOF thin films.

A comprehensive evaluation of PES data was performed and correlated with density functional theory (DFT) calculations of the density of states (DOS) of the fabricated 2D and 3D MOF films involved to yield the molecular-level insights, and the electronic properties which were represented in band diagrams as demonstrated in Chapter 4 and 5.

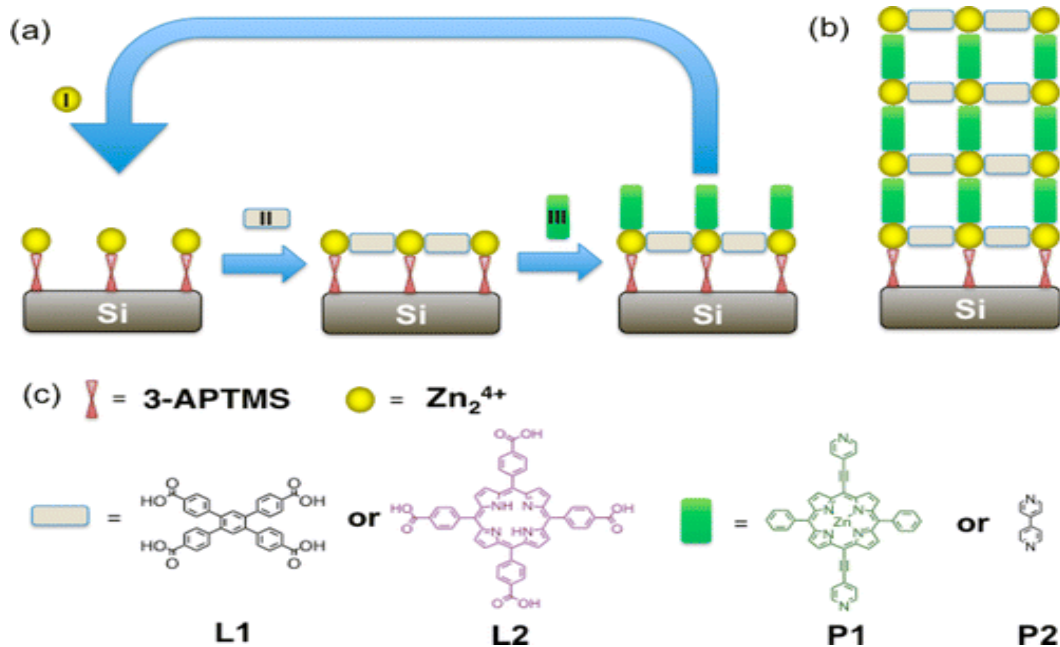


Figure 3 (a) Schematic diagram for the SURMOF growth sequence on functionalized Si surface by repeated immersion cycles in the metal ion solution, followed by L1 or L2 incubation to construct 2D MOF film (II), by incorporating pillaring linkers P1 or P2, a 3D thin film can be built. (b) SURMOF growth after N cycles of growth. (c) Representations of building blocks used in construction of MOF films. Adapted with permission from reference [50]. Copyright 2013, American Chemical Society. See Appendix A: Copyright permission.

CHAPTER 3: EXPERIMENTAL METHODOLOGY

3.1 Incubation Procedure

Liquid phase epitaxy (LPE) is essentially applied for the growth of semiconductor crystalline materials[52-54] in a layer by layer fashion, which enables to form stacked mono- or multi-layer structures by one or combination of different materials to produce homo- or hetero-epitaxial growth on atomically flat surface of another crystal with or without temperature, and it is mature technology to fabricate integrated circuits or solar cells[54]. LPE can be performed on a wide variety of substrates, very economic when up-scaled to mass production, and simple technique to grow crystalline semiconductor materials with the aim to fabricate molecular electronic devices.

The layer growth appears as functions of thermodynamic driving forces in a small supersaturation at the solid-liquid interface which is very small due to the reduced surface energy of the solution[54] unlike Molecular Beam Epitaxy (MBE) and Vapor Phase Epitaxy (VPE) with a layer growth that occurs in a high supersaturation at elevated temperature in a vacuum environment.

The epitaxial conditions can be executed from concentrated solutions at high temperature or from diluted concentrations at low temperature. In this dissertation, the LPE is performed from dilute solutions because it enables lower growth rates for enhanced thickness control, and improved structural perfections and excellent stoichiometry of the layers, and to minimize the risk of undesirable spontaneously nucleated crystallites. The growth starts when SAM molecules exist in the corresponding solutions started to diffuse and adsorb at the gold surface edges of the

substrate. Metal ions, organic ligands, or pillaring linkers can be attached to the anchored SAM molecule by self-assembly mechanism in a layer by layer fashion to construct SURMOFs. More details about the physical experimental methodology are covered in Chapter 4 and Chapter 5.

3.2 Photoemission Spectroscopy

Photoemission spectroscopy (PES) originates from the photoelectric effect initially observed by Heinrich Hertz in 1887 when he detected electrons emitted from a secondary arc due to the irradiation of incident UV light[55], then this phenomenon was further explained by Albert Einstein in his paper related to the theory of photoelectric effect in 1905 which led to the 1921 Nobel Prize award for the photoelectric law and his work domain of theoretical physics[56]. However, it was until 1950's when a high-resolution spectrometer was made by Kai Siegbahn and his co-workers[57] who was awarded half a Noble Prize in 1981 and William Jolly who pioneered core level electron spectroscopy, and this technique has been developed further by using synchrotron radiations since then enabling improved special and higher energy resolutions.

3.2.1 Physical Principle

In a direct PES experiment as illustrated in Figure 4, a solid-state material is irradiated with a source of a monochromatic light of energy $h\nu$ causing a photon absorption that undergoes a transition from electronic ground state with energy E_i into an excited state with energy E_f provided its energy is high enough, this will liberate a photoelectron with energy E_k out of the sample surface into a ultrahigh vacuum system (UHV) which enters electron analyser to measure its kinetic energy (KE) distribution with respect to the Fermi energy of the sample as defined in equation (1), and to investigate the chemical composition and electronic states. Where E_k is the kinetic energy of the photoemitted electron (eV), h is Planck's constant (6.626×10^{-34} J. s), ν is the frequency of the photon in Hertz (Hz), E_B is the binding energy in (eV) which is equal to the

ground state energy of the photoemitted electron, and Φ is the work Function of the solid (eV) which is equal to the energy difference between the vacuum level and Fermi energy.

$$E_k = h\nu - E_B - \Phi \quad (1)$$

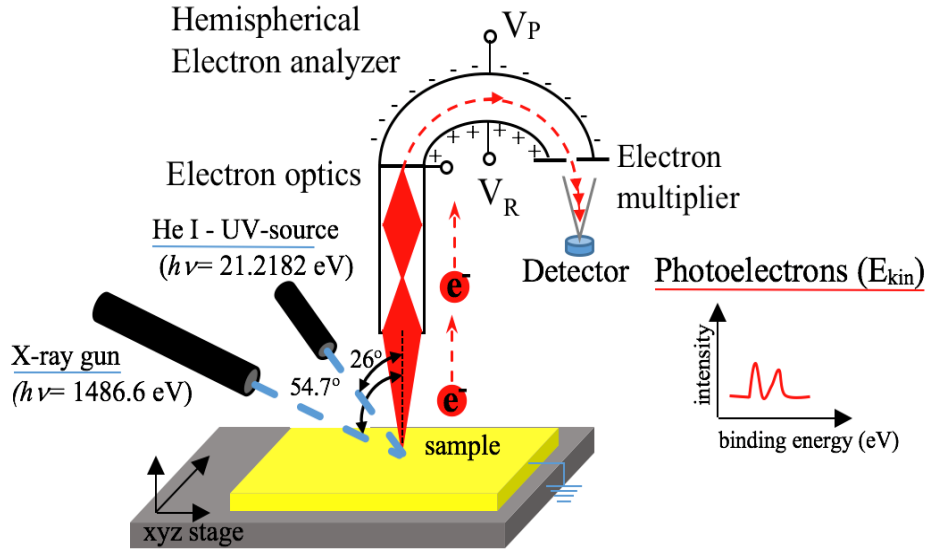


Figure 4 Sketch of typical direct PES setup with two light sources of X-ray gun and He I-UV discharge lamp. Light vector potential impinges on a sample, and electrons are excited by the photoelectric effect and travel within electron optics to hemispherical electron analyzer to be analyzed with respect to their Kinetic energy E_k .

The relation between the energy level diagram and the distribution of the photoemitted electrons is illustrated in Figure 5. The energy level of a solid sample consists of core levels with binding energy (E_B) and valence band. The binding energy E_B in solids is referred to the Fermi energy (E_f), and E_{vac} in both free atoms and molecules. In case of a metallic sample, the Fermi level will be positioned at the onset of the valence band showing no transfer band gap, and has a work function (Φ) defined as the minimum energy to remove an electron from the metal and is equal to the difference between the fermi energy (E_f) and the vacuum level E_{vac} . The inelastic electron scattering which lost its kinetic energy during inelastic collisions are represented by the secondary electrons that can be used to calculate the work function from the secondary edge.

When photoabsorption occurs in a valence state or core level with the binding energy (E_B), then a photoemitted electron will be detected and analyzed whose kinetic energy E_k according to eq. (1).

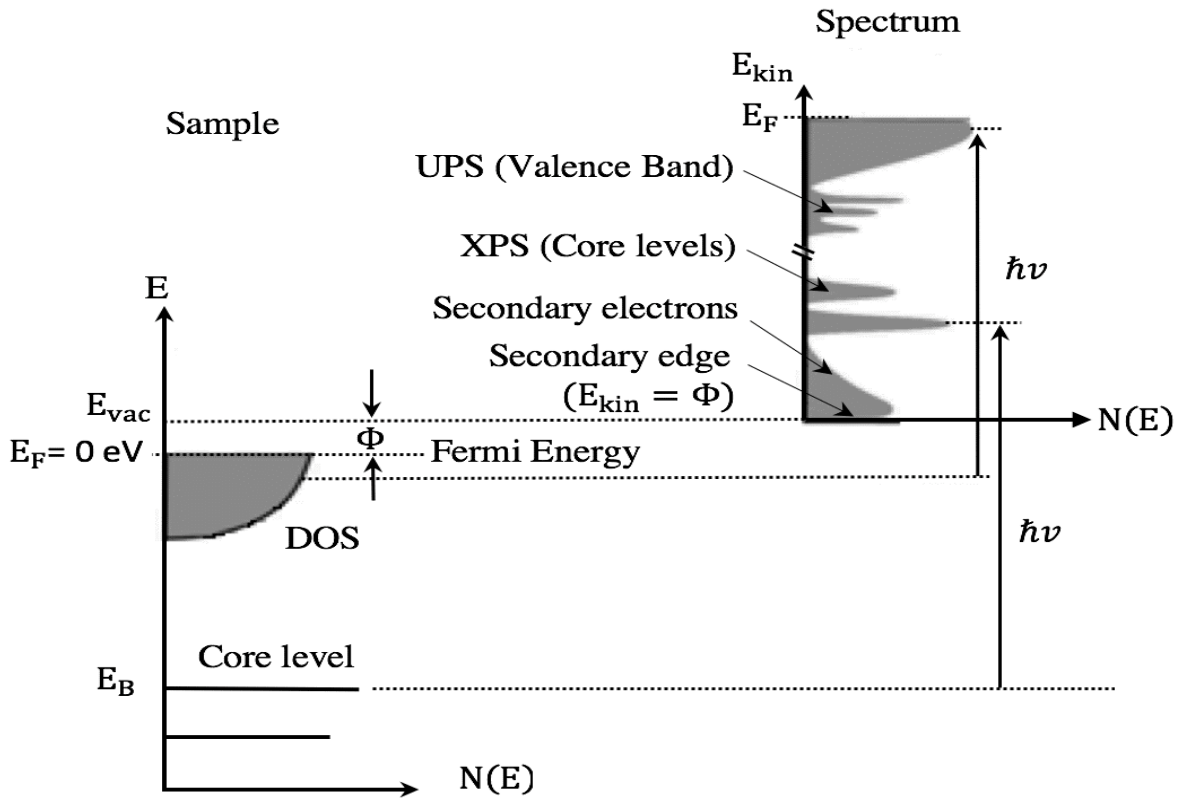


Figure 5 Sketch showing the energy level relations in PE process produced when photons impinged on the sample, producing kinetic energy distribution shifted by photons of energy $\hbar\nu$. E_B refers to the binding energy of electrons, which in the sample referred by the E_F , and E_{vac} in free atoms or molecules. Adapted with permission from reference [58]. Copyright 2003, Springer Science and Bus Media B V. See Appendix A: Copyright permission.

The PES is mainly sub-categorized according to source of radiations into four measurement techniques operate with different energy sources such as high energy photons or low energy electrons at various scan ranges: Low intensity X-ray photoemission spectroscopy (LIXPS), Ultraviolet Photoemission Spectroscopy (UPS), X-ray photoemission spectroscopy, and inverse photoemission spectroscopy (IPES). In XPS mode, a photon of energy 1486.6 eV is absorbed by an atom in the sample leading to ionization process, and emission of core electron to give crucial information about the chemical composition and structure. Whereas in UPS mode, a photon of

energy for He I= 21.2182 eV interacts with valence levels of material, leading to ionization by removing one of these electrons in the VB or HOMO. Each targeted element or material is represented unique spectrum that consists of number of emitted electrons as a function of their binding energy[58].

Inverse PES technique is used to investigate the unoccupied electronic structure, it is illustrated in Figure 6, and originates from the inverse photoelectric effect where an electron gun impinges the sample with an electron energy form ranged from 0 to 15 eV causing a transition from an initial state E_i into an unoccupied final state E_f , allowing an emission of a photon with the energy $E = h\nu$ which is the difference between E_i and E_f that is detected by a Geiger counter.

$$h\nu = E_i - E_f \quad (2)$$

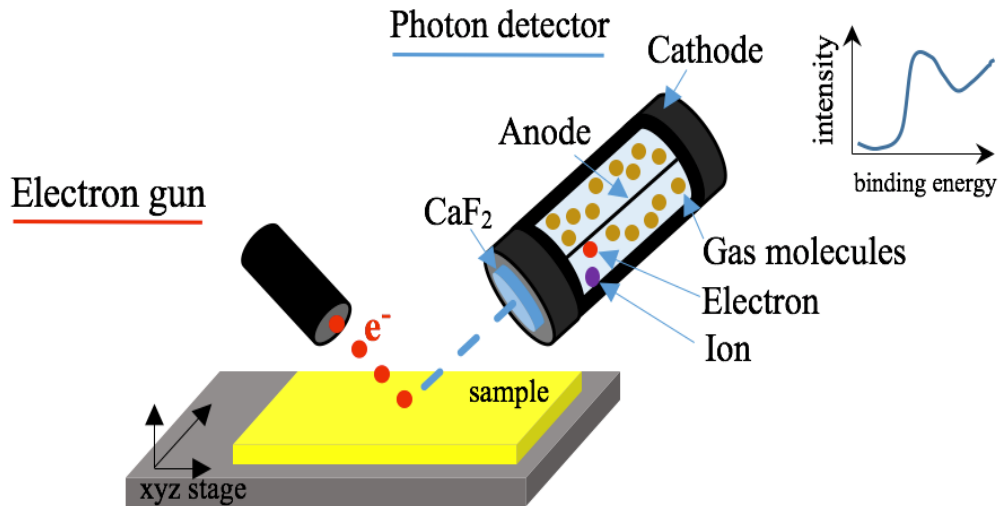


Figure 6 Sketch of typical inverse PES setup with electron gun and photon detector. Electrons impinges on a sample, and out coming photons will pass by band pass photon detector consisting of a CaF_2 window acting the low pass filter, and ionizing gas molecules setting the high pass filter, then they bound in the unoccupied state above fermi level representing the conduction band state.

3.2.2 Photoemission Process

PES incorporates three independent and sequential step model to manifest the photoemission data theoretically which initiated by Berglund and Spicer in 1964 as illustrated in

Figure 7; in the first step, photoexcitation of electron; when an incoming photon is absorbed which resulting in exciting and emitting an electron from an initial state orbital into a final unoccupied state in the bulk of the material. The second step provides information about transporting the excited electron to the surface of the material, and the third step describes the transmission and escape of this electron outside the surface into the vacuum where it can be detected and analyzed and reveal information about their origin[58].

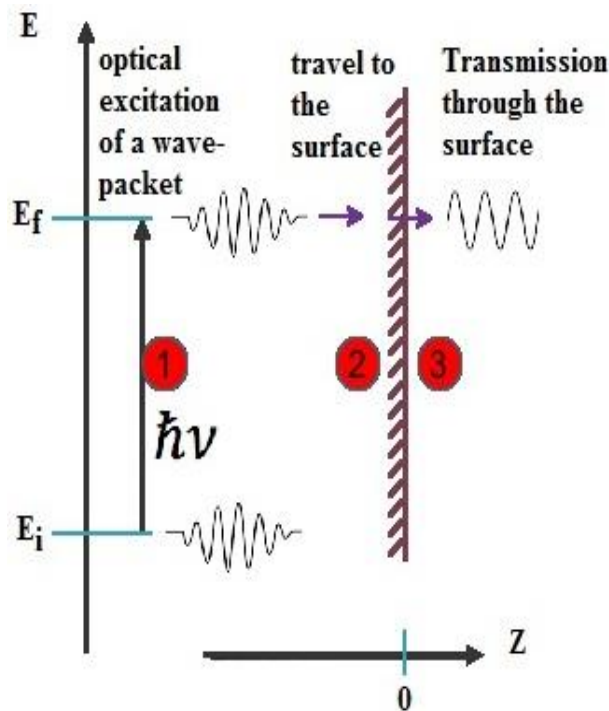


Figure 7 Sketch of the PES as a three-step process: 1) Photoexcitation of electrons, 2) transport to the surface with production of secondary electrons, 3) penetration the surface and escape into the vacuum.

3.2.3 The Electron Mean Free Path

It is crucial that the photoemitted electrons can be transported without colliding with air molecules and contained within stringent vacuum environments. The needs for UHV conditions for the investigations of surface states of materials can be manifested from Figure 8, which demonstrates the electron mean free path as a function of their kinetic energy for various selection

of a few metals is given by equation 3. The depth of penetration of incoming photons in the range of microns and it depends on the density of the chosen material, since the electron mean free path extends only in a very few angstroms, this means only electrons will be excited and emitted from the top of a few very thin layers which can be detected, and therefore the study of the sample required atomically clean surface to avoid interference from adsorbed impurities, otherwise the electrons will be absorbed by adsorbed contaminants and impairs the investigation of the sample surface. Electron interacting with surface yields appreciable photoemission information which makes PES advantageous to study the surface properties, however it requires vacuum of higher than 10^{-10} torr to prevent atoms or molecules from sticking onto the surface, which can form contamination monolayers.

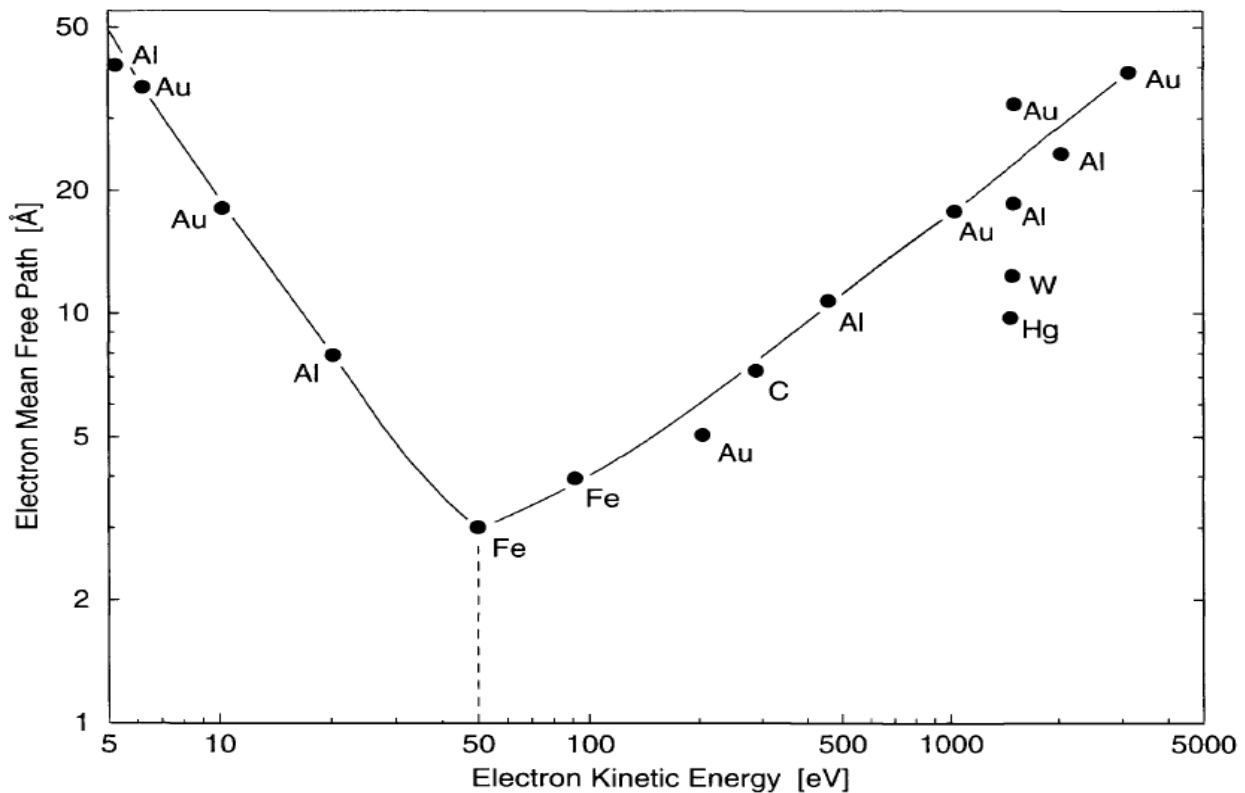


Figure 8 Electron mean free path as their function of their kinetic energy for various metals. Adpated with permission from reference [58]. Copyright 2003, Springer Science and Bus Media B V. See Appendix A: Copyright permission.

$$\lambda = E / \{E_p^2[\beta \ln(\gamma E) - (C/E) + (D/E^2)]\} \quad (3)$$

where λ is IMFP in Å, E the electron kinetic energy in eV, E_p is the free electron plasmon energy $[28.8 (N_{vq}/M)^{1/2}]$, ρ is the density in g. cm^{-3} , N_v is the number of valence electrons per atom or molecule, M , β , γ , C , D are atomic or molecular weight parameters[58].

3.3 X-ray Photoelectron Spectroscopy (XPS)

X-ray Photoelectron Spectroscopy is also known as Electron Spectroscopy for Chemical Analysis (ESCA), is one of the powerful surface science techniques to explore the first few atomic layers due to the mean free path of electrons (*i.e.* in solids is very small), and assign chemical states to the detected atoms. Surface analysis by XPS involves bombardment of a solid-state material in vacuo with monoenergetic soft X-rays, then photoelectrons are ejected from the different atomic shells of the element under investigation. The binding energies of electrons in the different shells can be observed in a spectrum which constitutes one of the most accurate sources of information on atomic level structure. The spectrum is obtained as a plot of the number of detected electrons per energy interval versus their binding energy. Individual element has a unique spectrum, the spectrum from a mixture of elements is represented by the sum of the peaks of the individual constituents. Quantitative data can be obtained from the peak height or area, and identification of chemical states often can be made from exact measurement of peak positions and separations, as well as from certain spectral features.

3.3.1 Basic Principles of X-ray Photon Generation

As illustrated in Figure 9, high energy electron bombards a twin anode made of either Al or Mg, causing ionization of electrons in core levels which generates X-rays radiation lines ($K_{\alpha 1/2}$) at energies of 1489.6 and 1253.6 eV, respectively. In addition to this process, Bremsstrahlung radiation is also produced. The irradiated area on the sample is elliptically shaped with an area of

1 to 2 cm² depending on the anode-sample distance. The aluminum radiation window prevents the Bremsstrahlung radiation and reduce the input of stray electrons from electron analyzer.

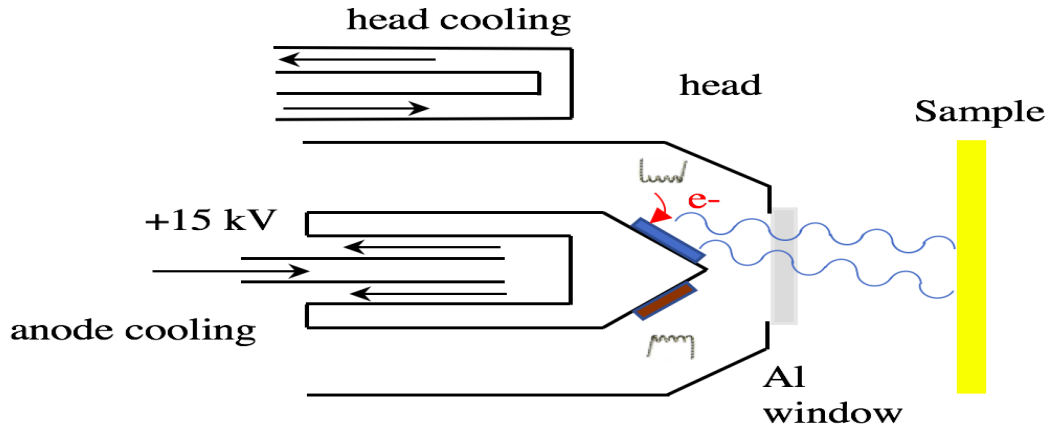


Figure 9 Principle of operation.

3.3.2 Spectrometer

PHOIBOS spectrometer is based on hemispherical deflection analyzer which consists of two hemispheres as depicted previously in Figure 4, the outer hemisphere is negatively charged which repels the incoming electrons, and inner hemisphere is positively charged which attracts the incoming electrons. It allows the energy of incoming charged particles entering through an entrance slit fitted with electronic optics to facilitate the transmission of a photoemitted electrons to the detector. When a fixed electric field gradient is applied across an outer hemisphere, only particles with specific kinetic energies are permitted to travel and make it to the detector. Whereas, electrons with lower kinetic energies will be deflected toward the positively charged outer hemisphere, and electrons with higher kinetic energies will approach the negatively charged inner hemisphere. Photons which bombarding the surface of a sample can result in the emission of photoelectrons as manifested by equation (1). The electron analyzer measures the kinetic energy of the electrons leaving the sample, if the X-ray energy and the kinetic energy of the electrons leaving the sample are known, then the binding energy of photoemitted electrons can be obtained.

In essence, each element has different and unique binding energy of specific atomic shells. The atomic shells of an element under X-rays bombardment absorb the photon energy then photoelectrons will be emitted to enter the electron analyzer to assign chemical states to the detected atoms. The binding energies of electrons in the different shells can be observed in a spectrum as illustrated in a typical XPS survey of sputtered Au film in Figure 10. The identification of emission characteristics attributed to the core level chemical states can be observed from the peak positions and separations, as well as from certain spectral features with respect to their binding energies.

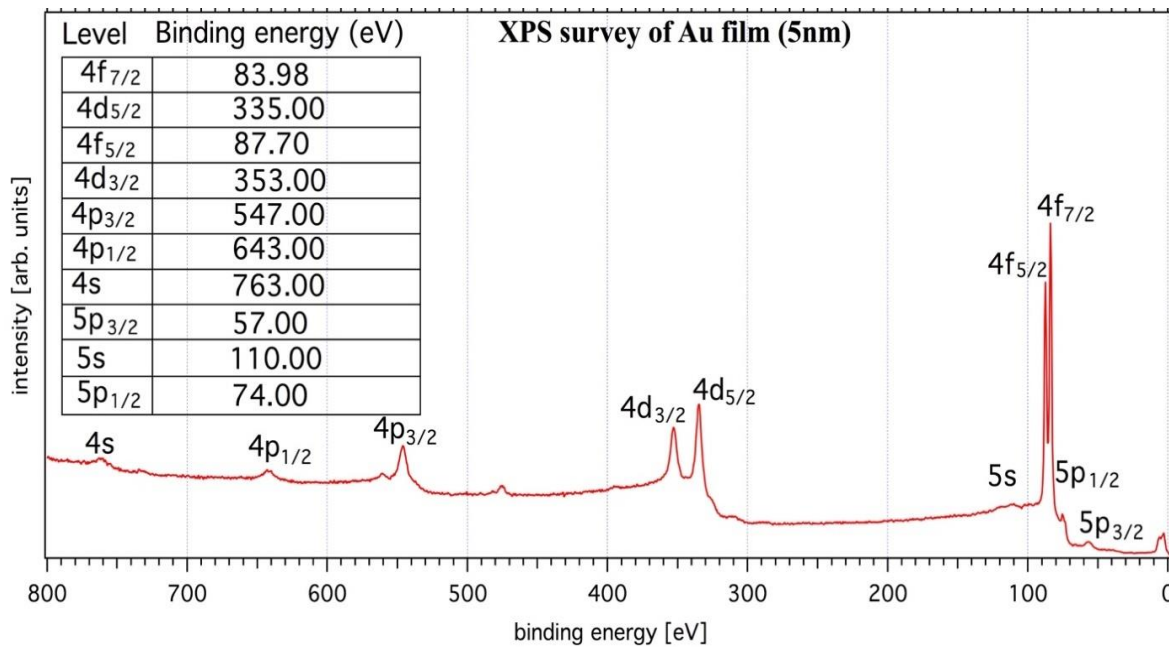


Figure 10 XPS survey spectra of sputtered Au film showing the count rate of photoelectrons as a function of binding energy. The core emission levels of Au are positioned at corresponding energy values as shown in the table.

A high resolution XPS spectrum measured on Au film is shown in Figure 11. The Au 4f region reveals two spin-orbit doublets into the Au 4f_{7/2} and Au 4f_{5/2} positioned at 84, and 87.7 eV respectively, a distinguished separation of its spin-orbit components value is found at 3.7 eV with asymmetrical peak shape.

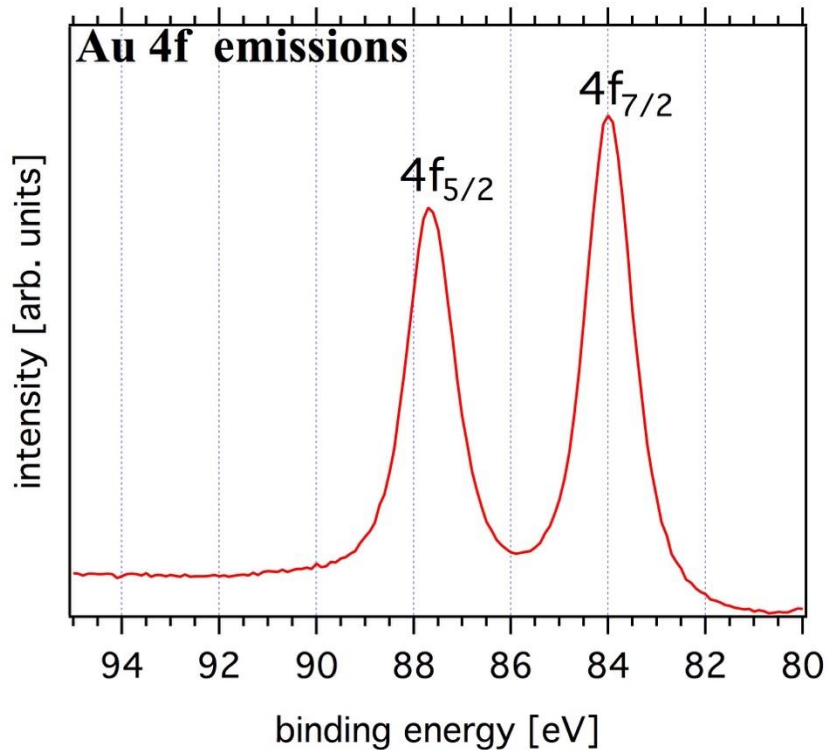


Figure 11 Au 4f core level XPS spectra of sputtered Au film.

3.4 Low Intensity X-ray Photoemission Spectroscopy (LIXPS)

Low intensity X-ray photoemission spectroscopy (LIXPS) uses an X-ray with low photon density of Mg K, 1253.6 eV, standby mode: 0.1 mA emission current to reveal the work function of the surface from the secondary edge of the spectrum. It gives information about the energy required to emit an electron from the fermi level of the material into a vacuum environment. This accurate measurement allows to avoid any photochemical reactions or modifications on the targeted surface which often occur after UPS measurement as charging artifacts. LIXPS is less affected by this issue which can be seen on organic materials due to the low conductivity of these molecules that cause peak shifts by charging phenomena compared to UPS. LIXPS is conducted in this dissertation prior and post UPS measurement to reveal any photochemical modifications caused by UV irradiations. Figure 12 Shows the LIXPS spectrum of sputtered clean Au film, the secondary edge (SE) is located at high binding energy between 15 and 17 eV which is defined by

the work function of the sample. The work function is determined by the difference between the energy of the X-ray photons (21.2182 eV) and the Au binding energy of the SE value of 15.97 eV, and by adding the analyzer correction factor (bf) value of approximately 0.1 eV.

$$W_f = h\nu - SE + bf \quad (4)$$

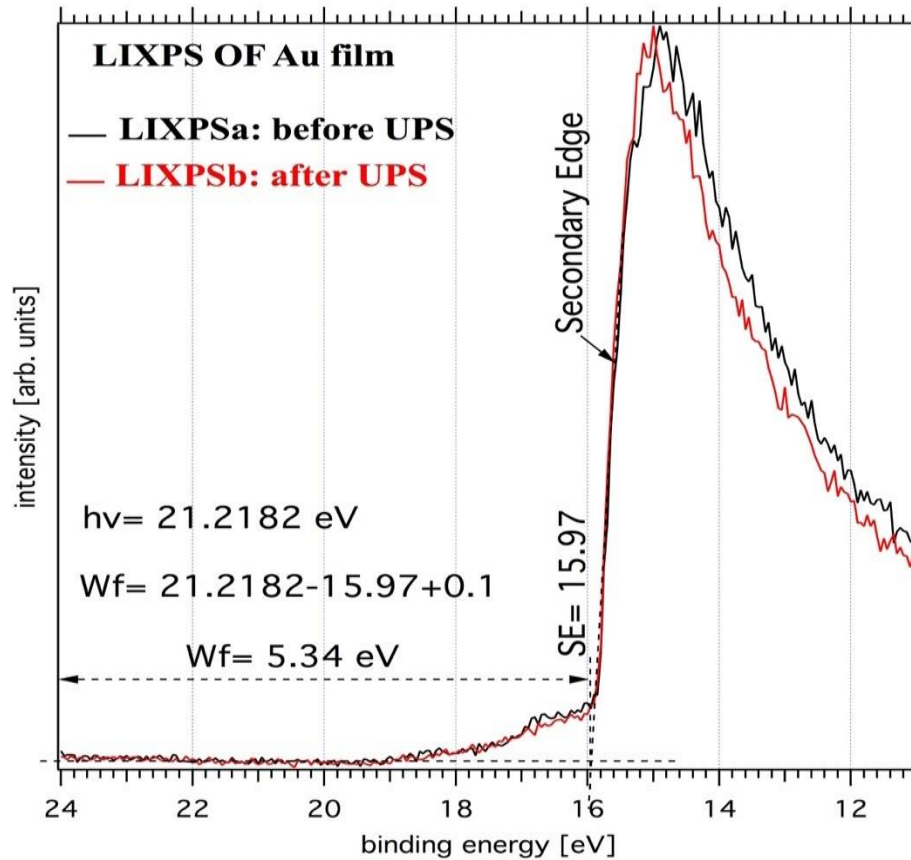


Figure 12 LIXPS spectra of sputtered clean Au film. The normalized secondary edges were measured with LIXPS before (LIXPSa, black spectra) and after (LIXPSb, red spectra) UPS.

3.5 Ultraviolet Photoemission Spectroscopy (UPS)

Ultraviolet Photoemission Spectroscopy (UPS) uses UV light to generate incident photons radiations by using a capillary discharge UV lamp from He (I) radiation of energy ranges from 10 to 50 eV on a solid-state material to examine the valence electron density of states. The narrow line width of UV excitation is in few meV which makes it more advantageous over X-rays without further monochromatization, and due to quasimonochromatic character of its excitation lines

provides a higher electron energy resolution capability of about 0.01 eV to reveal molecular vibrational structures. At low photon energies between 20 to 40 eV which is lower than the X-ray radiations value of 1253.6 eV, the s-like valence electron structures are minimized in comparison with p-like orbitals. At 40 eV, d-like valence electron structure can be revealed. Band structure calculations can be used in conjunction with UV excited photoelectron spectra to reveal more information about surface chemical analysis.

The UP-spectrum of valence electronic structure measured on sputtered clean gold surface is shown in Figure 13. The secondary edge (SE) is located at high binding energy from which the work function can be calculated as demonstrated in equation 4; where W_f is the work function in eV can be obtained from subtracting the secondary edge (SE) cutoff from the UV excitation energy ($\hbar\nu = 21.2182 \text{ eV}$), and by adding the analyzer broadening factor value of 0.1 eV. The surface of the certain samples might be sensitive to high photon density of UV irradiation and may result in charging artifacts, which can build up a positive charge due to the incomplete replenishment of ejected photoelectrons or due to the surface photochemical modifications during the measurement. The broad hump after the SE is as a result of inelastic scattered electrons escaped from the material surface and has no information related to the electronic structure. Valence band structures are located at low binding energies where Au 5d band contribution is revealed. The d band doublet emission peaks contain hyper-fine structures positioned at 6.15 and 3.7 eV which attributed to the overlap of filled 5d orbitals from gold atoms[59]. The drop-in intensity at lowest binding energy is assigned to valence band for inorganic materials or HOMO onset for organic materials, and this onset coincides with the Fermi level which is positioned at 0 eV for gold or other (semi)metallic surfaces. Whereas, a shift of this onset toward high binding energies gives information whether the surface has semiconductive or insulating property. The valence band emission from UPS

measurement along with the conduction band emission from IPES provide rich information about the band gap of the material as well as crucial information about charge injection barriers.

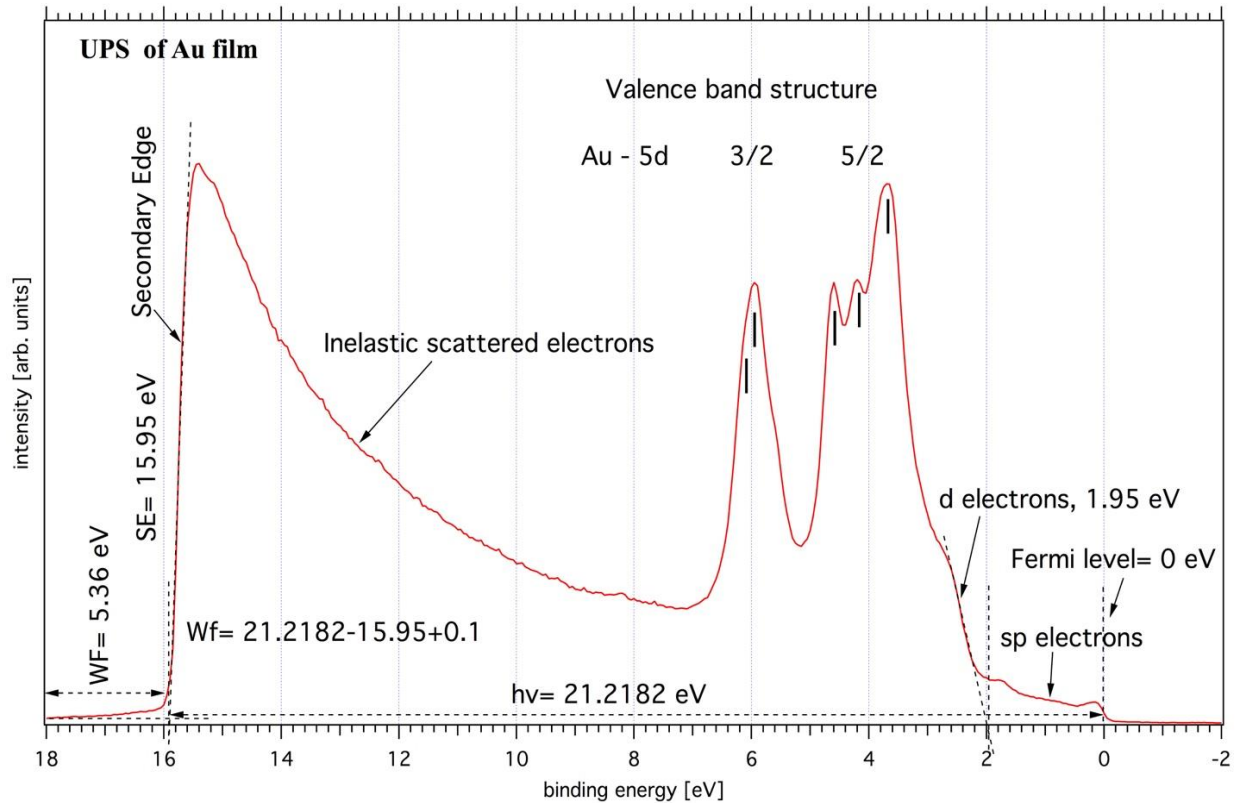


Figure 13 The characteristic of high-resolution UP-spectrum of Au surface showing the secondary edge cutoff at high binding energy, the inelastic scattered electrons, valence band structure, and fermi level positioned at 0 eV.

3.6 Inverse Photoemission Spectroscopy (IPES)

As manifested previously in Figure 6, the inverse photoemission spectroscopy (IPES) uses an electron gun that impinges the surface of the sample with monochromatic electrons which binds with an unoccupied band state above Fermi level, and then falls into lower lying unoccupied band state, as a result of this process, photons are emitted from the sample into vacuum, then recorded by a photon detector to give information about conduction band or LUMO.

Figure 14 shows typical IPES scan on Au film. The onset of conduction band is positioned the fermi level 0 eV for Au and other metals, and this is a crucial property of the targeted material

to determine the band gap of semiconducting and insulating surfaces in conjunction with the valence band value from UPS measurement.

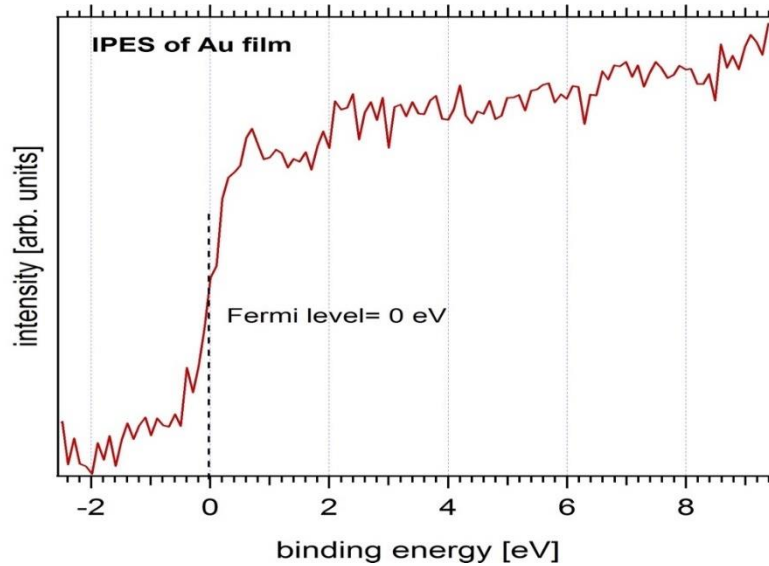


Figure 14 IPES of Au film showing the onset of conduction band state coincides with the fermi level.

3.7 UHV Multi-Chamber Analysis System

All experiments performed UHV multi-chamber analysis system (SPECS Nano Analysis GmbH, Berlin, Germany) under ultrahigh vacuum (UHV) conditions (2×10^{-2} mbar base pressure) as depicted in Figure 15. The system consists of a fast entry lock, transfer chamber for sputtering, atomic layer deposition chamber, deposition chamber for metal evaporation and electro spray deposition, and analyzing chambers equipped with X-ray, ultraviolet, and inverse photoemission spectroscopy (XPS, UPS, and IPES, respectively as illustrated in a physical setup shown in Figure 16. A homemade acrylic glovebox was attached to the load lock, which enables a direct transfer of the sample from the sample preparation area under 99.995% N₂ into a vacuum system, with a sequence of surface cleaning and direct and inverse PES measurement of a reference Au sample, which is followed by transferring the sputtered clean sample into the glove box for SAM functionalization, and MOF deposition via incubation procedures.

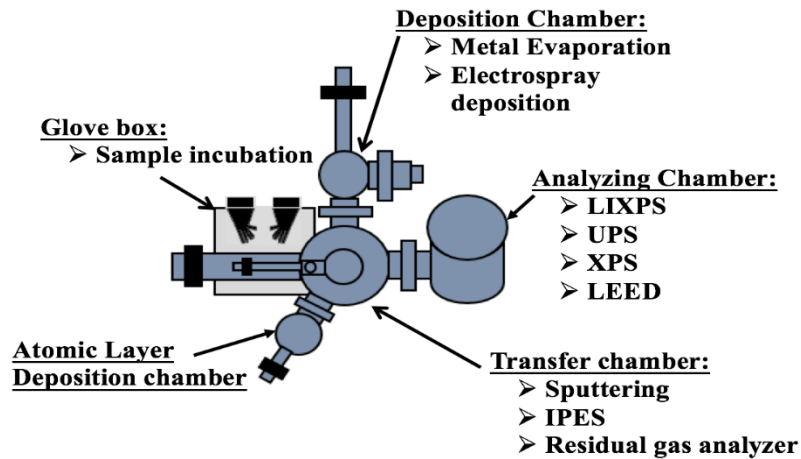


Figure 15 Simplified schematic of the UHV multi-chamber analysis system used for direct and inverse PES measurements on SURMOF. The system consists of a glove box, transfer chamber, ALD, deposition chamber, and analyzing chamber.

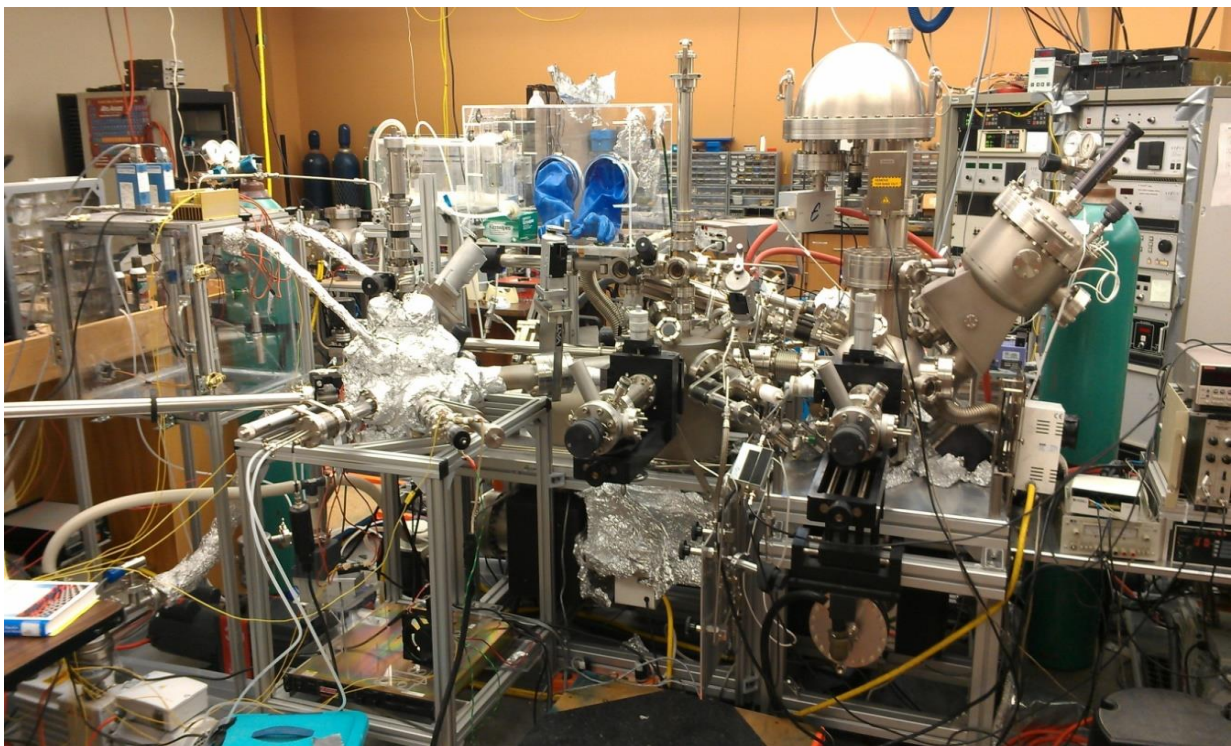


Figure 16 The multi-chamber deposition and characterization systems.

The advantage of such system is the ability to perform PES measurements on the SURMOFs in-situ without exposing the sample to the ambient. This is crucial system is to allow accurate investigations of the physical electronic and chemical properties, and interfacial growth

of MOF thin films. Such characterizations are important and has implications on the energy level alignments which provides the scientific foundation of molecular junctions and nanoelectronic devices.

3.8 Experimental Variability of Photoemission Measurements

In this dissertation, the resultant work function values of MOF materials were obtained and compared with the Au standard measurements as presented in the following two chapters. The uncertainty factor using an energy step function with a value of 0.10 eV accounted in the equation (4) for the analysis system's resolution. A fitting procedure was written and applied by IGOORE software to calculate the accurate values of the secondary edges from LIXPS and UPS measurements. The XPS survey spectrum in Figure 10 uses high pass energy mode in the analyzer system which enables more electrons to reach the detector and produces high intensity spectrum with a high signal to noise ratio for individual core level emission features but at the expense of sacrificing energetic resolution. This is still reasonable as it is accounted for a qualitative analysis related to the elemental composition of a targeted sample. Whereas, the high magnification spectra in Figure 11 uses low pass energy mode which results in a much lower intensity but with drastically improved resolution compared with the wide-scan survey spectrum, this enables to detect finer details such as peak shifts due to chemical change or structural evolution, or multiplet peaks related to information from chemical elements existed in various chemical environments.

The major advantage of UPS measurements lies in its high surface sensitivity and resolution value of 10 meV which is related to the narrow linewidth of the electronic transition in the discharge process that enables precise analysis of the hyper-fine structure of the valence band features. The variability of the several experiments confirmed on SUMOFs by the control experiments produced the same HOMO values even though the MOF components were selected

from different batches, and the HOMO features at the MOF interface is consistent as layers grow in thicknesses.

The resolution analysis of IPES measurements is about 0.4 eV, this accounts for the current setup of the Geiger photon counter that uses a CaF₂ window with a low-pass filter with 10.08 eV cutoff energy, and uses an Acetone vapor mixture with Argon utilized as ionization gas with a high-pass cutoff energy value of 9.69 eV. A spectrum was calibrated on sputtered Au film and is assessed to a value of 4.89 eV. Then, the energy scale was modified by positioning the Fermi edge at 0 eV. This was taken as a reference to quantify the conduction band onset as well as the LUMO level from measurements on the SURMOFs.

CHAPTER 4: ADVANCED PHOTOEMISSION SPECTROSCOPY INVESTIGATIONS WITH DFT CALCULATIONS ON THE SELF-ASSEMBLY OF 2D METAL-ORGANIC FRAMEWORKS NANO THIN FILMS¹

4.1 Abstract

Metal-organic frameworks (MOFs) deposited from solution have the potential to form 2-dimensional supramolecular thin films suitable for molecular electronic applications. However, the main challenges lie in achieving selective attachment to the substrate surface, and the integration of organic conductive ligands into the MOF structure to achieve conductivity. The presented results demonstrate that photoemission spectroscopy combined with preparation in a system-attached glovebox can be used to characterize the electronic structure of such systems. The presented results demonstrate that porphyrin-based 2D MOF structures can be produced and that they exhibit similar electronic structure to that of corresponding conventional porphyrin thin films.

Porphyrin MOF multilayer thin films were grown on Au substrates pre-functionalized with 4-mercaptopyridine (Mpy) via incubation in a glove box, which was connected to an ultra-high vacuum system outfitted with photoelectron spectroscopy. The thin film growth process was carried out in several sequential steps. In between individual steps the surface was characterized by photoemission spectroscopy to determine the valence bands and evaluate the growth mode of the film. A comprehensive evaluation of X-ray photoemission spectroscopy (XPS), ultraviolet

¹This chapter was adapted with permission from [40]. Copyright 2016, American Chemical Society. DOI: 10.1021/acsami.6b10340. See Appendix A: Copyright permissions.

photoelectron spectroscopy (UPS), and inverse photoemission spectroscopy (IPES) data was performed and correlated with density functional theory (DFT) calculations of the density of states (DOS) of the films involved to yield the molecular-level insights into the growth and the electronic properties of MOF-based 2D thin films.

4.2 Introduction

The past two decades have witnessed a growing interest in the area of metal-organic frameworks (MOFs), an advanced class of functional porous materials that adopts concepts from crystal engineering to self-assembled highly ordered crystalline porous materials[24]. MOFs are highly attractive to both academic and industrial communities due to their potential applications such as heterogeneous catalysis[60], gas storage[27], gas separation[26], drug delivery[61], sensing[28], or storage devices[62]. As crystalline porous coordination polymers, MOFs are constructed by connecting metal ions or clusters with organic based ligands. This results in porous crystalline nanoscale frameworks composed of a variety of molecular compounds containing highly tunable empty space for guest molecule adsorption. Meanwhile, this also makes these materials interesting for controlled mass transfer and opens the prospect of creating tailor designed materials with both electronic and ionic conductivity.

In particular, the self-assembly of conductive MOF structures on wafer-type supports and the investigation of their performance in device structures are of great interest for next-generation electronic device development. Such devices can be manufactured through a combination of standard lithographic techniques and molecular self-assembly of embedded MOF structures. The resultant materials integrating ionic and electronic conductivity in one single structure would exhibit promising applications in energy storage, fuel cell and other areas. Probably the prime example are memristive[63],[62] circuit elements as demonstrated by Hewlett Packard[64], which

demonstrate the high significance of materials with combined electronic and ionic conductivity for future technological applications. Memristors enable a remarkably simple (compared to transistor/capacitor based classic static or dynamic random access memory(RAM)) design of memory elements, which only need two terminals for read and write operations, while being able to store the information for long times without power.

The well-developed crystal engineering strategy enables us to custom design MOFs structures via the judicious selection of the metal ions and organic linkers, which also suggests the self-assembly of MOF-based device structures with electronic conductivity is viable. Among a variety of organic linkers used to fabricate nano thin films, porphyrin ligand, because of their versatility and functionality, present tremendous potential when combined with suitably chosen active SBUs. However, when applying MOF or related coordination materials on nanoelectronic devices, the main challenges to be addressed lie in controlling the size of objects at the nanoscale and aligning such objects on surface of various substances in certain desired ways without losing their original electronic properties.

In essence, π -stacked conjugated molecular structures need to be achieved in such materials. This was shown recently by Narayan et al[14]. who synthesized a conducting porous framework based on columnar stacks of TTFTB (tetrathiafulvalene tetrabenzoate). Recent research on covalent organic frameworks (COFs) has shown that conductive molecular materials like porphyrins and phthalocyanines can be used for the formation of porous structures with charge transport capabilities [65], [66]. This suggests that these molecular building blocks should be employable for conductive MOF structures.

The tailor design of conductive MOF structures makes it necessary that the electronic structure can be measured to provide feedback for the design process. The presented research

demonstrates that photoemission spectroscopy in combination with clean structural synthesis in a vacuum system attached glove box can be used for the characterization of the frontier orbital structure of self-assembled MOF films. This research is based on an established track record of this measurement technique for the characterization of the electronic structure of interfaces composed of conductive small molecular as well as polymeric materials.

In essence, the photoemission spectroscopy results of both UPS and IPES measurements yield the density of states of the highest occupied molecular orbitals (HOMO), and lowest unoccupied molecular orbitals (LUMO), respectively, relative to the Fermi level. Since this measurement occurs in ultra-high vacuum and also is very surface sensitive (only the top 5 nm are ‘seen’) the investigated samples need to be prepared in vacuum or in the inert environment of a vacuum-attached glove box. Such measurements were successfully demonstrated in the past for a variety of molecular materials such as conductive polymers, small molecular electroluminescent materials, self-assembled monolayers or ribonucleic acids.

In this paper the application of this technique to self-assembled conductive MOF structures is demonstrated. Self-assembled MOF thin films were grown in several steps, while characterizing the electronic structure depending on the layer thickness. In these experiments MOF thin films composed of TCPP linkers and dicopper paddlewheel secondary building blocks (SBU) were self-assembled on top of SAM-terminated (MP) Au substrates. The TCPP molecule is a prototypical linker-molecule candidate for conductive MOF structures, and well-suited for the presented measurements since similar measurements were already demonstrated successfully on evaporated porphyrin thin films[67, 68],[69]. The molecule MP was chosen as SAM substrate for the structure since it is capable of coordinating to the copper paddlewheels from axial positions while facilitating charge transport. These experiments were accompanied by computational DFT

calculations on the DOS of the prepared MOF structures. These calculations showed strong agreement and allowed the interpretation of the photoemission data.

4.3 Experimental and Simulation Sections

4.3.1 Materials

MOF Materials: MOF Synthesis. $\text{Cu}(\text{NO}_3)_2$ and TCPP (5,10,15,20-tetrakis(4-carboxyphenyl) porphyrin); 4-mercaptopyridine (96%), as well as anhydrous ethanol were purchased from Fisher Scientific. The N,N-dimethylformamide (DMF), (ACS, 99.8+%) was obtained from Alfa Aesar, and the thin film Au (100nm Au deposited on a 20nm Ti adhesion layer on glass slides) substrates were purchased from EMF Corp. (Ithaca, NY).

4.3.2 Sample Preparation

All experiments were performed in a commercial multi-chamber system (SPECS Nano Analysis GmbH, Berlin, Germany) under ultrahigh vacuum (UHV) conditions (2×10^{-10} mbar base pressure). The system consists of a fast entry lock, transfer chamber for sputtering, and analysis chambers equipped with X-ray, ultraviolet, and inverse photoemission spectroscopy (XPS, UPS, and IPES respectively). A home-made acrylic glovebox was attached to the load lock to enable a direct transfer of the sample from the sample preparation area into the vacuum. The glovebox was filled with 99.995% N_2 and kept under slight overpressure to suppress sample contamination from the ambient environment during sample preparation.

The thin film Au (100nm thick) substrates were cut into $1 \times 1 \text{ cm}^2$ pieces and mounted on a substrate holder via screws. This allowed for direct electrical contact between the Au layer and the chamber ground to avoid charging effects. The substrates were then transferred into UHV chamber for sputtering to clean the Au surface. A SPECS IQE 11/35 ion source with a kinetic energy of 5 KeV and an emission current of 20 mA was used and the sample sputtered for 40 min

at an Ar pressure of 4 mbar[70]. After sputtering, the clean Au substrates were characterized by the standard measurement sequence beginning with an LIXPS measurement (Mg K, 1253.6 eV, standby mode: 0.1 mA emission current), then followed by UPS (He I, 21.2182 eV), XPS (Mg K, 1253.6 eV, 20 mA emission current), and finally an IPES measurement (electron gun, Kimball ELG-2/EGPS-1022, and a Geiger counter with an energy resolution of about 0.43 eV).

The deposition experiments started by loading an Au substrate into the glovebox for the growth of the SAM via incubation. The sample was placed into the bottom of a vial containing the SAM solution (1 mM SAM solution of 4-mecaptopyridine in ethanol stirred at 80 °C for 24 hours). The vial was sealed and placed in the glovebox for 24 hours at 40 °C. After cooling the sample to room temperature, it was removed then rinsed gently with ethanol, deionized water, and dried with a stream of 99.995% N₂.

In the first MOF experiment (A), the Au functionalized substrate was alternately immersed into the metal ion solution (13.329 mM Cu(NO₃)₂ solution in DMF stirred on a hot plate at 80 °C for 24 hours) for 12 hrs followed by an immersion step in the organic ligand solution (1.2645 mM TCPP solution in DMF stirred on a hot plate at 80 °C for 24 hours) for an additional 12 hours, three sequential incubation cycles were performed in the glovebox at a temperature of 40 °C. In between each immersion step, the substrate was rinsed with fresh DMF and deionized water to remove excessive unbound molecules from the surface[71], and dried in a stream of 99.995% N₂ as depicted in (Figure 17), which shows the expected crystal structure[72]. Following each individual immersion cycle, the surface was characterized with the above LIXPS/UPS/XPS sequence.

In a control experiment (B), fresh TCPP and Cu(NO₃)₂ solutions were mixed together in a vial following the same concentrations and conditions reported in the main experiment (A). An

identical Au functionalized surface was immersed into a vial containing the mixed solution for three incubation cycles in the glovebox each for 24 hours at 40 °C (identical conditions as in experiment A). After each complete incubation cycle, the substrate was rinsed with DMF and deionized water, and then dried with 99.995% N₂. This was followed by transfer into the attached vacuum system and PES characterization.

In the second control experiment (C), the Au functionalized surface was immersed in the TCCP solution (same concentration and experimental conditions as were used in experiment (A)), but the immersion in the Cu(NO₃)₂ solution was omitted. After the experiment, the sample was inserted into the vacuum system and then characterized by PES.

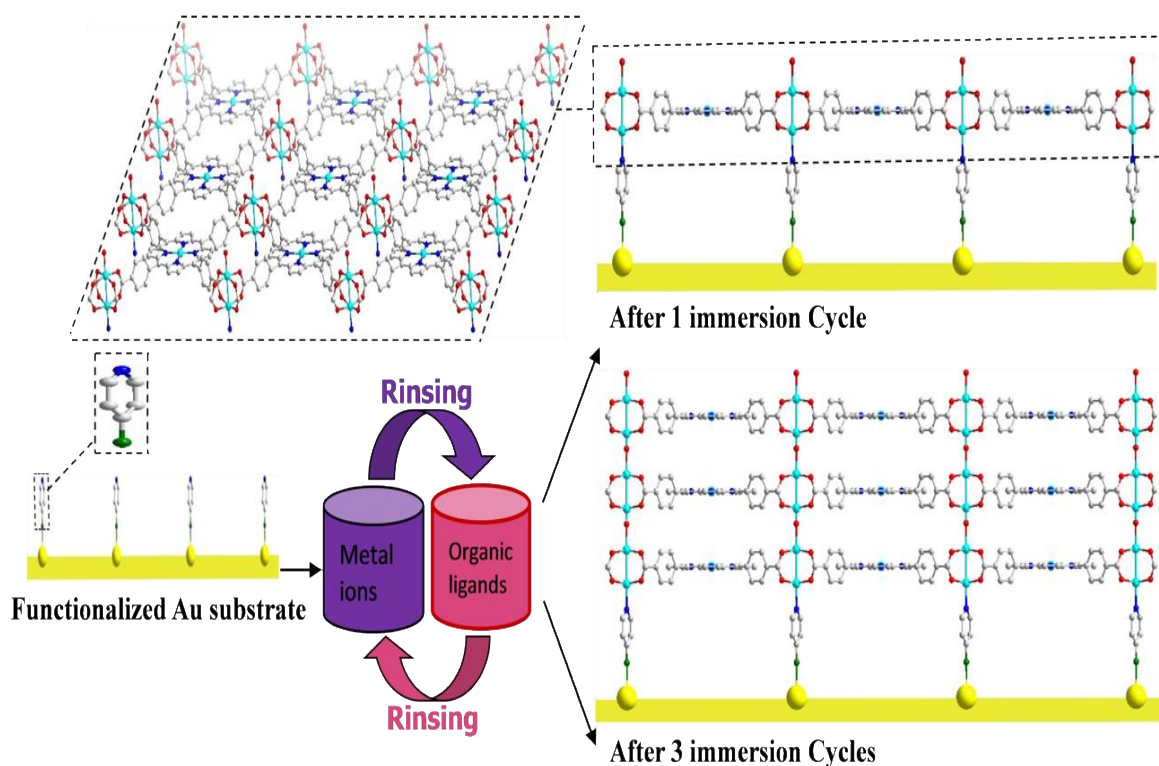


Figure 17 Schematic depiction of the growth sequence: MOF films were grown in three incubation cycles on a MP SAM-terminated gold substrate. First, the sample was incubated in the metal ion solution (Cu(NO₃)₂), followed by immersion into the organic ligand solution (TCCP). Each incubation step was completed by rinsing the sample in DMF and deionized water. Color assignment: carbon, gray; oxygen, red; sulfur, green; nitrogen, blue; cooper, cyan. Adapted with permission from [40]. Copyright 2016, American Chemical Society.

4.3.3 DFT Calculations on the Electronic Structure

The molecular modeling software Gaussian09 was used to perform all-electron DFT calculations on the metallated and free base TCPP molecules connected to Copper paddle wheels[72]. The computed structure of TCPP can be seen from Figure 18a and that of CuTCPP shown in Figure 18b.

The Gaussian basis set 6-311G** and DFT exchange correlation functional B3LYP with 2-dimensional periodic boundary condition were employed. The ground-state geometries of both MOF structures were fully optimized in vacuum, then the electronic structure and the energy levels were calculated. By considering possible deformation and thermal effects in the system, the theoretical DOS spectra are plotted by Gaussian broadening of the intensity around each energy eigenvalue. The results are compared with experimental UV photoelectron spectra in the discussion section.

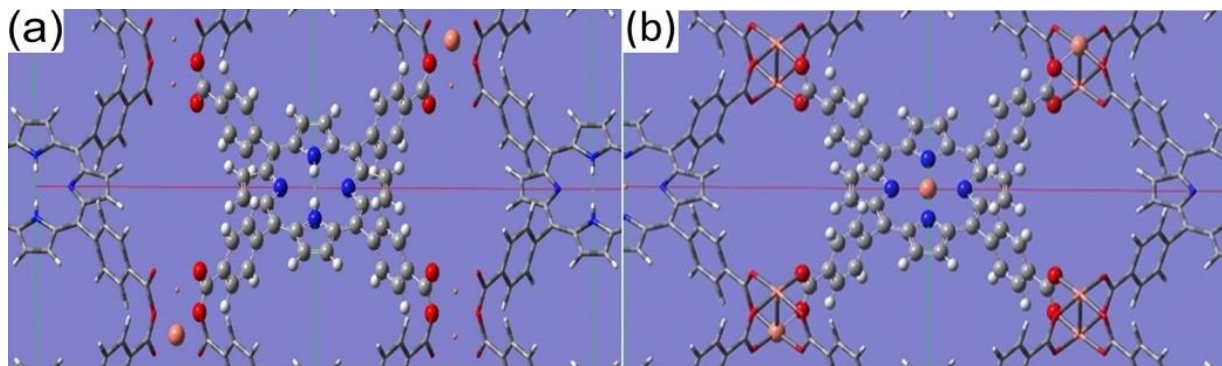


Figure 18 Computed structures of MOF molecules connected to Cu paddle wheels. (a) Free base TCPP, and (b) metallated CuTCPP. Adapted with permission from [40]. Copyright 2016, American Chemical Society.

4.4 Results

4.4.1 XPS Measurements

The standard LIXPS-UPS-XPS measurement sequence was carried out after each sample preparation step. Figure 19 shows the evolution of the C 1s, N 1s, O 1s, S 2p, Cu 2p, and Au 4f

core level emission lines throughout the three experiments A, B, and C. The bottom spectra correspond to the sputtered Au substrate as measured for experiment A. Experiments B, and C yielded similar spectra. The following spectra correspond to the incubations steps performed on each of the samples. The spectra measured for the clean substrate shows only weak O 1s and C 1s peak emissions at around 531 eV, and 284.8 eV respectively. These peaks are related to residual contamination from the sample holder assembly.

In the first experiment (A), the Au 4f signals were attenuated gradually after each incubation cycle, the 3rd cycle has negligible intensity compared to the 1st cycle which clearly indicates the surface has a substantial MOF growth with increasing thickness. The intensities before and after incubations allowed for an estimation of deposited layer thickness using the Lambert-Beer law with a mean free path for the emitted electrons of Au 4f through SAM[73],[74], and porphyrin derivatives[75],[76] respectively. The approximate thickness of the SAM is 0.45 nm, which is commensurate with the length of the molecule assuming it is aligned vertically on top of the Au surface. The individual layer thicknesses of the MOF 1st cycle, MOF 2nd cycle, MOF 3rd cycle, are 39.94 Å, 77.13 Å, and 112.7 Å respectively. The Au 4f emission features of the second (B) and third (C) experiments only show attenuation consistent to the SAM incubation cycle, but there is no further attenuation after incubation in the MOF solutions. This indicates that the MOF only grows if the SBU is present on the surface before the linker is offered.

The S 2p emission feature of the SAM has a binding energy of about 161 eV consistent with S in the thiolate form bonded to an Au surface[77]. This emission feature disappeared only in the first experiment (A) during the MOF incubation cycles, while it remained unchanged in the control experiments. This further supports the conclusion that the MOF film only grows if Cu (NO₃)₂ was deposited prior to incubation in TCPP. A similar behavior is seen in all other MOF

overlayer related emissions. Only in experiment (A) MOF related emissions occur, while experiments B and C show not much change after the SAM has grown.

The aromatic hydrocarbon related C 1s emission features of both SAM and TCPP multilayers produce a peak at about 285 eV. The distinguishing element in the C 1s spectra of the MOF layer has a smaller emission at about 288 eV, which is related to C-O bonds, which are found in the COOH groups of the MOF[78],[79].

This feature only occurs in experiment A, while the emissions seen in B and C retain their shape, intensity and binding energy during the incubation steps. This support that no film grew on top of the SAM layer.

The O 1s emission featured show a similar behavior. There is a small O 1s emission feature present after the SAM growth step. This emission line is related to residual surface contamination of surrounding areas on the substrate holder [80]. In experiment (A), this emission is attenuated at the expense of a strong new peak that is related to the COOH groups present in the MOF film [81]. Control experiment (B) shows a change in the O 1s spectrum due a small amount of deposited $\text{Cu}(\text{NO}_3)_2$ indicating that some molecules deposited on the surface during the incubation step. Experiment (C) shows again no change relative to the initial SAM layer, indicating that no film deposition. This clearly shows that $\text{Cu}(\text{NO}_3)_2$ needs to be present on the surface before incubation in TCPP if a thin film is to be grown.

The Cu 2p emission from the $\text{Cu}(\text{NO}_3)_2$ (orange spectrum) shows only contributions of Cu(I) with a binding energy of 932.4 eV. However, once the TCPP was added onto the surface, the Cu 2p emission (purple spectrum) revealed Cu(II) characteristic at 936.1 eV and additional satellite peaks at 940 eV and 944.3 eV assuming a Cu paddle wheel SBU was assembled by self-organization in situ by the presence of TCPP. The Cu 2p emission from the $\text{Cu}(\text{NO}_3)_2$ (orange

spectrum) shows only contributions of Cu(I) with a binding energy of 932.4 eV. However, once the TCPP was added onto the surface, the Cu 2p emission (purple spectrum) revealed Cu(II) characteristic at 936.1 eV and additional satellite peaks at 940 eV and 944.3 eV assuming a Cu paddle wheel SBU was assembled by self-organization in situ by the presence of TCPP. This is also supported by the particular structure of the observed emissions, which agree well with the data published by other groups[82], [83]. In addition, the binding energy of the spectra changes significantly once the MOF film forms. This is seen in the sequence of spectra of experiment (A) as the MOF film grows in thickness. The initial spectrum measured after the $\text{Cu}(\text{NO}_3)_2$ deposition step is gradually attenuated, while a spectrum with peaks shifted by about 3 eV to higher binding energy arises. This indicates a charge transfer from the $\text{Cu}(\text{NO}_3)_2$ building blocks to the TCPP spacers as the MOF forms.

The analysis of the N 1s spectra sequence is consistent with the Cu 2p series. The initial N 1s spectrum (red) of the SAM shows a broad peak at about 400.1 eV, which confirms the deposition of MP on the Au surface. The N 1s spectra measured during the growth of the MOF film (green spectrum) during experiment (A) exhibit distinctly different emission features that are attributed to a molecule containing pyrolic (-NH-) and iminic (-N=) nitrogen species. These are strong indicators that an interaction between Cu atoms and TCPP molecules took place. These emission lines are located at 397.9 eV and 399.8 eV, respectively; which are in a close agreement with other experiments found in the literature [84],[85]. The shift of Cu 2p to higher binding energies and the N1s to lower binding energies indicate that electrons were donated from the copper atoms to the TCPP molecules , as electron loss usually results in higher binding energies [70].

In summary, the XPS data clearly show that a layered self-assembly process of a MOF structure occurs between the $\text{Cu}(\text{NO}_3)_2$ and TCPP molecular units when $\text{Cu}(\text{NO}_3)_2$ is deposited on the surface before the TCPP incubation steps. When $\text{Cu}(\text{NO}_3)_2$ and TCPP are directly mixed in solution, this process does not occur, possibly due to the formation of 3D MOF structures in solution which do not deposit on the presented SAM surfaces.

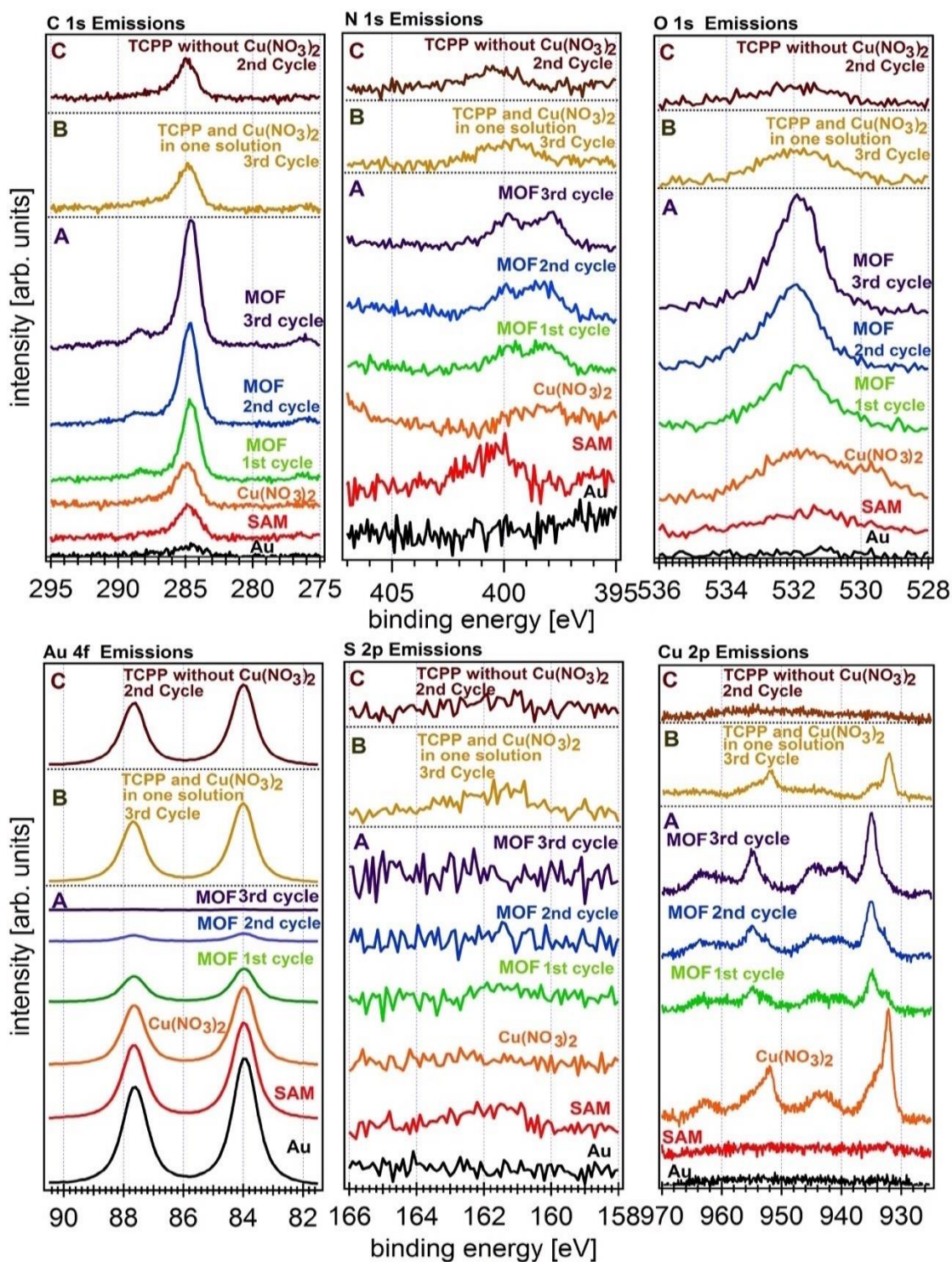


Figure 19 C 1s, N 1s, O 1s, Au 4f, S 2p, and Cu 2p core level XPS spectra measured before and after step-by-step incubation on the functionalized Au substrate (A) in the $\text{Cu}(\text{NO}_3)_2$ solution, then in the TCP solution for three cycles sequentially, (B) in both the $\text{Cu}(\text{NO}_3)_2$ and the TCP solution for three cycles sequentially, and (C) only in a TCP solution for two cycles. Adapted with permission from [40]. Copyright 2016, American Chemical Society.

4.4.2 LIXPS, UPS, and IPES Measurements

Prior to each XPS measurement sequence, the samples were characterized with UPS and LIXPS. LIXPS uses the XPS, an X-ray gun in its standby setting, i.e. uses a very low photon density. This low density is still enough to perform a successful measurement of the secondary edge, i.e. the work function can be detected. This approach allows the detection of charging artifacts that often occur during UPS measurements due to the relatively high photon density of UV sources. Especially on organic materials this can be an issue due to the often-low conductivity of these materials, which prevents the effective replenishment of photo extracted electrons. This causes charging, which manifests itself in peak shifts. LIXPS is much less affected by charging phenomena, i.e. comparing UPS, and LIXPS work function measurements reveal the onset of charging artifacts in UPS measurements [86], [87].

The UP- and LIXP-spectra measured in conjunction with the XPS spectra of Figure 19 are shown in Figure 20. The center graph shows the full UP-spectra measured after each experimental step. The left graph shows the corresponding LIXPSa and LIXPSb (dashed lines) spectra as measured before and after the UPS measurements, respectively. The right part of the figure shows the valence bands/HOMO regions of the spectra. 0 eV represents the Fermi energy.

The secondary edge feature of the LIXP-spectra, located between 16 and 18 eV, is defined by the work function of the sample (Figure 20, left panel). Each incubation cycle produced intense spectral lines corresponding to the frontier orbital states of the deposited molecules, while strongly attenuating the Au emissions. The secondary cutoff shifted to higher binding energy after each of the incubations, indicating a decrease in the Au surface work function due to the interaction between the surface and the MOF film.

The work functions were determined after each incubation step by measuring the high binding energy cutoff at the secondary edge where the spectra ends are located. This value is 15.9752 eV in case for Au. Hence, the work function can be determined by: the difference between the energy of the UV photons (21.2182 eV for He I excitation energy) and the Au binding energy (black spectrum) of the secondary edge 15.9752 eV, and by adding the analyzer broadening (analyser correction factor) of approximately 0.1 eV. Similarly, the resultant work function values after depositing the SAM and MOF layers, 4.3 eV and 5.16 eV respectively, and these were determined from the LIXPS measurements rather than the UPS measurements to avoid any charging artifacts or photochemical surface modifications that can occur during the UPS measurement.

The valence bands and the HOMO regions after background subtraction are shown in Figure 20, right panel, the bottom (black) spectrum shows the typical emissions for a clean Au surface after in situ sputtering. After step-by-step incubations of the metal ions and the organic ligands, the Au features are attenuated and replaced by emissions related to the valence bands/HOMO levels of the SAM film (red spectrum) and the MOF film (green, blue, and purple spectra).

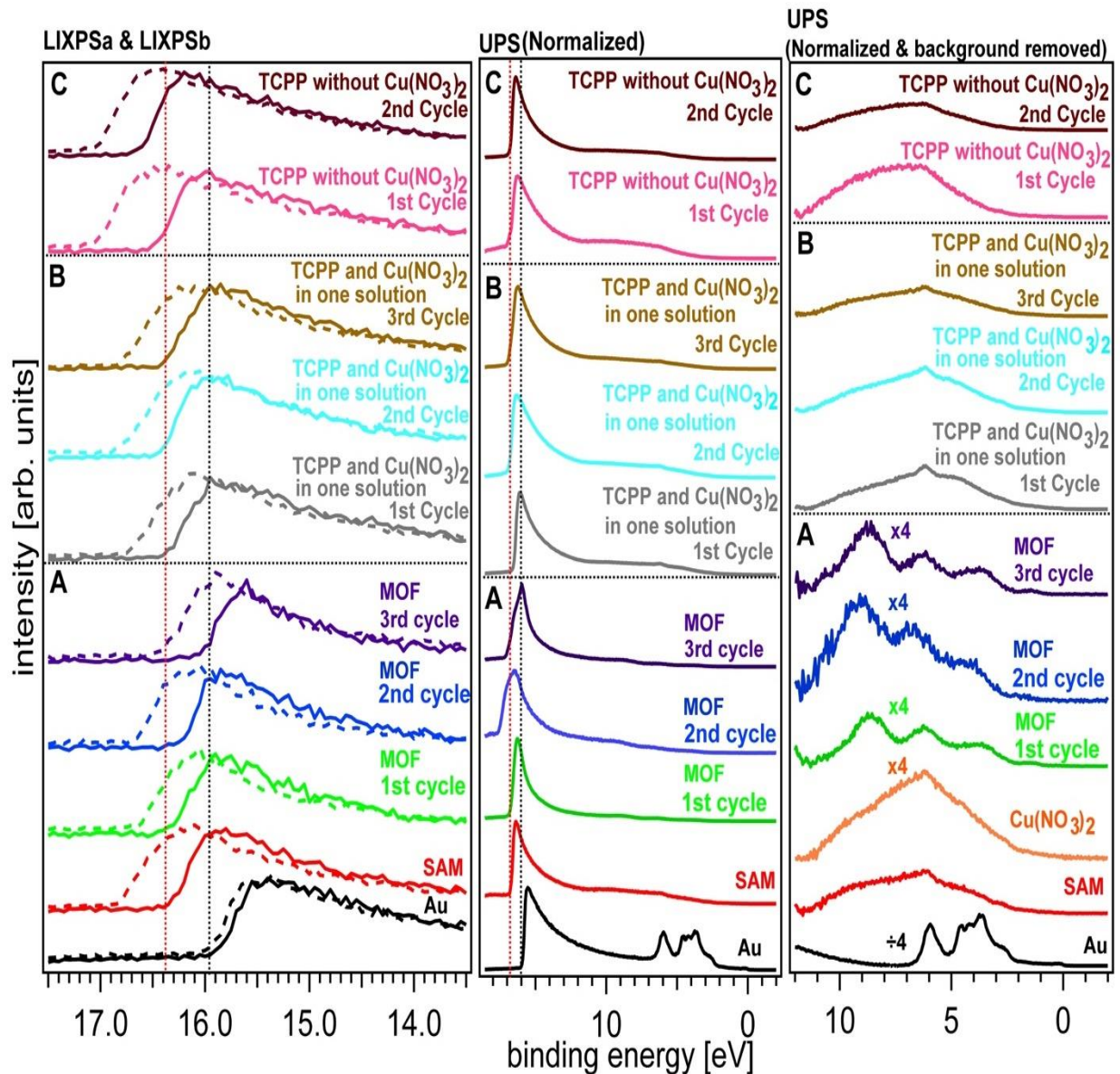


Figure 20 LIXPS and UP spectra before and after step-by-step incubation of sputter cleaned Au functionalized substrate in: (A) in the metal ion $\text{Cu}(\text{NO}_3)_2$ then in the organic ligands TCPP for three cycles sequentially, (B) in both the metal ion and the organic ligand solution for three cycles sequentially, and (C) only in a TCPP solution for two cycles. Their normalized secondary edges were measured with LIXPS before (LIXPSa) and after (LIXPSb) UPS and are shown in the left panel. The complete normalized UP spectra are displayed in the middle. The right panel shows the evolution of the valence band/HOMO emission features through the deposition process. Adapted with permission from [40]. Copyright 2016, American Chemical Society.

4.5 Discussion

The data show that the film only grows when the surface of the SAM substrate is ‘seeded’ for the growth process with the $\text{Cu}(\text{NO}_3)_2$ SBUs. The second control experiment (C) showed that no significant layer growth occurs during incubation in TCPP without a prior deposition of $\text{Cu}(\text{NO}_3)_2$. This is a good indicator that a MOF structure is indeed growing. This is supported by the emergence of an additional emission at about 400 eV, which indicates the formation of bonds between the $\text{Cu}(\text{NO}_3)_2$ building blocks and the TCPP molecules. Unfortunately, a direct proof of the formed layer structure was not possible with our experimental setup. Since photoemission spectroscopy experiments with in-situ preparation require the deposition of ultra-thin layers to prevent charging artifacts from occurring the available sample preparation facilities are not set-up for the deposition of films thick enough for XRD experiments. Hence, further experiments are needed to clarify the crystal structure directly.

The UPS valence bands spectra of the MOF films show a four-peak structure that closely resembles spectra measured recently on in-vacuum deposited Co metalloporphyrin multilayer films[67] and free base porphyrin[88]. However, the Cu 2p energy shifts to higher binding energies and the N1s to lower binding energies suggest that the interaction between the $\text{Cu}(\text{NO}_3)_2$ building blocks and the TCPP molecules also leads to a metallization of the porphyrin molecules. This was taken into account for the DOS calculations where both free base TCPP and CuTCPP molecules connected to Cu paddlewheels were assembled into the MOF structures. The measured UPS spectrum of free base TCPP in comparison with the calculated DOS structures of both free base TCPP and CuTCPP are shown in Figure 21, and Figure 22, respectively.

The spectrum is background subtracted and the calculated DOS curves were shifted to match the peak positions. This was necessary since the calculation was performed on a slab of the

MOF structure suspended in vacuum, while the physical film was deposited on an Au/SAM substrate, which references its electronic structure to the substrate surface via interface dipoles.

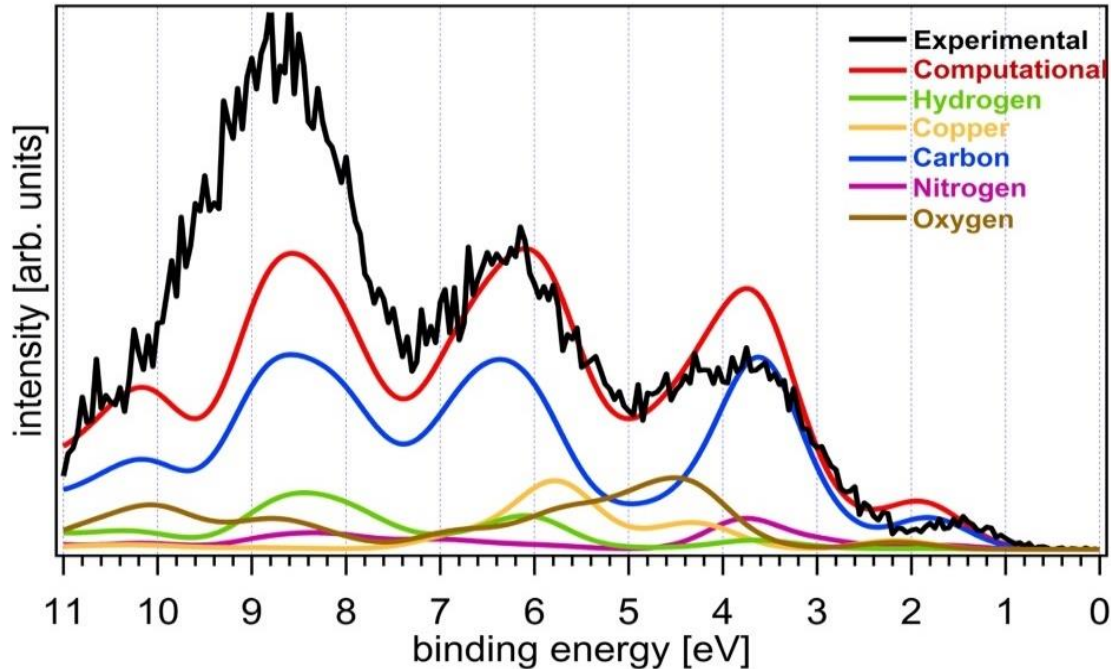


Figure 21 DOS comparison between the experimental and computational results. Four emission peaks above the Fermi level are shown in blue line from UP spectra of the MOF thin film growth consisted of $\text{Cu}(\text{NO}_3)_2$ and TCPP on top of functionalized Au substrate. The computational DOS is in red line and PDOS from each individual atomic contribution are presented with different colors. Adapted with permission from [40]. Copyright 2016, American Chemical Society.

The spectrum shows four emission peaks below the Fermi level. The peaks are at 1.5 eV, 3.75 eV, 6.35 eV and 8.75 eV in both experiment (black) and computed DOS (red). These emissions can be mainly assigned to C 2p, O1s, N 2p, Cu 2p and H 1s orbitals. This is evident from the projected DOS curves in Figure 20 and Figure 21, which show the individual contributions from each of the atomic species present in the prepared films.

The Cu 2p emission peak has a major and broader contribution from CuTCPP molecules than TCPP molecules. Not surprisingly, this peak is also the emission feature that shows the most significant differences relative to the spectrum measured on a pure TCPP film[89].

It is denoted from various experiments found in literature that there are significant similarities between UPS spectral features of metallated and H₂-porphyrin or H₂ Phthalocyanine thin films [67, 89]. This concludes that the experimental electronic structure of the deposited MOF multilayer film Figure 22 has similar distinguished spectral features compared to that of pure TPP multilayer film[67], [68], but differs from a TCPP monolayer film[90].

In the area of the Fermi edge, the experimental spectrum of CuTCPP connected to Cu-paddlewheels (black spectrum) shows a peak of the highest occupied states around 1.5 eV which agrees with the corresponding peaks in the theoretical DOS (red spectra) of free and metallated TCPP in Figure 21 and 22, respectively.

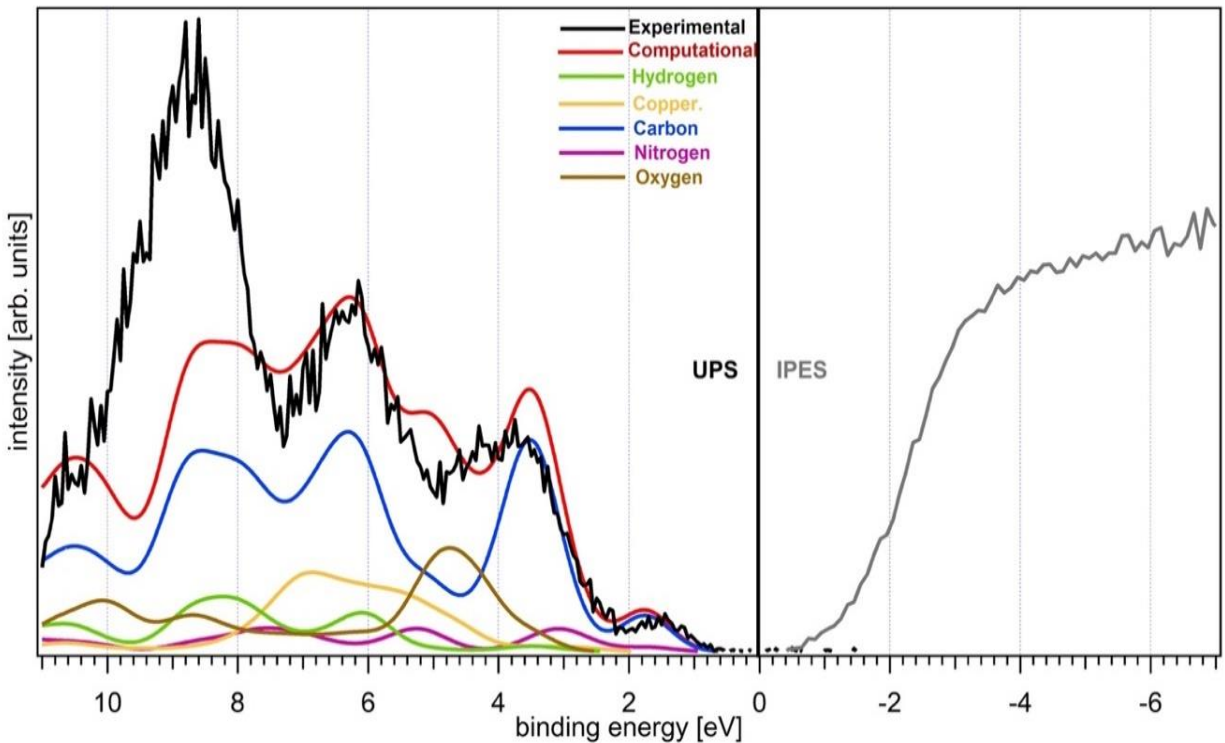


Figure 22 DOS comparison between the experimental UPS, IPES, and computational results. Four emission peaks above the Fermi level are shown in blue line from UP spectra of the MOF thin film growth consisted of Cu(NO₃)₂ and CuTCPP on top of functionalized Au substrate. The computational DOS is in red line and PDOS from each individual atomic contribution are presented with different colors. Adapted with permission from [40]. Copyright 2016, American Chemical Society.

The HOMO orbitals of CuTCPP can be seen in Figure 23a and 6b with spin-up and spin-down, respectively. The Lowest Unoccupied Molecular (LUMO) orbitals of CuTCPP with spin-up on the upper copper and the other is spin down on the lower copper paddle-wheel are shown in Figure 6c and 6d, respectively. The band gap value obtained from the DFT calculation for CuTCPP is 2.07 eV. The LUMO and HOMO of TCPP connected to copper paddle wheels can be seen as shown in Figure 6e and 6f, respectively. The corresponding band gap value obtained from the DFT calculation is 0.95 eV.

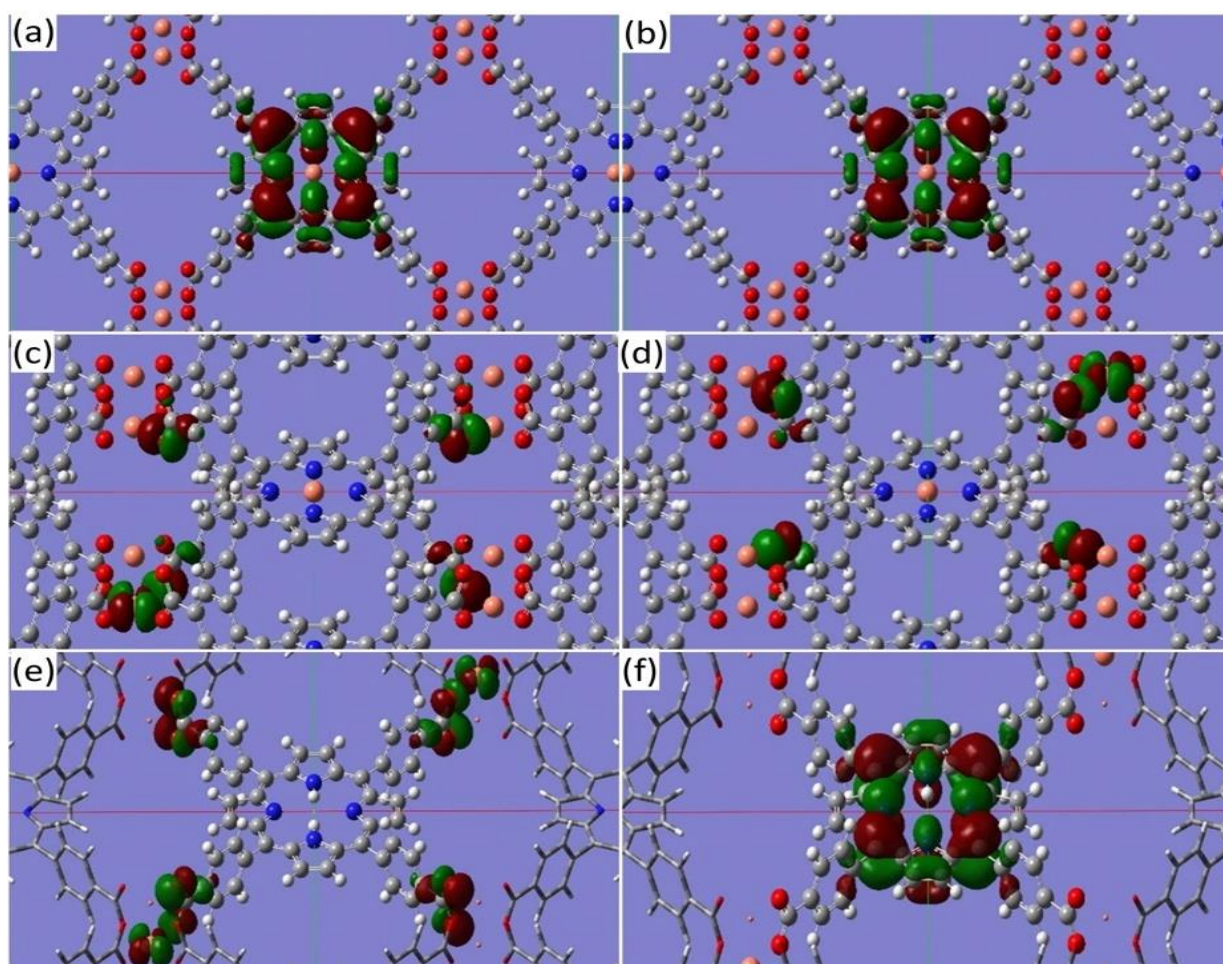


Figure 23 Computed structure of CuTCPP connected to Cu paddle wheels: a) HOMO orbital with spin-up, b) HOMO orbital with spin-down, c) LUMO orbital with spin-up, and d) LUMO orbital with spin down. Computed structure of TCPP connected to Cu paddle wheels: e) LUMO orbital, and f) HOMO Orbital. Adapted with permission from [40]. Copyright 2016, American Chemical Society.

The onset of the first UPS peak from the MOF (CuTCPP) experimental result (black spectrum) in Figure 22 located at the lowest binding energy 0.9 eV represents the hole injection barrier ϕ_h of the HOMO level at the Au functionalized surface/MOF interface, and the onset of the first IPES peak from the same experiment (gray spectrum) revealed at 1.15 eV which represents the electron injection barrier ϕ_e of the LUMO level which was shifted by 0.43 eV taking the energy resolution into account as shown in the electronic structure of Figure 24. The corresponding experimental band gap is 2.05 eV, and this agrees with the transfer gap value of 2.07 eV obtained from the full range of the computational DFT calculations of the DOS; and this also suggests that the interaction between the $\text{Cu}(\text{NO}_3)_2$ building blocks and the TCPP molecules also leads to a metallization of the porphyrin molecules. In contrast, the transfer gap values for porphyrin and its derivatives vary in the literature from 2.34 eV up to 2.9 eV[88] [69].

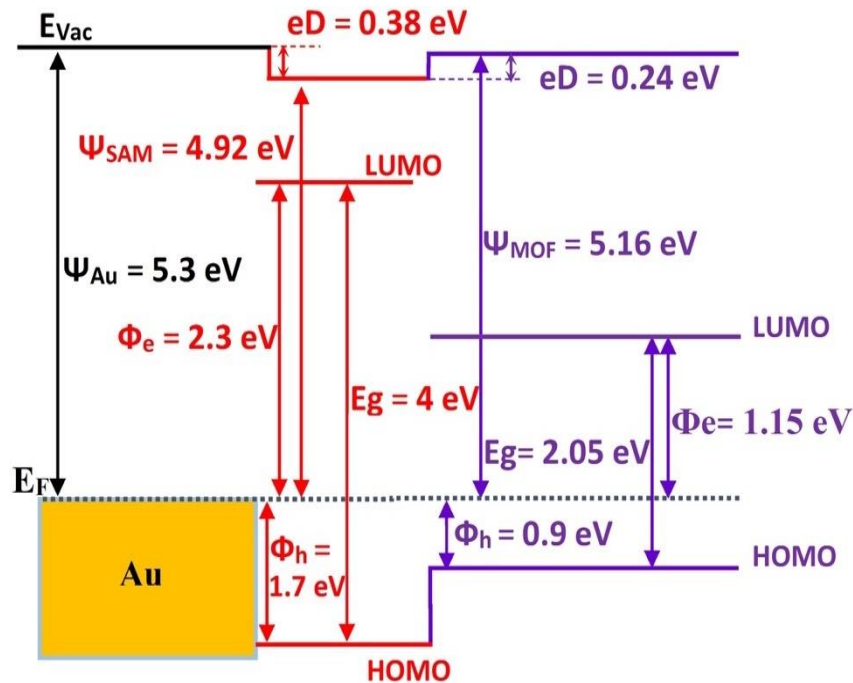


Figure 24 Electronic structure of the interface of the MOF (CuTCPP) 2D thin film grown on Au functionalized surface as determined from the UP-, IPE- and LIXP-spectra measurements. Adapted with permission from [40]. Copyright 2016, American Chemical Society.

The ionization energy (E_{ion}) of the MOF, found to be 6.06 eV, was determined by adding the resultant work function of the MOF (CuTCPP) to the hole injection barrier. Although the Fermi level is close to the HOMO of the MOF and the hole injection barrier is smaller than the electron injection barrier, it is difficult to infer the conduction type due to the low carrier density in the very thin MOF film (11.27 nm), and the energy of the frontier orbitals of the MOF layered structures depends strongly on the metal work function, and the SAM. The HOMO onset of the SAM revealed at 1.7 eV which was obtained from the UPS measurement from Figure 3 (red spectrum) and the corresponding HOMO-LUMO gap is 4-4.1 eV which was adapted from the work published in reference [91].

A scanning electronic microscope (SEM) produced an image shown in Figure 25 revealing the topography of the MOF thin film formation. Focused ion beam was also incorporated as presented in Figure 26 to support the presence of the fabricated MOF film. Out-of-plane Grazing

incidence technique (GIXRD) measurement was conducted with θ - 2θ scans at an incidence angle α of 0.2° as shown in Figure 27, and unique peaks observed from the MOF and the SAM at around 19.59° and 38.38° assigned to (002) from and (003), respectively which supports the film grows in a planer fashion to the substrate surface which concurs with GIXRD measurement reported in literature.[72, 92]

MOFs offered the possibility to form significant multilayer growth with injection barriers due to the self-organization of the MOF on top of an Au functionalized surface. The bond created between the hosting functionalized substrate surface and the MOF offers a path to charge transfer due to the hole injection barrier of 0.9 eV, and electron injection barrier value of 1.15 eV.

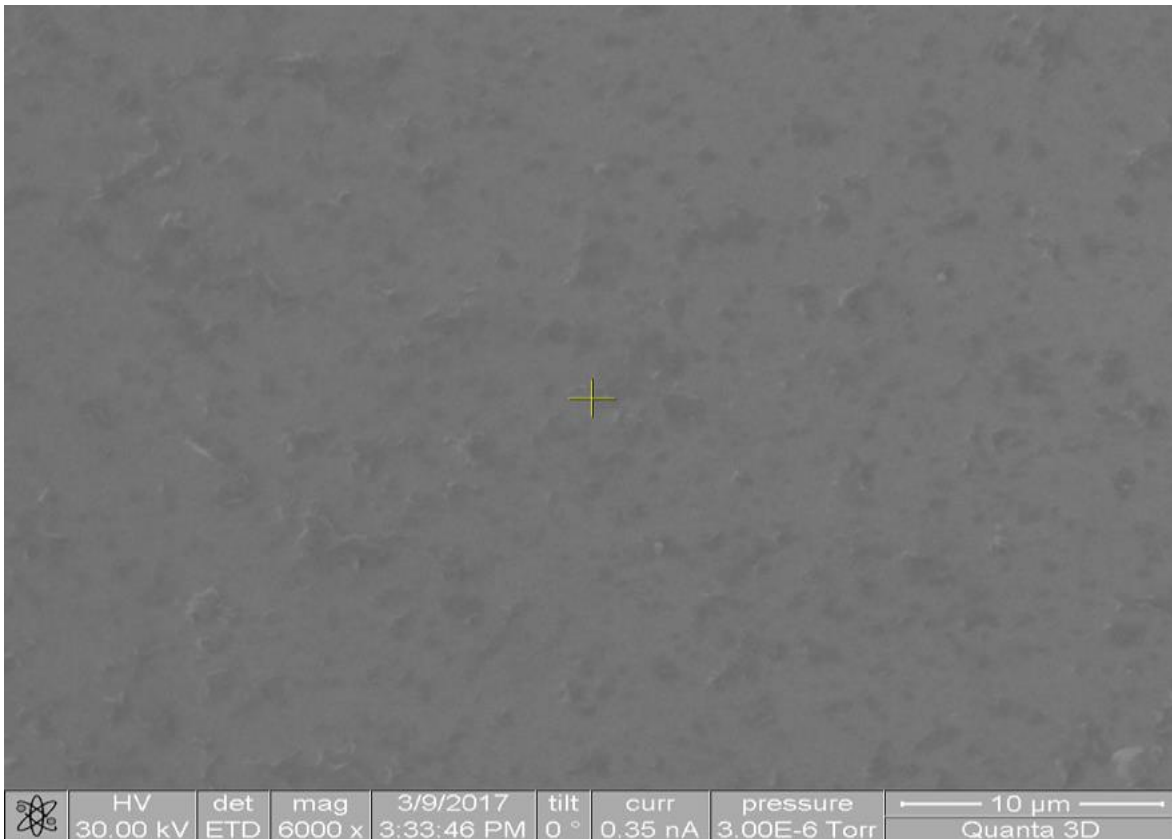


Figure 25 SEM image of MOF thin film after third immersion cycle.

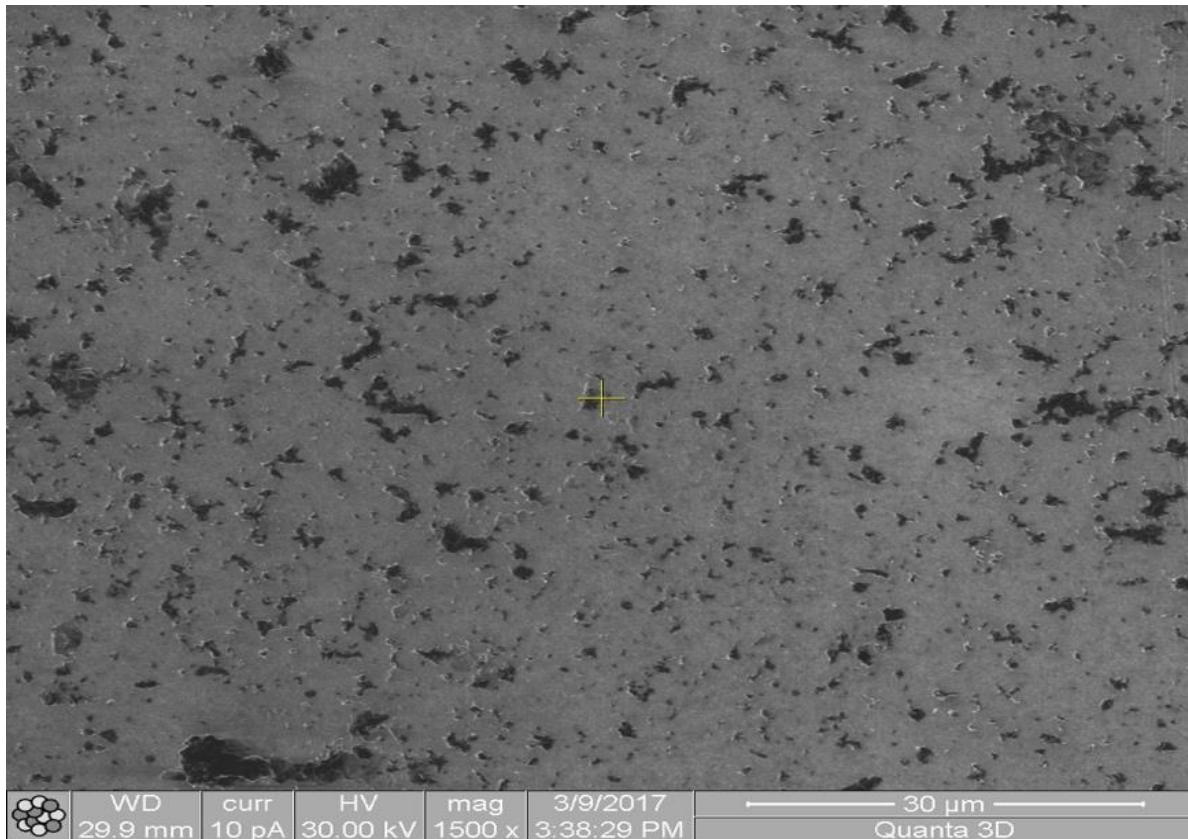


Figure 26 FIB image of MOF thin film after the third immersion cycle.

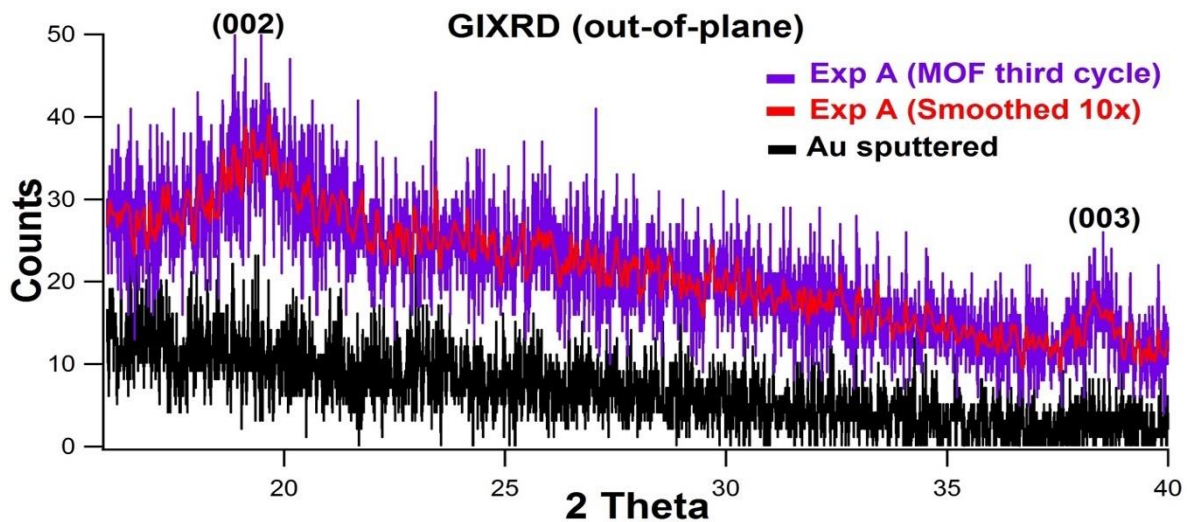


Figure 27 Out-of-plane GIXRD of MOF thin film showing (002) and (003) (top spectrum) diffractions assumed from the MOF, and SAM respectively. The bottom is a reference spectrum of Au surface.

4.6 Conclusion

Self-assembly of metal-organic framework was used to generate a self-organized conductive 2D MOF nano film on top of Au functionalized substrate via sequential step-by-step incubation cycles. The growth of the MOF film was determined by ultraviolet and X-ray Photoemission spectroscopy and compared to DFT calculations, and this represents a significant advance with unprecedented investigation.

The increase of the emission features of the C 1s, N 1s, O1s and Cu 2p and the decrease of the Au 4f, and S 2p obtained through XPS measurement after sequential incubations were reliable indicators of the adsorption and the surface coverage of the MOF film on the surface of the substrate. The control experiments determined that the metal ion, $\text{Cu}(\text{NO}_3)_2$, was an essential and suitable SBU as a linker between SAM and the arm groups of organic ligand.

The UPS results revealed the orbitals line-up of the MOF molecules bound to the surface of the Au functionalized surface, and revealed similar emission spectral features in correlation with DFT calculations. The combined results from the first onsets of UP- and IPE- spectra revealed the band gap which strongly agrees with the value obtained from DFT calculations. The orbitals line-up showed significant barriers for both hole and electron injections from the Au functionalized surface to the MOF thin film, and this is property at the interface is crucial to design and develop conductive MOF materials that can offer an important breakthrough in molecular electronic devices.

4.7 Acknowledgments

Professor Rüdiger Schlaf and Radwan Elzein gratefully acknowledge the funding from the National Science Foundation (grant# NSF DMR-1035196).

CHAPTER 5: ENERGY LEVEL ALIGNMENTS AND MODIFICATION OF INTERFACIAL ELECTRONIC STRUCTURES OF 2D AND 3D SURMOFS²

5.1 Abstract

Surface mounted metal-organic framework (SURMOF) thin films are of intensive research interest for next generation molecular nanoelectronics due to their unique diversity of highly ordered nanocrystalline structures, versatility, functionality, tailorable electronic, ionic, and magnetic properties.

Despite the significant progress in MOF materials, fundamental understanding of their electronic structures at the interface to achieve favorable energy level alignments with suitable hole or electron transport layers remained largely uninvestigated. Tuning and improving their interfacial properties can dramatically improve the performance, reliability of novel electronic devices and their practical applications. Hence, powerful and unique techniques such as direct and inverse Photoemission Spectroscopy (PES) are crucially required to access the frontier electronic structures and provide feedback on the design of SURMOF 2D-, and 3D- thin films in order to promote efficient charge injection, separation, and enhance the retention, light emission, or absorption in devices.

The presented research successfully demonstrates tuning of the electronic structures of porphyrin paddlewheel frameworks which were synthesized by liquid-phase epitaxy (LPE) on Au prefunctionalized surface with 4-mercaptopyridine (Mpy) in a glove box attached to Ultra-high

²This chapter is submitted to a journal for publication and is awaiting review.

vacuum (UHV) PES. Secondary Building Unit (SBU) based on $\text{Cu}(\text{OAc})_2$ paddlewheeled to free-base-, and metalated- conductive ligands (5,10,15,20-tetrakis(4-carboxyphenyl) porphyrin) MTCPP (M= Co, Ni, or free metal) to build 2D SURMOF. Pillaring linkers Pyrazine (Pz) and 4,4'-Bipyridine (Bipy) were embedded in between the 2D frameworks which led to the construction of 3D SURMOFs.

Systematic intentional modifications of interfacial electronic structures of the fabricated films were characterized by LIXPS, UPS, and IPES which demonstrate unprecedented energy level alignments at the SURMOF interfaces. Evidence of the thin film growth and interactions was observed by XPS. Thus, these exceptional understandings of tailored HOMO-LUMO levels, transfer gaps, work function values, interfacial dipoles, ionization potentials, and electron affinities provided a unique feedback on the designed SURMOFs. The correlated results provide a significant advancement and breakthrough to develop novel electronic devices requiring tunability with opportunity to integrate complex functions.

5.2 Introduction

MOFs have been a major focus of contemporary materials research in recent years which are attractive for various electronic devices [15, 16, 93-95] and applications. [96, 97] MOFs exhibit interesting electronic, ionic, and magnetic [98, 99] properties, and offer exceptional nanoscale porosity which enables selective mass transfer throughout the material. In the context of electronic materials this offers an additional charge transfer path via ion transfer. These properties offer interesting opportunities for the design of the next generation of molecular-scale electronics. Their versatile nature also enables diversity of rich structures with different dimensionalities, they can be deposited over extremely large surface areas, possess mechanical flexibility, and are lightweight materials offering low production cost using various thin film deposition techniques.

The presented research aims to shed more light on the electronic properties of conductive MOF materials using photoelectron spectroscopy combined with in-situ preparation of MOF structures. This method has been successfully applied to complex organic materials in recent years making it an interesting approach for the investigation of the electronic properties of conductive MOF structures. Examples of such PES measurements are experiments on conjugated polymers Poly[2-methoxy-5-(2-ethylhexyloxy)-1,4-phenylenevinylene](MEH-PPV),[100,101] Polythiophene (P3HT),[102] and biomolecules such as ribonucleic acid (RNA),[103] homopolymers[104] and peptides,[105] TiO₂,^[86] CdSe nano-crystals,[106] and recently on a SURMOF 2D thin film.[40] Despite the significant breakthroughs in synthesizing conductive MOFs,[14] the fundamental understanding of their electronic properties in contact with other materials at interfaces remains largely uninvestigated. The energy level alignment between metal electrodes and MOFs controls charge carrier injection, the strength of internal electric fields for ionic transport through the materials. Hence, surface science techniques such as direct and inverse (PES) are crucial to study the frontier energy levels and to give a feedback on the design of SURMOFs.

Among a wide variety of organic conductive ligands presented in the literature,[14-16] porphyrin molecules [17, 18, 107] are attractive candidates in building conductive MOF nano thin films on wafer surfaces due to the diversity of their molecular structures, functionalization, core metalation, tunability, and they are excellent hosts for guest confinements such as electrolyte ions within the pores. In turn, SURMOFs based on porphyrin derivatives are suitable for molecular electronic applications due to their semiconductive, and redox properties, which comprise π -cation radicals and multiple cationic states and their capability to transport and store charges for extended periods. In this work, porphyrin paddlewheel frameworks were synthesized by Liquid Phase Epitaxy (LPE) using free base and metalated conductive organic ligands (5,10,15,20-

tetrakis(4-carboxyphenyl) porphyrin) MTCPP (M= Co, Ni, or free metal), and SBU based on $\text{Cu}(\text{OAc})_2$ were incorporated to construct conductive 2D SURMOFs. Whereas, further integration of various organic pillaring linkers such as Pz or Bipy between the 2D frameworks led to the construction of 3D SURMOFs with remarkable change in electronic properties. The self-assembled 2D and 3D thin films were deposited from solutions via sequential step by step synthesis on pre-functionalized gold surfaces with 4-mercaptopyridine (Mpy) in a glove box attached to PES as demonstrated in the experimental section. The resultant electronic structures of the SAM, 2D-, and 3D- SURMOFs and their chemical interactions at the interfaces were characterized by the following surface science techniques: low intensity XPS (LIXPS) which revealed information about work function values, ultraviolet photoemission spectroscopy (UPS) gave valuable insights about both the binding of HOMO energy levels and the work function values, XPS revealed the interfacial chemical interactions and monitored the film growth, and inverse photoemission spectroscopy (IPES) provided information about the LUMO energy levels. The obtained results provide crucial information that SURMOFs uncover a significant tuning of their electronic structures and energy level alignments relevant to Fermi level through selection of MOF components by two approaches (i) various metalated TCPP cores, and (ii) different pillaring linkers.

In this context, seven MOF experiments were conducted and their corresponding energy band diagrams were extracted from the PES measurements, which revealed essential understanding of the electronic properties that SURMOFs show unique tunability to switch from p-type to n-type material, and can conduct positive charge carriers (holes) and negative charge carriers (electrons), respectively. The result findings allow for the creation of functional electronic materials via designing hybrid hetero-junction structures with internal donor-acceptor properties

and redox shuttle mediators acting as solid-state electrolytes. The transfer band gap values of the fabricated 2D and 3D films demonstrate tunability ranging from 0.84 – 2.8 eV, which makes it attractive to fabricate and develop hybrid and Tandem Dye-Sensitized solar cells fulfilling good responsivity to wide light absorption. Other interesting applications that rely on multi-heteroepitaxial systems where MOFs can satisfy the requirements of low and high work functions with donor and acceptor properties are thermoelectric convertors and memristors. Therefore, MOF materials can open up the possibility to adapt heterogeneous integration of new technologies with particularly attractive complex functions.

5.3 Experimental Section

5.3.1 Materials: MOF Materials and Synthesis

$\text{Cu}(\text{OAc})_2$ and MTCPP (5,10,15,20-tetrakis(4-carboxyphenyl) porphyrin); 4-mercaptopyridine (96%), 4,4'-Bipyridine, Pyrazine, as well as anhydrous ethanol were purchased from Fisher Scientific. The N,N-dimethylformamide (DMF), (ACS, 99.8+%) was obtained from Alfa Aesar, and the thin film Au (100 nm Au deposited on a 20 nm Ti adhesion layer on glass slides) substrates were purchased from EMF Corp. (Ithaca, NY).

5.3.2 Deposition Technique

LPE conducted previously on functionalized surfaces[41], is adapted in the physical experiments as modular step by step assembly process. It offers a high level of control over chemical functionalization and yields preferred nanocrystal orientation.[22, 23] MOFs were also mounted on various terminating functional groups (e.g., -N,[40] -NO₂, -NH₂, -COOH, and -OH moieties)[41] as reported in literature on a wide variety of surfaces, and this process is compatible with vacuum technology and nanofabrication, and was successfully performed in a glove box attached to surface science system (PES) for in situ-measurements.

5.3.3 In-situ Film Preparation

Glass slides coated with 5 nm Ti adhesion layer and 100 nm Au thin film were cut into 1×1 cm² squares by diamond scribing, then mounted onto a sample holder and fixed on the corners via screws. This enabled good Ohmic contacts between the Au film and the chamber ground to avoid charging during PES measurements. Three-step cleaning process using acetone, methanol, and deionized water was performed on the Au samples to remove organic impurities, dust particles, and minimize contamination, followed by drying with a 99.995% N₂ gun prior to sputtering step. The solvent-cleaned samples were entered a homemade acrylic glovebox filled with 99.995% N₂ and was kept under slight overpressure to suppress sample contamination from the ambient environment during film growth. The glovebox is attached to the fast entry load lock to enable a direct transfer of the solvent-cleaned samples into the PES chamber.

5.3.4 Direct and Inverse PES System

All PES experiments were carried out in a multichamber system (SPECS Nano Analysis GmbH, Berlin, Germany) under UHV conditions (2×10^{-10} mbar base pressure). The system consists of a fast entry load lock, transfer chamber for sputtering, and analysis chambers equipped with X-ray, ultraviolet, and inverse photoemission spectroscopy (XPS, UPS, and IPES respectively). After transferring the solvent-cleaned samples from the glove box into UHV chamber, the Au surfaces were sputtered with Ar plasma using SPECS IQE 11/35 ion source with a kinetic energy of 5 keV and an emission current of 20 mA at 9×10^{-6} Torr for 40 min, then the cleaned Au surfaces, were transferred to analysis chambers for PES characterization sequence beginning with an LIXPS measurement (Mg K, 1253.6 eV, standby mode: 0.1 mA emission current), followed by UPS (He I, 21.2182 eV), then XPS (Mg K, 1253.6 eV, 20 mA emission current), and finally an IPES measurement (electron gun, Kimball ELG-2/EGPS-1022, and a

Geiger counter with an energy resolution of about 0.43 eV). This analysis was performed to establish a reference measurement of the Au surface before the film growth. The deposition process started by transferring the sputtered Au sample back to the glove box for the SAM incubation. The sample was placed in a vial containing the 1mM SAM solution of Mpy in ethanol which was pre-sonicated in ultrasound bath at 40 °C for 15 min. The vial was sealed and kept in the glovebox at room temperature, then the sample was removed from SAM solution after 20 min, and dried with a stream of 99.995% N₂ prior and post rinsing step with ethanol. The prefunctionalized sample with Mpy was loaded back into the analyzing chamber for PES measurement, then it was sent out to the glove box for the MOF incubation.

5.3.5 2D MOF Experiment

Experiment A (Exp A) consisted of four different samples (S1-S4) as depicted in Figure 28. The prefunctionalized Au substrates were alternately immersed into the metal ion solution (13.329 mM Cu(OAc)₂ solution in DMF) for 30 min followed by an immersion step in various organic ligand solutions (1.2645 mM MTCPP in DMF, where M: free metal, Ni, or Co) for an additional 1 h, three-six sequential incubation cycles were performed in the glovebox at room temperature. In between each immersion step, the substrate was dried in a stream of 99.995% N₂ prior and post rinsing step with EtOH to remove unreacted chemical species. Following each individual immersion cycle, the surface was characterized with the LIXPS/UPS/XPS/IPES measurement sequence.

5.3.6 3D MOF Experiments

Experiment B (Exp B) consisted of three different samples (S1-S3) as depicted in Figure 28: The pre-functionalized Au surfaces were alternately immersed into the metal ion solution (13.329 mM Cu(OAc)₂ solution in DMF) for 30 min followed by an immersion step in the

corresponding organic ligand solution (1.2645 mM TCPP or CoTCPP in DMF) for an 1 h, then in the pillaring linker solution (0.05 M of Pz or Bipy solution in EtOH) for additional 30 min. Three-six incubation cycles followed by drying-rinsing-drying sequence identical to experiment (A), then each sample was transferred into attached UHV systems for PES and IPES measurements.

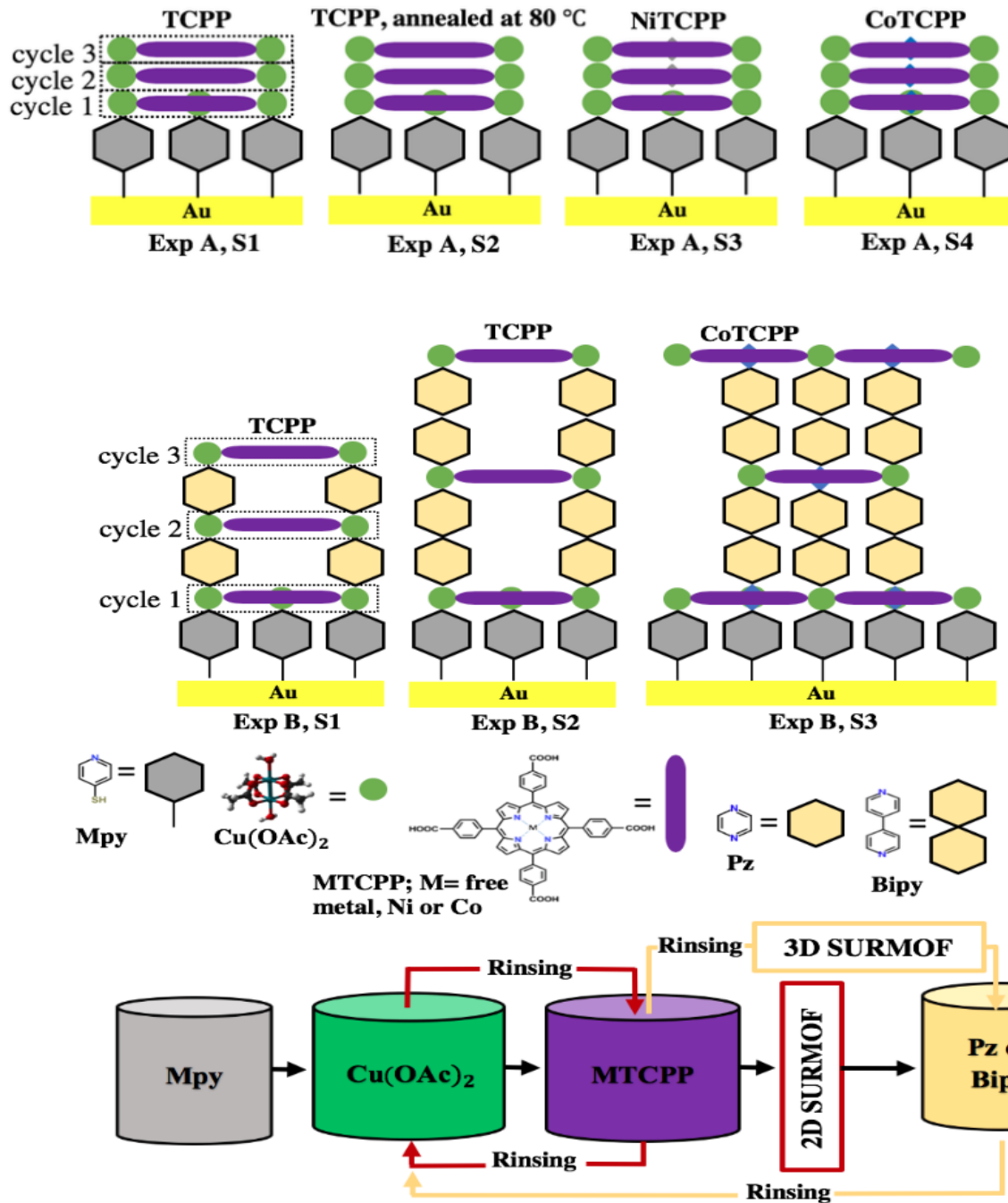


Figure 28 Schematic depiction of idealized 2D and 3D SURMOF growth sequence in a glove box: Films were grown by incubation on Mpy SAM-terminated Au surfaces. Four samples in Exp A (S1-S4) were incubated in the same metal ion solution, followed by immersions into the corresponding organic ligand solution (MTCPP, where M: Ni, Co, or free metal) for 2D SURMOF films; and by incorporating pillaring linkers (Pz or Bipy) led to 3D SURMOF film construction. Each incubation step was completed by rinsing the sample in EtOH, then each sample was transferred into UHV PES system for characterizations.

5.4 Results and Discussion

5.4.1 Work Function Measurements by LIXPS

Work function measurements by LIXPS. LIXPS uses the XPS, an X-ray gun in its 'stand by mode' (Mg K, 1253.6 eV, 0.1 mA emission current) to perform successful work function measured from the secondary edges located between 16 and 18 eV of the spectra by fitting straight lines into their low kinetic energy cut-off which is formed by inelastic scattered photoelectrons, and by determining the intersect with the base line of the spectra. This technique prevents the detection of charging artifacts in low conductive samples that cause peak shifts during UPS measurements. The spectrum in Figures 29 and 30 shows LIXPSa (single lines), and LIXPSb (dashed lines) spectra as measured prior and post UPS measurements, respectively of four samples of Exp A (S1-S4), and three samples of Exp B (S1-S3). The values of the work functions are determined by the difference between the energy of the UV photons (21.2182 eV for He I excitation energy) and the binding energy edges of the corresponding spectra. The analyser broadening of ± 0.1 eV was added to the work function values. All calculated data evaluations of the spectrum shown in Table S1 were acquired by Igor Prof software (Wavemetrics).

5.4.1.1 Work Function Measurements of 2D SURMOFs

The resultant work function values of Exp A, S1 are derived from LIXPSa as shown in Figure 29 and revealed at a value of 4.77 eV after the third incubation cycle in TCPP (Cycle 3). However, after annealing the same sample (Exp A, S2) at 80 °C the work function value from LIXPSa (cycle 3) was increased by 0.1 eV, and expected charging artifact observed in UPS measurement causing the secondary edge to shift down to lower binding energy by 0.89 eV. The resultant work functions values of NiTCPP (Exp A, S3) and CoTCPP (Exp A, S4) ligands obtained after the third incubation cycles (cycle 3) are 4.59 and 4.88 eV, respectively. This trend of

increasing in work function values occurred systematically from TCPP, then with changing the metalloporphyrin ligand from NiTCPP, to CoTCPP.

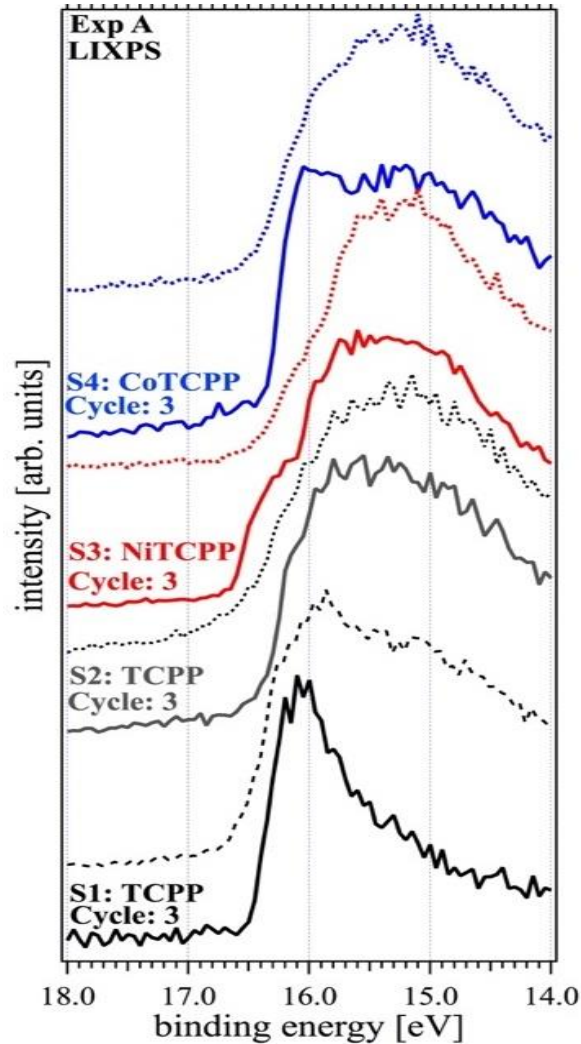


Figure 29 LIXPSa was measured before (single lines) and LIXPSb after (dashed line) UPS measurements after incubation of the functionalized Au surface in: $\text{Cu}(\text{OAc})_2$, and then in the corresponding organic ligand or pillaring linker solutions. Exp A shows resultant work function measurements of four samples (S1-S4) after third incubation cycles in the corresponding ligand solutions of TCPP, TCPP (control), NiTCPP, or CoTCPP, respectively.

5.4.1.2 Work Function Measurements of 3D SURMOFs

The resultant work function of Exp B, S1 derived from spectrum shown in Figure 30 (left panel) which belongs to TCPP when pillared with Pz molecule after the third incubation cycle

(cycle 3) is 4.77 eV. However, when Bipy molecule was used (Exp B, S2) the work function value of the same organic ligand has decreased to 3.72 eV illustrated in Figure 30 (middle panel). This implicates a lengthier pillaring linker incorporates in decreasing the work function of the resultant MOF thin film. Furthermore, when ligand was replaced by CoTCPP pillared with Bipy (Exp B, S3), its resultant work function value is decreased to 4.52 eV in comparison with free base TCPP ligand (Exp, S2).

It is denoted that in all LIXPS experiments that post each incubation cycle, the secondary cut-off shifts to higher binding energies which is an indication of reduction in the Au work function as the MOF layers grow, charging artifacts observed in UPS measurements, for this reason work function values obtained from LIXPSa spectra should be taken into accounts. Furthermore, the work function of TCPP molecule can be tuned by using various core metals or pillaring linkers to match between the work function of MOF material and that of the substrate to achieve efficient hole or electron transport properties.

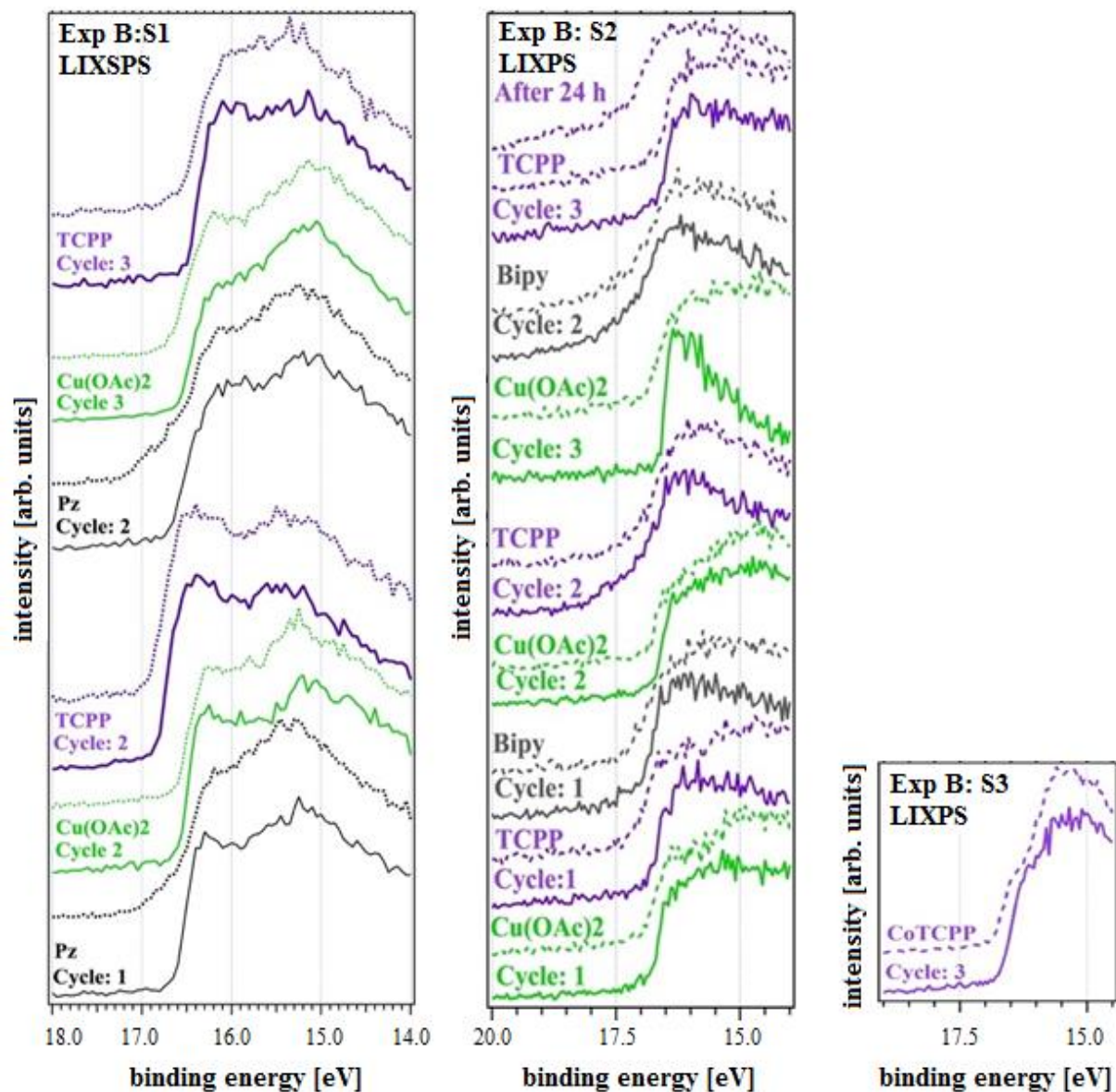


Figure 30 LIXPSa was measured before (single lines) and LIXPSb after (dashed line) UPS measurements after incubation of the functionalized Au surface in: $\text{Cu}(\text{OAc})_2$, and then in the corresponding organic ligand or pillaring linker solutions. Exp B shows measurements of three samples S1 (left panel), S2 (middle panel), and S3 (right panel) post each incubation cycle in MTCPP (M= free metal, or Co) with pillaring linkers of Pz, or Bipy.

Table 1 Comparison between the resultant work function values from LIXP-, IPE, and UP-spectra measurement of 2D and 3D SURMOFs obtained from Exp A (S1-S4), and Exp B (S1-S3). Exp A (S1-S3) shows work function values after incubation cycles in ligand solution of TCPP, NiTCPP, or CoTCPP, respectively; Exp B (S1-S2) show measurements post each incubation cycle in TCPP, and pillaring linkers of Pz, or Bipy.

	Work function (eV)	LIXPSa	UPS	LIXPSb
Exp A, S1	Au	5.34	5.38	5.34
	SAM	4.32	4.07	3.90
	Cu (cycle 1)	4.43	4.21	4.30
	TCPP (cycle 1)	4.47	4.23	4.25
	TCPP (cycle 3)	4.77	4.66	4.69
Exp A, S2	TCPP (cycle 3, annealed)	4.88	3.76	4.65
Exp A, S3	NiTCPP (cycle 3)	4.59	4.61	4.72
Exp A, S4	CoTCPP (cycle 3)	4.88	4.73	4.73
Exp B, S1	Pz (cycle 1)	4.65	4.58	4.49
	Cu (cycle 2)	4.69	4.45	4.62
	TCPP (cycle 2)	4.44	4.50	4.33
	Pz (cycle 2)	4.56	4.41	4.25
	Cu (cycle 3)	4.68	4.78	4.56
	TCPP (cycle 3)	4.77	4.44	4.67
Exp B, S2	Bipy (cycle 1)	4.36	3.56	3.94
	Cu (cycle 2)	4.43	3.73	4.18
	TCPP (cycle 2)	4.21	2.73	3.90
	Bipy (cycle 2)	4.12	2.82	3.76
	Cu (cycle 3)	4.46	3.18	4.36
	TCPP (cycle 3)	3.72	2.17	3.90
	Bipy (cycle 3)	3.67	0.76	3.58
	Cu (cycle 4)	4.66	1.99	4.22
	TCPP (cycle 4)	4.54	2.48	4.48
Exp B, S3	CoTCPP (cycle 3)	4.52	4.06	4.44

A comparison between the work functions with charging artifacts from UPS measurements plotted as shown in Figure 31. The obtained work function values of 2D and 3D MOF films show increase in their work functions as the multilayers form relative to the work function of the Au surface, and this upward shift was also demonstrated by Yun Bai et al on porphyrin films.[108]

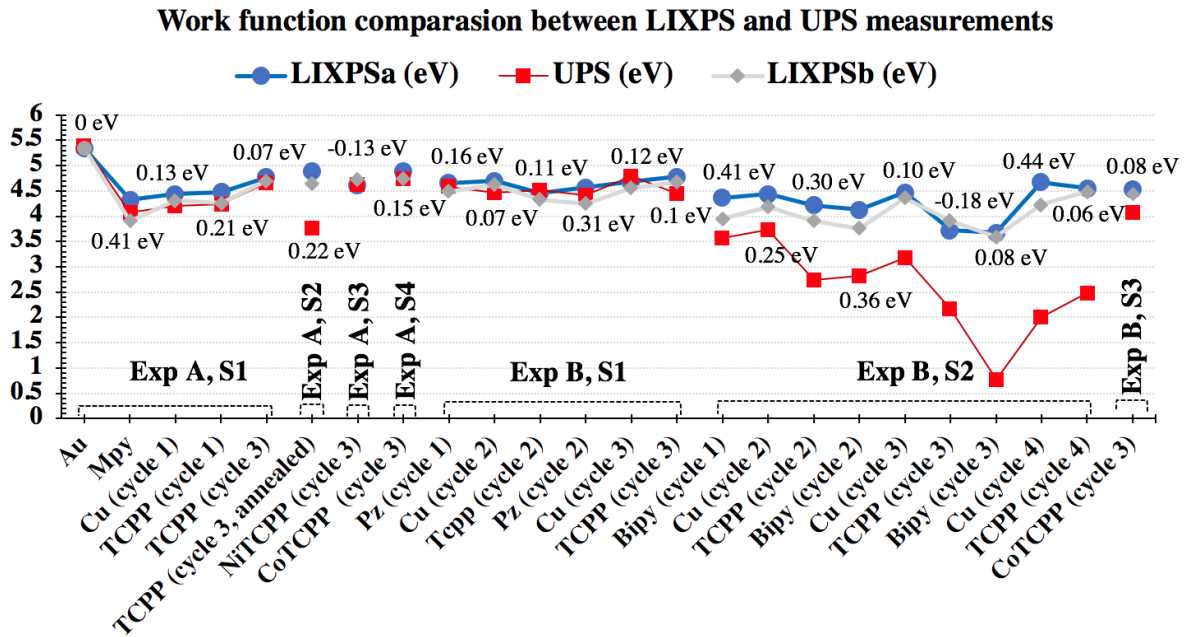


Figure 31 Comparison between the resultant work function values from LIXP-, IPE, and UP-spectra measurement of 2D and 3D SURMOFs obtained from Exp A (S1-S4), and Exp B (S1-S3). LIXPSa, blue line; LIXPSb, gray line; UPS, red line. Charging artifacts are observed when LIXPSb does not shift back after UPS measurement. Hence, LIXPSa data should be taken into account. The difference between LIXPSa and LIXPSb values are labeled.

5.4.2 UPS and IPES Measurements

The samples in each experiment were characterized post LIXPSa measurements by UPS. The UP-spectrum were normalized and the HOMO regions after background subtractions are revealed above Fermi level. The work function values from UPS measurements in Table 1 were derived from the locations of the cut-off features by fitting procedures, and the values obtained were adjusted by the analyzer broadening factor. The black spectrum in Figure 37 shows typical emissions for a clean Au surface after in situ sputtering, these features were replaced by features

which attributed to the SAM, porphyrin derivatives (organic ligands), and pillaring linkers after samples' incubation. The presented UPS valence bands of the 2D and 3D MOF thin films spectra reveal distinguished and discernible a four-peak feature which are similar to conventional porphyrin films reported in literature[109],[110],[111],[40].The shape of these peaks indicates the growth of multilayered structures and this is supported by the absence of Fermi edge as demonstrated by Gottfried et al[67]. and Friesen[112]. The energy gap between free base and metalated porphyrin ligands decreased from TCPP, to NiTCPP, and CoTCPP due to the porphyrin occupied and unoccupied molecular orbitals, and their redox states that are sensitive to the energy of 3d-orbitals of various core metals as explained by M.-S.Liao and co-workers[113]. The incorporation of pillaring linkers Pz and Bipy with axial ligations have significantly modified the electronic structures of MOF films. These modifications have substantial influence on the alignments of HOMO and LUMO levels relevant to the fermi level as demonstrated in the energy diagrams of 2D and 3D SURMOFs.

5.4.2.1 Valence and Conduction Bands of 2D SURMOFs

UP-and IPE spectra of four samples fabricated with the same metal ion $\text{Cu}(\text{OAc})_2$ paddlewheeled to various organic ligands as shown in Exp A, S1: TCPP; S2: TCPP (annealed at 80°C); S3: NiTCPP; and S4: CoTCPP are shown in Figure 32. Their corresponding work function values derived from the UPS secondary cutoff edges after third incubation cycles are 4.66, 3.76, 4.61, and 4.73 eV respectively, these values roughly agree with the work functions obtained from LIXPS measurements (except for the annealed sample, S2), and their corresponding transfer band gap values are 2.05, 2, 1.35, and 0.84 eV, respectively. The band gap value of $\text{Cu}(\text{OAc})_2$ coordinated to TCPP molecules (Exp A, S1) found at 2.05 eV agreed very well with the band gap value of 2.05 eV reported from $\text{Cu}(\text{NO}_3)_2$ with the same organic ligand.[40] In contrast, the optical

band gap value of TCPP molecule is 2.9 eV which was obtained from UV-Vis spectrophotometry in literature,[114] the low band gap value is due to the presence of $\text{Cu}(\text{OAc})_2$ in a MOF structure. The transfer band gap value of $\text{Cu}(\text{OAc})_2$ coordinated to NiTCPP ligand (Exp A, S2) revealed at 1.35 eV which differs from the optical band gap values of 2.9-3.06 eV found in literature[115]; however, the reported ligand (NiTCPP) was adsorbed on TiO_2 surface and without SBUs. The transfer band gap value of $\text{Cu}(\text{OAc})_2$ coordinated to CoTCPP ligand (Exp A, S4) revealed at 0.84 eV in contrast to the optical band gap values varied between 2.4-3.1 eV in literature.[116, 117] This implicates that various core metals in the porphyrin rings[113], and the presence of chosen metal nodes contributed to alter the HOMO/LUMO values, and that guides significantly to tunable transfer band gaps of the fabricated 2D MOF thin films.

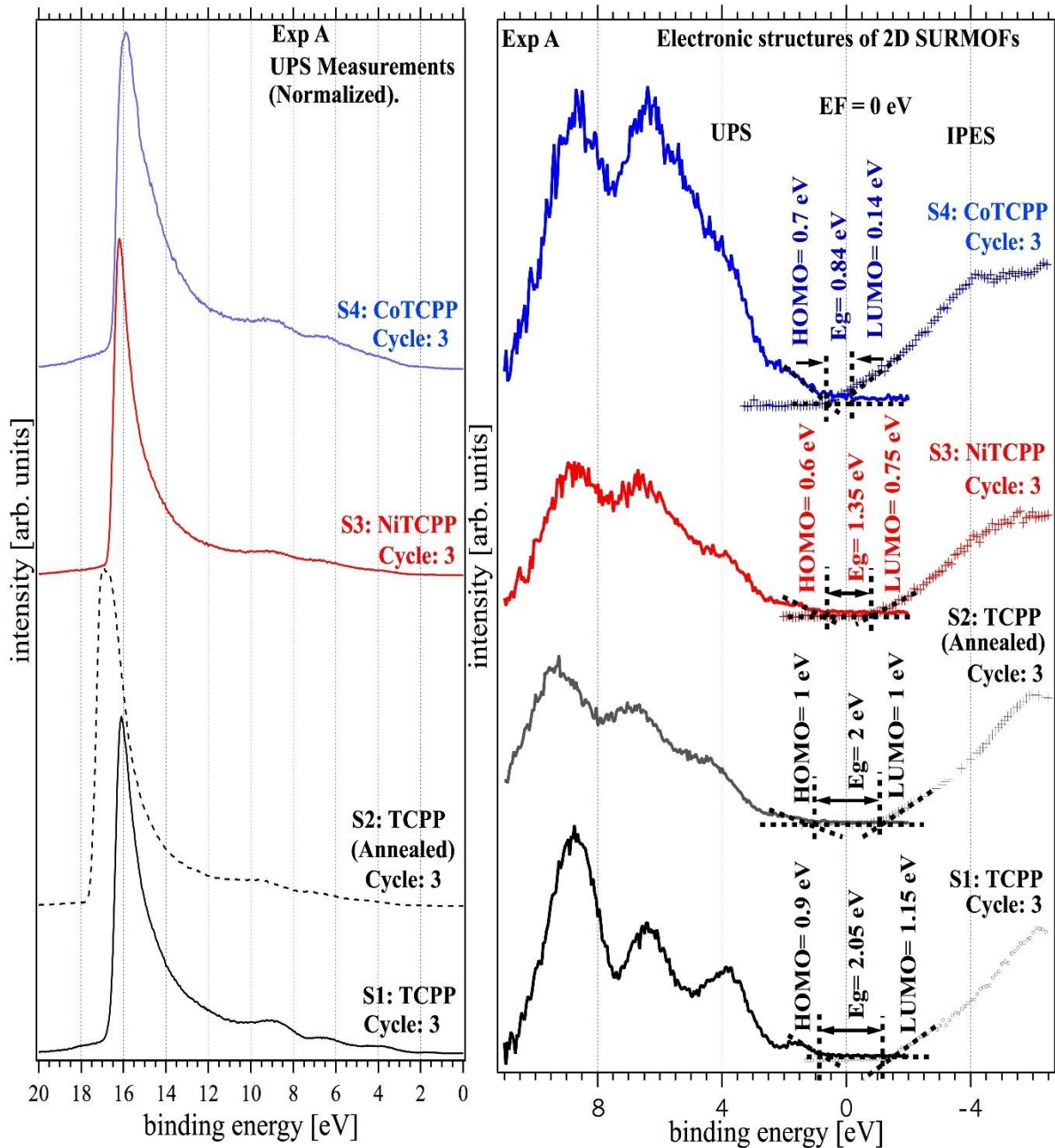


Figure 32 UP- and IPE spectra of 2D SURMOFs for four different samples grown on prefunctionalized Au surfaces. Exp A (S1-S4): $\text{Cu}(\text{OAc})_2$ paddlewheeled with TCPP, TCPP (annealed at 80°C) NiTCPP, and CoTCPP, respectively. Left panel shows full UPS normalized spectrum with corresponding secondary edges that determine the work functions which are located at high binding energies. Right panel shows HOMO and LUMO regions of 2D films after third incubation cycle located above and below Fermi edge, respectively.

5.4.2.2 Energy Band Diagram of 2D SURMOFs

The electronic structures are represented by the energy band diagram for $\text{Cu}(\text{OAc})_2$ paddlwheelled with TCPP (Exp A, S1) are shown in Figure 33a, the electronic properties of Au substrate prefunctionalized with Mpy in all experiments are identical to the work published in reference[40]. However, the work function shifts slightly to lower binding energy which is attributed to the different processing technique of the SAM growth performed in this work. The corresponding work function value of the MOF film is 4.77 eV, the hole Φ_h and electron Φ_e injection barriers revealed at 0.9 and 1.15 eV respectively, and the transfer band gap value is 2.05 eV. The interfacial dipole (eD) that affects the injection efficiency is obtained by the subtraction of the Mpy work function from that of the MOF and had a value of 0.45 eV. The energy separations are represented by both the ionization energy (E_{ion}) that has a value of 5.06 eV obtained by adding the work function of the SURMOF to the Φ_h , and the electron affinity (E_{EA}) has a value of 3.62 eV obtained by subtracting the Φ_e from the work function of the SURMOF.

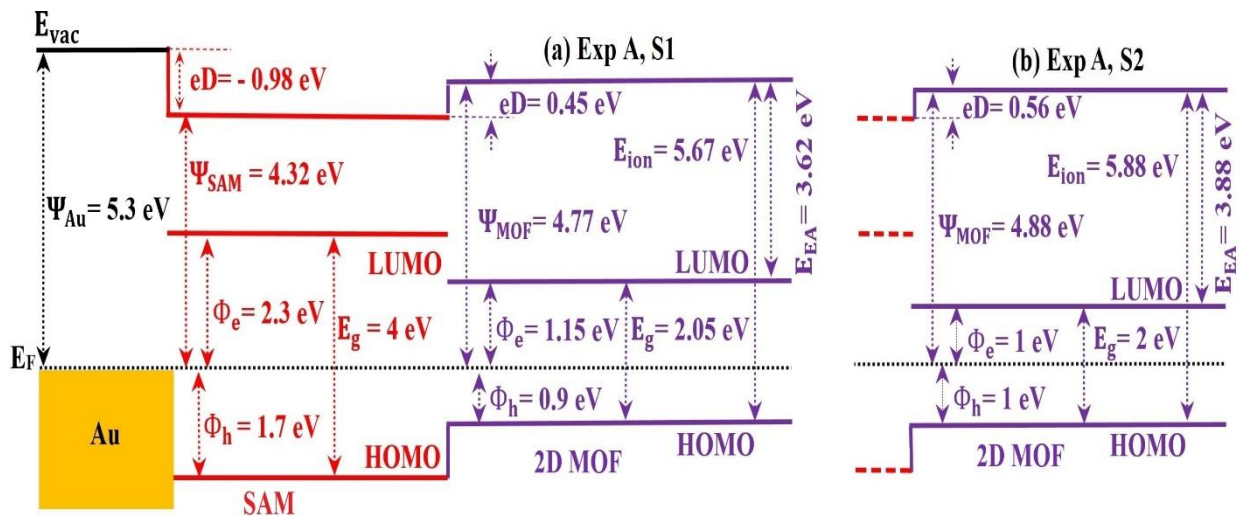


Figure 33 Electronic structures at the interface of Exp A. (a) S1: 2D MOF thin film grown (Metal ion: $\text{Cu}(\text{OAc})_2$, Organic ligand: TCPP) on Au prefunctionalized surface as determined from the UP-, IPE- and LIXP-spectra measurements. (b) S2: 2D MOF thin film annealed at 80 °C (Metal ion: $\text{Cu}(\text{OAc})_2$, Organic ligand: TCPP) which was grown on Au prefunctionalized surface as determined from the UP-, IPE- and LIXP-spectra measurements.

The electronic structures of 2D MOF film which was annealed at 80 °C (Exp A, S2) are shown in Figure 33b have considerably shifted to higher binding energies in comparison with (Exp A, S1). The corresponding work function value is 4.88 eV, the hole Φ_h and electron Φ_e injection barriers were both revealed at 1 eV respectively, and the corresponding transfer band gap is 2 eV. The interfacial dipole (eD) obtained at a value of 0.56 eV. The energy separations representing both the ionization energy (E_{ion}) and the electron affinity (E_{EA}) obtained at values of 5.88, and 3.88 eV, respectively.

The electronic structures in the energy band diagram of $Cu(OAc)_2$ paddlewheeled with NiTCPP (Exp A, S3) shown in Figure 34a have considerably shifted to lower binding energies compared to (Exp A, S1). The corresponding work function value is 4.32 eV, the hole Φ_h and electron Φ_e injection barriers revealed at 0.6 and 0.75 eV respectively, and the corresponding transfer band gap is 1.35 eV. The interfacial dipole (eD) obtained at a value of 0.27 eV. The energy separations representing both the ionization energy (E_{ion}) and the electron affinity (E_{EA}) obtained at values of 5.19, and 3.84 eV, respectively.

The energy band diagram of $Cu(OAc)_2$ paddlewheeled with CoTCPP (Exp A, S4) is shown in Figure 34(b). The corresponding work function value is 4.88 eV, the hole Φ_h and electron Φ_e injection barriers revealed at 0.7 and 0.14 eV respectively, and the corresponding transfer band gap has reached a lowest value of 0.84 eV compared with previous experiments (Exp A, S1-S3). The interfacial dipole (eD) obtained at a value of 0.56 eV. The energy separations representing both the ionization energy (E_{ion}) and the electron affinity (E_{EA}) obtained at values of 5.88, and 5.04 eV, respectively.

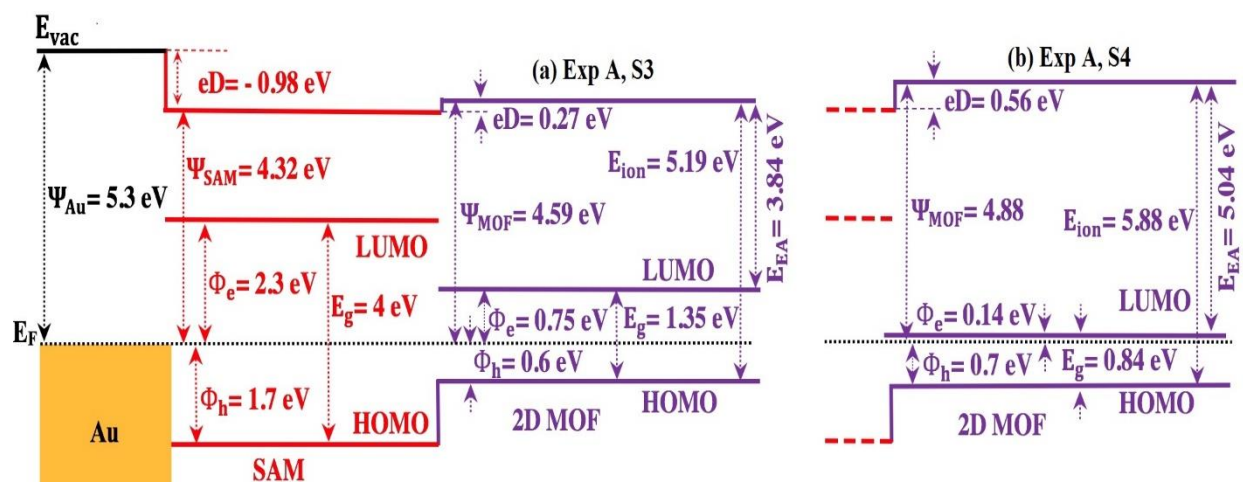


Figure 34 Electronic structures at the interface of Exp A. (a) S3: 2D MOF thin film (Metal ion: $\text{Cu}(\text{OAc})_2$, Organic ligand: NiTCPP) grown on Au prefunctionalized surface as determined from the UP-, IPE- and LIXP-spectra measurements. (b) S4: 2D MOF thin film (Metal ion: $\text{Cu}(\text{OAc})_2$, Organic ligand: CoTCPP) grown on Au prefunctionalized surface as determined from the UP-, IPE- and LIXP-spectra measurements.

5.4.2.3 Valence and Conduction Bands of 3D SURMOFs

All UPS- and IPE- spectra (normalized with background subtractions) that correspond to the three samples in Exp B (S1-S3) are shown in Figure 35.

The HOMO and LUMO values obtained that is attributed to the MOF 3D film pillared with Pz molecule (Exp B, S1) are 1.2 and 1.6 eV, respectively. The resultant band gap value amounts to 2.8 eV which is larger than that of the MOF 2D film (Exp A, S1) formed without a pillaring linker. This remarkable upward shift of HOMO and LUMO levels to higher binding energies is due to the incorporation of Pz as dopant molecule with π -electron-donating ability[118] of the nitrile group leading to a larger band gap. The normalized UPS spectra with background subtraction showing measurements after each incubation step is shown in Figure 36.

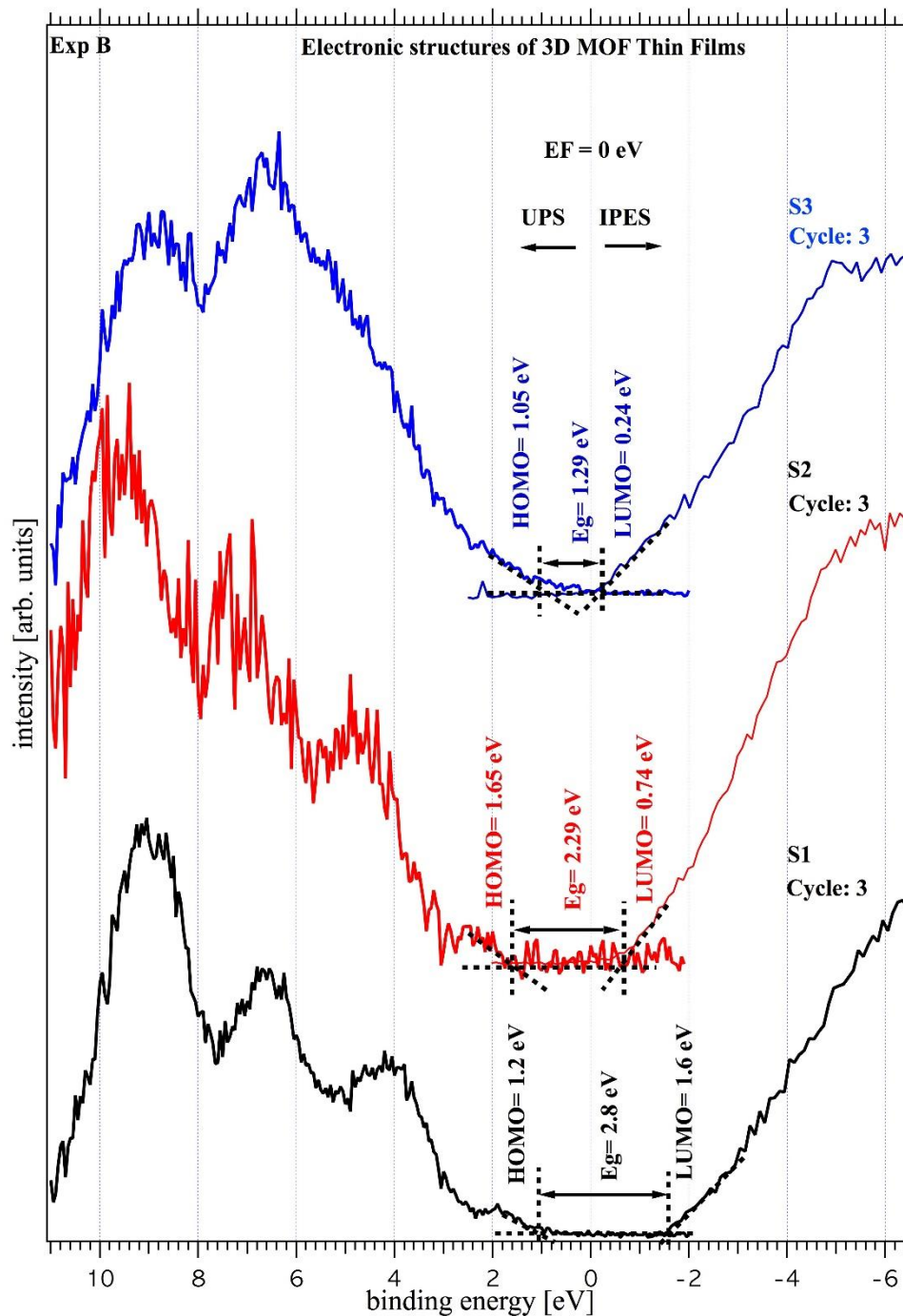


Figure 35 UP- and IPE spectra of 3D MOF films showing the HOMO and LUMO regions after third incubation cycle located above and below Fermi edge, respectively. Exp B for three different samples grown on prefunctionalized Au surfaces. Exp B, S1 (Metal ion: $\text{Cu}(\text{OAc})_2$, Organic ligand: TCPP, Pillaring Linker: Pz). Exp B, S2 (Metal ion: $\text{Cu}(\text{OAc})_2$, Organic ligand: TCPP, Pillaring Linker: Bipy). Exp B, S3 (Metal ion: $\text{Cu}(\text{OAc})_2$, Organic ligand: CoTCPP, Pillaring Linker: Bipy).

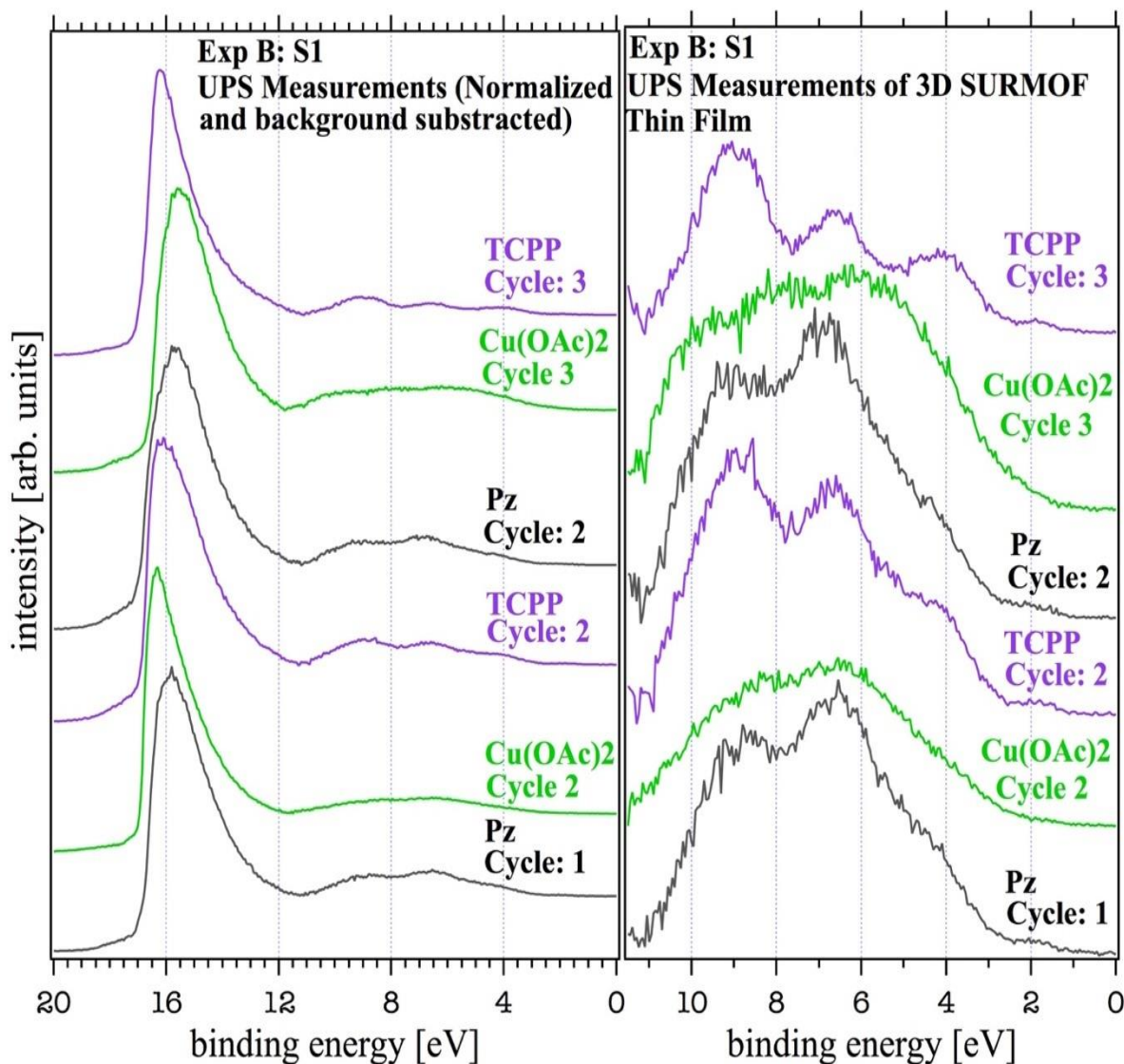


Figure 36 UP spectra of 3D SURMOF thin film of Exp B: S1. (Metal ion: $\text{Cu}(\text{OAc})_2$, Organic ligand: TCPP, Pillaring Linker: Pz). Left panel shows full UPS normalized spectrum with corresponding secondary edges that determine the work functions that are located at high binding energies. Left panel shows HOMO regions are located above Fermi edge for the step by step growth of the 3D film.

The HOMO and LUMO values obtained from MOF 3D film pillared with Bipy molecule (Exp B, S2) are positioned at 1.65 and 0.74 eV, respectively. The HOMO interestingly has shifted to higher binding energy by 0.63 eV compared to the HOMO of Exp B, S1, and places the LUMO at a lower value of 0.74 eV. The resultant band gap value is 2.29 eV. In spite of the optical band gap of Bipy amounts to 5.3 eV found in literature[119, 120] and with a HOMO positioned at 5.0

eV from UPS measurement; there was a similar straddled HOMO alignment to 1.65 eV by the effect of Bipy on phthalocyanine molecule which was reported by Palmgren et al.[121] which is in good agreement with the result observed in Exp B, S2. This clearly indicates that the addition of various pillaring linkers has a leading impact to tune the electronic properties of 3D MOF thin films. The normalized UPS spectra with background subtraction measured after step by step growth is shown in Figure 37.

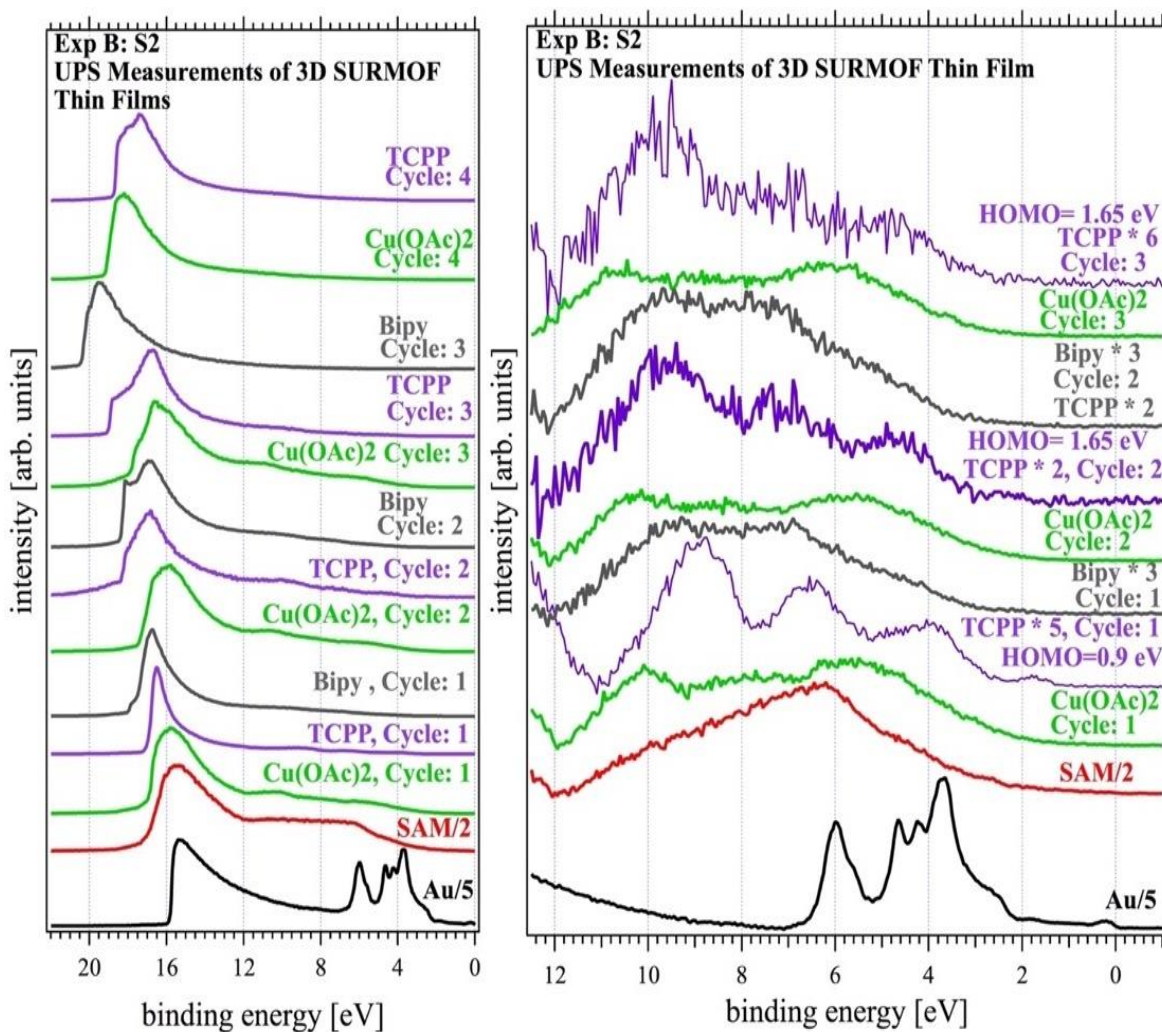


Figure 37 UP spectra of 3D SURMOF thin film of Exp B: S2. (Metal ion: $\text{Cu}(\text{OAc})_2$, Organic ligand: TCPP, Pillaring Linker: Bipy) Left panel shows full UPS normalized spectrum with corresponding secondary edges that determine the work functions that are located at high binding energies. Right panel shows HOMO regions are located above Fermi edge for the step by step growth of the 3D film.

The resultant UP-IPE spectra of metalated porphyrin ligand CoTCPP pillared with Bipy molecule (Exp B, S3) after the third incubation cycle is shown in Figure 35. The HOMO has shifted to higher binding energy value of 1.05 eV and the LUMO to lower binding energy value of 0.24 eV, the remarkable decrease in LUMO energy is probably attributed to the presence of the axially bonded linkers. This is completely in agreement with the LUMO of about 0.2 eV from Biby as reported in literature.[121] The corresponding transfer band gap value is 1.29 eV which is larger than that of the 2D MOF thin film formed with CoTCPP (Exp A, S3). Thus, the incorporation of Bipy molecule with CoTCPP enabled to decrease the bandgap value to 1.29 eV. In contrast, according to the UV-vis measurement, the optical band gap value of CoTCPP ligand is larger and varies between 2.4-3.1 eV in literature[116, 117] due to the absence of both the SBUs and the pillaring linkers. The normalized UPS spectra is shown in Figure 38.

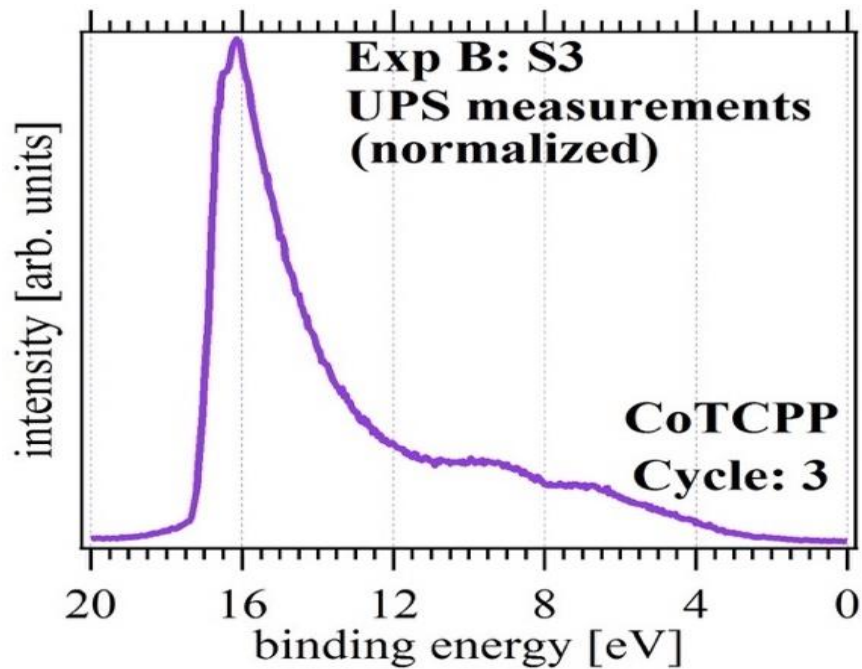


Figure 38 UP spectra of 3D MOF thin film in Exp B: S3. (Metal ion: $\text{Cu}(\text{OAc})_2$, Organic ligand: CoTCPP, Pillaring Linker: Bipy) showing full UPS normalized spectrum with corresponding secondary edge that determines the work functions located at high binding energies.

5.4.2.4 Energy Band Diagram of 3D SURMOFs

The electronic structures are denoted in the energy band diagram for $\text{Cu}(\text{OAc})_2$, paddlewheeled with TCPP (Exp B, S1) with the amalgamation of pillaring linker (Pz) is shown in Figure 39. The corresponding work function value is 4.77 eV, the hole Φ_h and electron Φ_e injection barriers revealed at 1.2 and 1.6 eV respectively, and the corresponding transfer band gap is 2.8 eV. The interfacial dipole (eD) that affects the injection efficiency is obtained by the subtraction of the Mpy work function from that of the MOF and has a value of 0.45 eV. The energy separations are represented by both the ionization energy (E_{ion}) with a value of 5.97 eV obtained by adding the work function of the SURMOF to the Φ_h , and the electron affinity (E_{EA}) value is 3.17 eV obtained by subtracting the Φ_e from the work function of the MOF film.

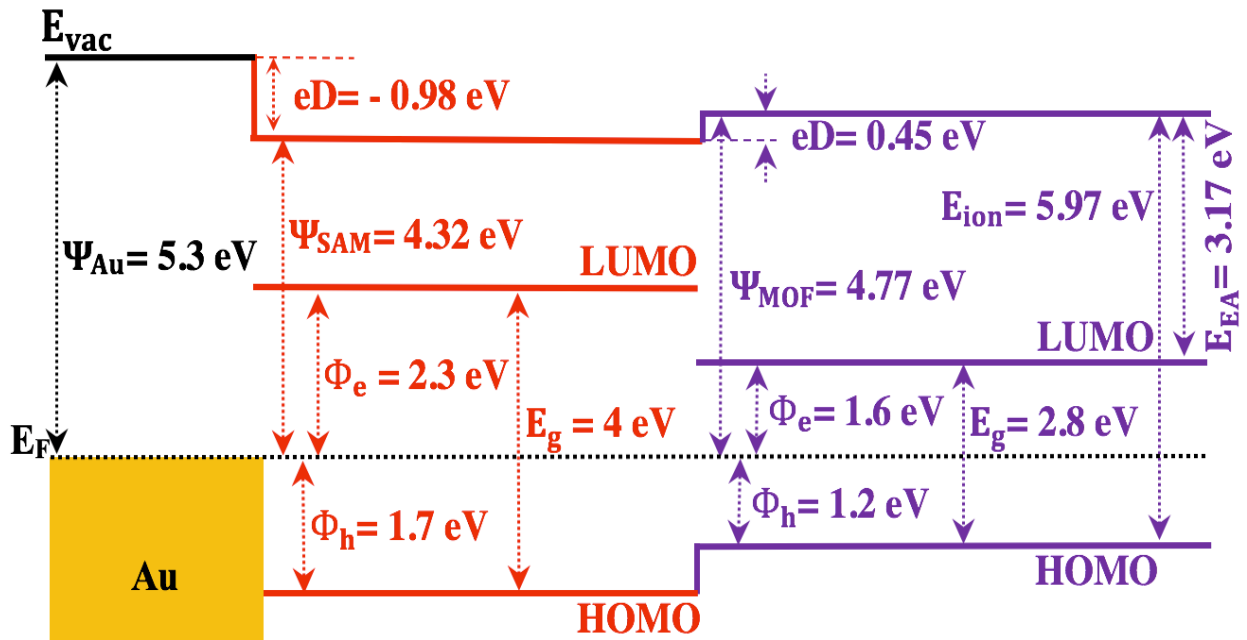


Figure 39 Energy band diagram of 3D MOF thin film of Exp B: S1, (Metal ion: $\text{Cu}(\text{OAc})_2$, Organic ligand: TCPP, Pillaring linker: Pz) grown on Au prefunctionalized surface as determined from the UP-, IPE- and LIXP-spectra measurements.

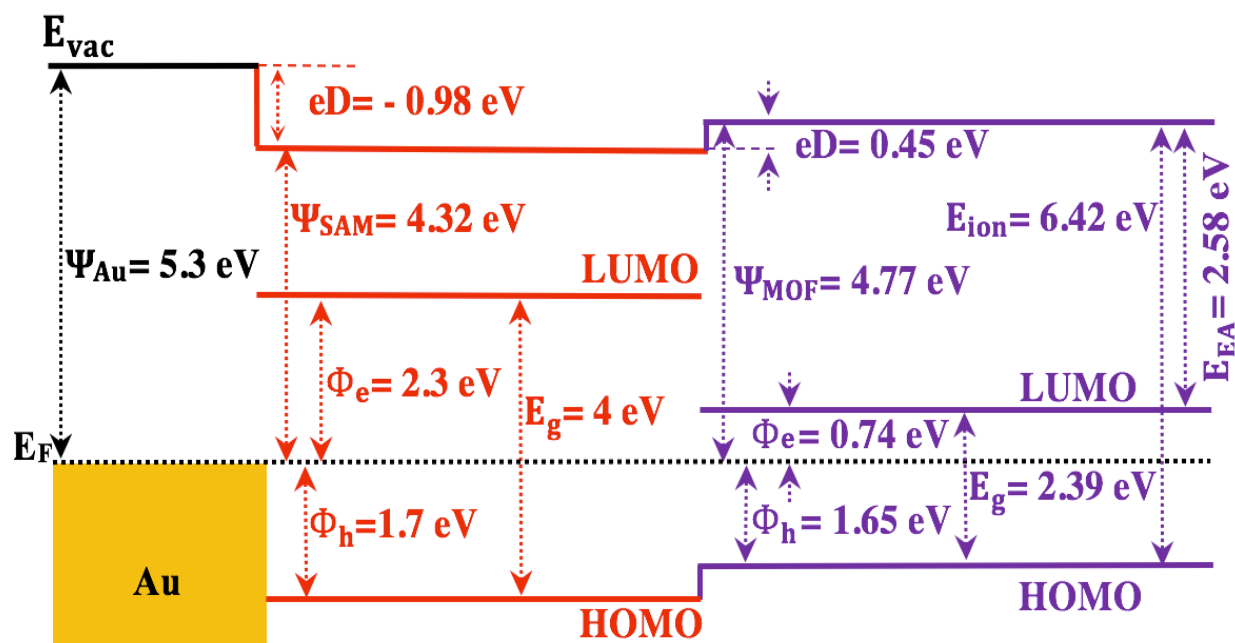


Figure 40 Energy band diagram of 3D MOF thin film of Exp B: S2, (Metal ion: $\text{Cu}(\text{OAc})_2$, Organic ligand: TCPP, Pillaring linker: Bipy) grown on Au prefunctionalized surface as determined from the UP-, IPE- and LIXP-spectra measurements.

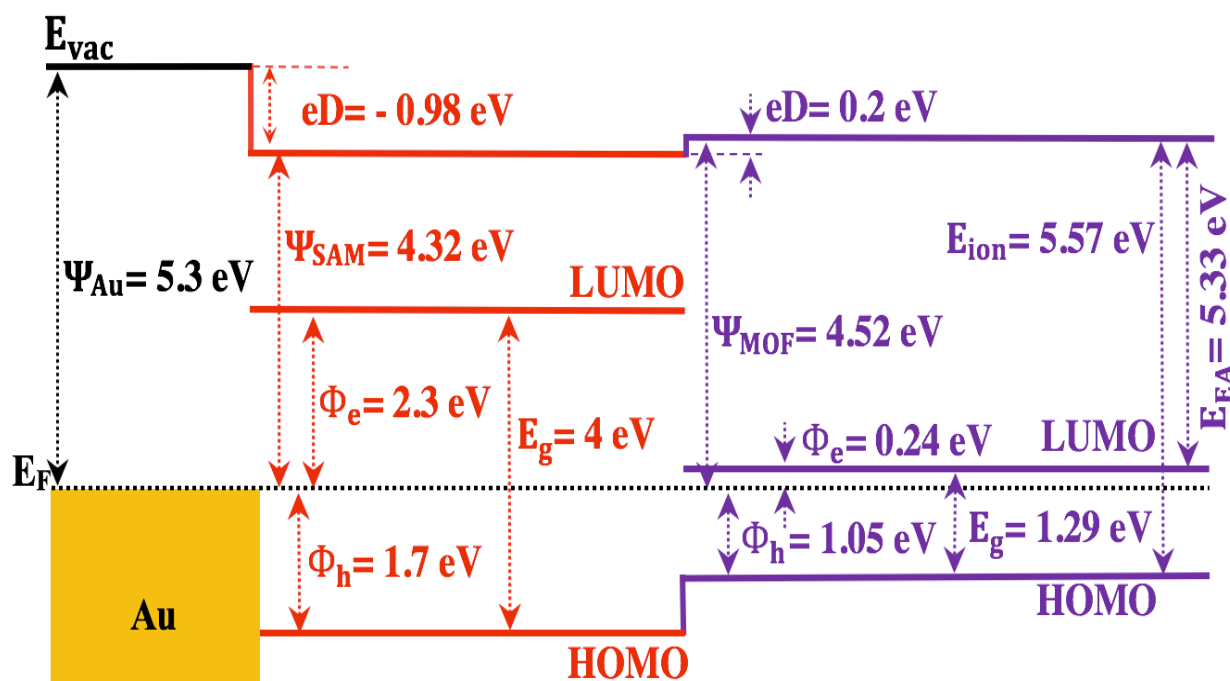


Figure 41 Energy band diagram of 3D MOF thin film of Exp B: S3, (Metal ion: $\text{Cu}(\text{OAc})_2$, Organic ligand: CoTCPP, Pillaring linker: Bipy) grown on Au prefunctionalized surface as determined from the UP-, IPE- and LIXP-spectra measurements.

The electronic structures of $\text{Cu}(\text{OAc})_2$ paddlewheeled with TCPP (Exp B, S2) which pillared with Bipy molecule is shown in Figure 40. The obtained work function value is 4.77 eV, the hole Φ_h and electron Φ_e injection barriers revealed at 1.65 and 0.64 eV, respectively. The interfacial dipole (eD) had a value of 0.45 eV. The ionization energy (E_{ion}) obtained at a value of 6.42 eV.

The electronic structures observed in the energy band diagram of $\text{Cu}(\text{OAc})_2$ paddlewheeled with CoTCPP (Exp B, S3) which pillared with Bipy linker is shown in Figure 41. The corresponding work function value of the MOF is 4.52 eV, the hole Φ_h and electron Φ_e injection barriers revealed at 1.05 and 0.24 eV respectively, and the corresponding transfer band gap is 1.29 eV. The interfacial dipole (eD) obtained at a value of 0.2 eV. The energy separations representing both the ionization energy (E_{ion}) and the electron affinity (E_{EA}) obtained at values of 5.57, and 5.33 eV, respectively.

5.4.3 Interfacial and Surface Chemistry Characterizations

XPS was involved to study the interfacial growth mechanism and surface chemistry of 2D and 3D SURMOFs after sequential step-by-step incubations.

5.4.3.1 XPS of 2D SURMOFs

The evolution of the Au 4f, C 1s, and Cu 2p core level emission lines through Exp A, S1 is shown in Figure 42. The black spectrum corresponds to the SURMOF with TCPP experiment where the growth occurred at RT. The gray (dashed) spectrum represents S2 with the same organic ligand which was annealed at 80 °C. Metalated porphyrin ligands NiTCPP and CoTCPP are shown in red and blue, respectively. The green spectrum reveals the emission of SAM features.

The intensities of Au 4f spectra in Exp A were decreased significantly post each incubation cycle (C) which indicate the SURMOF growth with increasing thicknesses. These intensities for

SURMOF grown at RT are quite similar after the third incubation cycle, and have substantially lowest attenuation post six incubation cycle indicating complete surface coverage. Interestingly, the annealed sample (S2) shows more significant growth after the third incubation cycle than other samples due the lowest reduction of its Au intensity. The difference in intensities of porphyrin materials in different samples correlates to the thickness and surface coverage of the films which is related to the dipping process (*i.e.*, the velocity of withdrawing the substrate from the solution), where a faster withdrawing speed, produces a thicker film due to pulling more liquids[122] into forming wet-dry solid-state MOF films. In contrast, robot dipping[123] or ALD[124] processes can produce more consistent layer growth and thicknesses compared with the layer by layer process performed in this work.

The aromatic hydrocarbon related C 1s emission features of both SAM and TCPP multilayers produce strong peaks at about 285.6 and 285 eV, respectively. The element in the C 1s spectra has a smaller emission at about 288.9 eV, which is related to C-O bonds, which are found in the COOH groups of Cu(OAc)₂ when interacted with TCPP molecule[109],[79]. The shift to higher binding energy in S1 post six incubation cycle by 0.9 eV of the organic ligand is related to charging artifacts during XPS measurement as the film grows in thickness.

The Cu 2p emissions from the Cu(OAc)₂ show observations of Cu(II) states positioned at binding energy values of 932.7 eV and 935.4 eV. However, once the organic ligands were added onto the surface, the Cu 2p_{3/2} emissions show distinguished doublet features after the third incubation cycle positioned at 933 and 935 eV respectively, and have substantially shifted to higher binding energies and revealed two additional shake-up satellite peaks located in Cu 2p_{3/2} peak region which are positioned at 942 eV and 946 eV. These chemical shifts with the attenuated intensities post incubations the samples in the porphyrin solutions, and the peak shapes of the

oxidation states Cu (II) concur that Cu paddlewheels (SBUs) were self-assembled in situ by the presence of the COOH of porphyrin ligands.

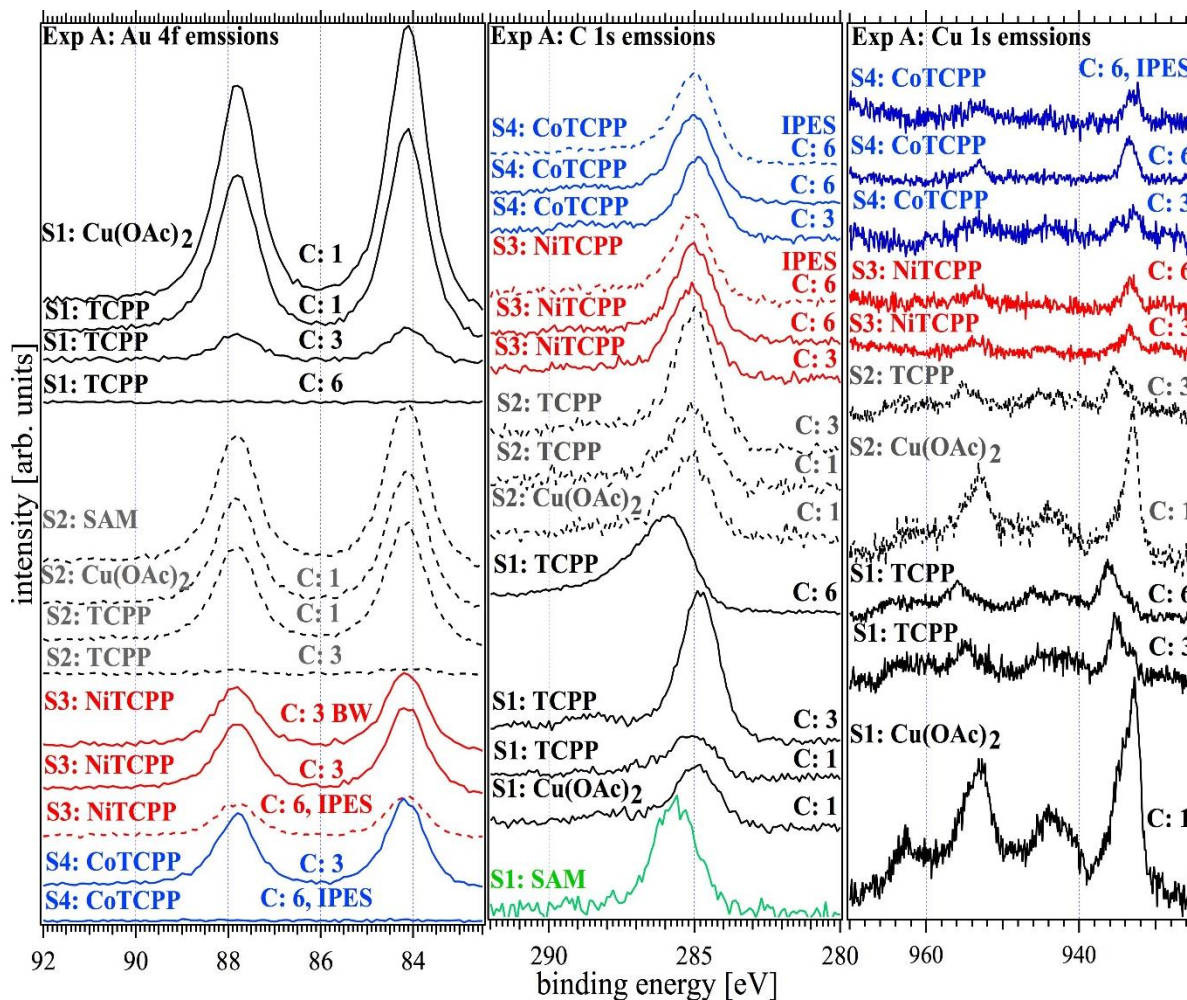


Figure 42 Au 4f, C 1s, and Cu 2p core level XPS spectra of 2D SURMOF measured after incubation the prefunctionalized Au substrate in the $\text{Cu}(\text{OAc})_2$ solution, then in the corresponding organic ligand solution for three to six cycles sequentially. Black, gray, red, and blue spectra represent MOF experiments with the following organic ligands: TCPP, TCPP annealed at 80°C , NiTCPP, and CoTCPP respectively.

The S 2p emission feature of the SAM has a binding energy of about 162.7 eV consistent with S in the thiolate form bonded to an Au surface[40, 125] is shown in the Figure 43. The N 1s emission features are shown in Figure 44 (left and middle panel). The initial N 1s core level of the SAM reveals a broad peak at about 400.6 eV, which confirms the deposition of Mpy on the Au

surface. The N 1s spectra measured during the growth of the 2D MOF films from Exp A (S1-S4) exhibit distinctly emission features that are attributed to a molecule containing iminic (-N=) and pyrolic (-NH-) nitrogen species. These are also indicators that an interaction between Cu (II) states and corresponding porphyrin molecules occurred at the surface. These emission lines are located at 398.6 eV and 400 eV, respectively; which are in a close agreement with other experiments found in the literature[84, 126, 127],[40, 85, 108].

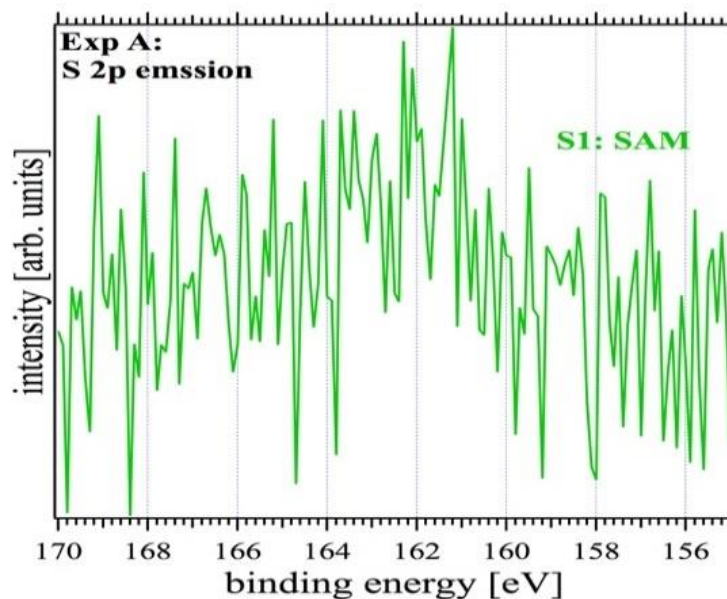


Figure 43 S 2p core level XPS spectrum measured after incubation the Au substrates in 4-mercaptopyridine solution.

The analysis of the O 1s core level emission sequence as shown in Figure 44 (right panel) is consistent with the Cu 2p, C 1s, and N 1s emission series. The O 1s emission feature present after the Cu(OAc)₂ growth step is located at 531.4 eV. This emission is attenuated and shifted to a higher binding energy value of 532 eV after the third incubation cycle in TCPP and this attributed to the COOH groups present in the MOF film observed in Exp A, S1, however charging artifacts seen post six incubation cycle as the film gets thicker. The O 1s core emissions in S2, S3, and S4 revealed with shifts to higher binding energies positioned at 532.4, 533, and 532.2 eV respectively,

which indicate interactions between the SBUs and the corresponding organic ligands took a higher binding energy value of 532 eV after the third incubation cycle in TCPP and this attributed to the COOH groups present in the MOF film observed in Exp A, S1, however charging artifacts seen post six incubation cycle as the film gets thicker. The O 1s core emissions in S2, S3, and S4 revealed with shifts to higher binding energies positioned at 532.4, 533, and 532.2 eV respectively, which indicate interactions between the SBUs and the corresponding organic ligands took place.

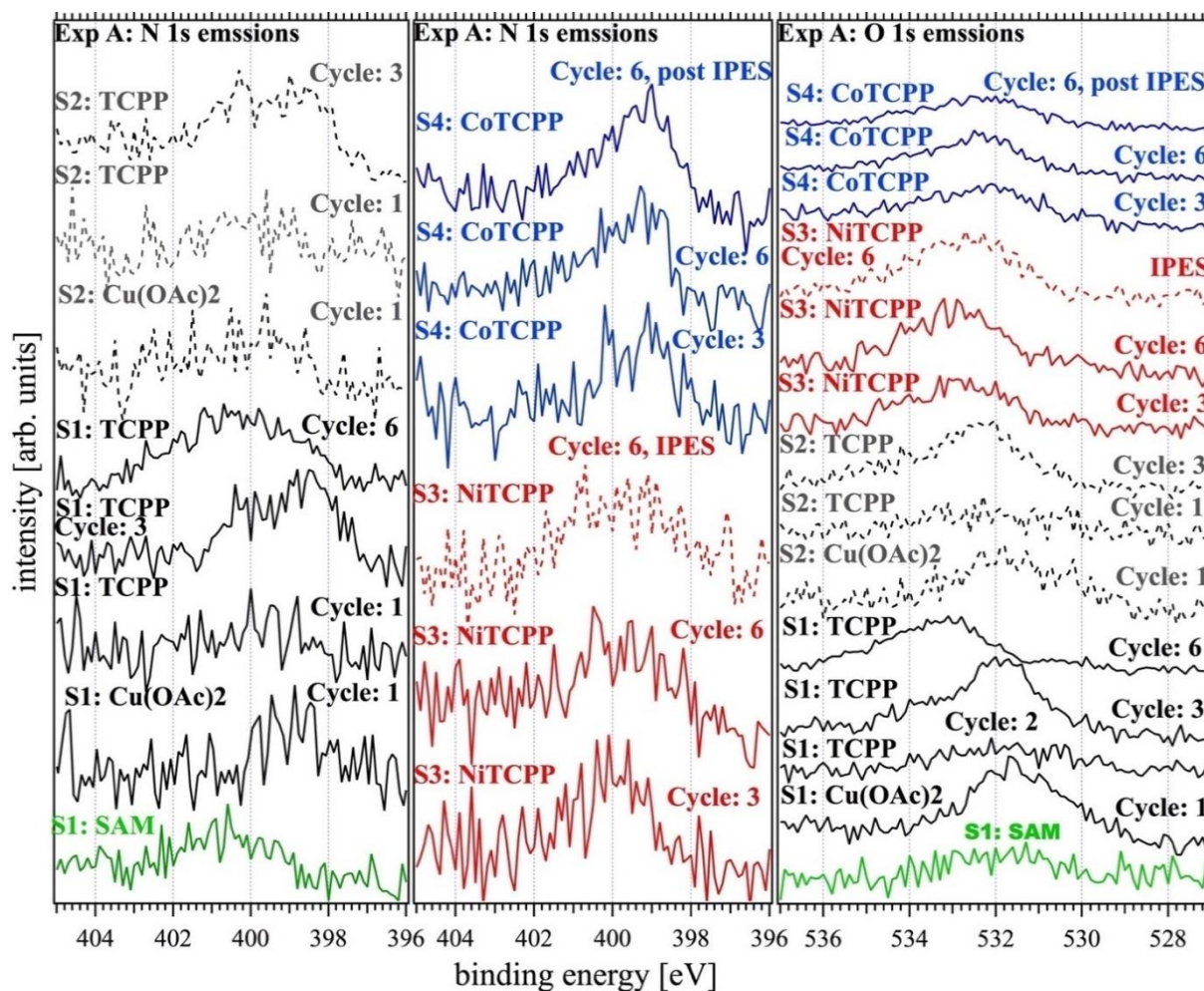


Figure 44 N 1s, and O 1s core level XPS spectra of 2D SURMOF thin films measured after incubation the prefunctionalized Au substrate in the $\text{Cu}(\text{OAc})_2$ solution, then in the corresponding organic ligand solutions for three to six cycles sequentially. Black, gray, red, and blue spectra represent MOF experiments with the following ligands: TCPP, TCPP annealed at 80°C , NiTCPP, and CoTCPP respectively.

5.4.3.2 XPS of 3D SURMOFs

The evolution of the Au 4f, C 1s, and Cu 2p core level emission lines throughout Exp B, S1 is shown in Figure 45. The black spectrum from the top reveals the Au 4f emission features after first incubation cycle in Pz molecule. The intensities of Au 4f spectra in Exp B were decreased significantly post each incubation cycle which indicated the MOF growth with increasing thicknesses. The Au 4f intensity shows lowermost attenuation post third incubation cycle.

The Core level emission lines Exp B, S2 are shown in Figure 8a. The Au 4f emissions show good surface coverage post second incubation cycle. The Au 4f core level emissions of metalated porphyrin CoTCPP with Bipy (Exp B, S3) after third incubation cycle is shown in Figure 9a.

The C 1s emission of Exp B, S1 shows aromatic hydrocarbon features in Figure 45 related to TCPP multilayers with Pz which is positioned at a binding energy value of 285 eV. The distinguishing element in the C 1s spectra has a smaller emission at about 288.6 eV, which is attributed to COOH groups of $\text{Cu}(\text{OAc})_2$ when bound to TCPP molecules in agreement with literature.[79, 109] These emissions have shifted to higher binding energies in (Exp B, S2) as shown in Figure 47 by about 0.5 eV after the third incubation cycle due to the incorporation of Bipy molecule which probably related to the formations of 3D multilayered structure.

The Cu 2p emissions after deposition of TCPP molecules (purple spectra) shown in Figure 45 (Exp B, S1) reveal the Cu(II) states have shifted to higher binding energy values of 933.1 and 935.2 eV. The presence of strong satellite shake-up peaks represents the Cu(II) states in $\text{Cu}(\text{OAc})_2$ form, and the reduction of their intensities after the deposition of TCPP and Pz molecules indicate interactions with $\text{Cu}(\text{OAc})_2$ took place. The Cu 2p core level emissions after deposition of TCPP and Bipy in Figure 8 (Exp B, S2) show expected Cu (II) states positioned at 933 and 935.5 eV and have shifted to higher binding energy value of 1.1 eV after the second incubation cycle. The Cu

2p core level emissions of CoTCPP of (Exp B, S3) in Figure 49 are identical to the emissions observed from the MOF growth reported in Figure 47.

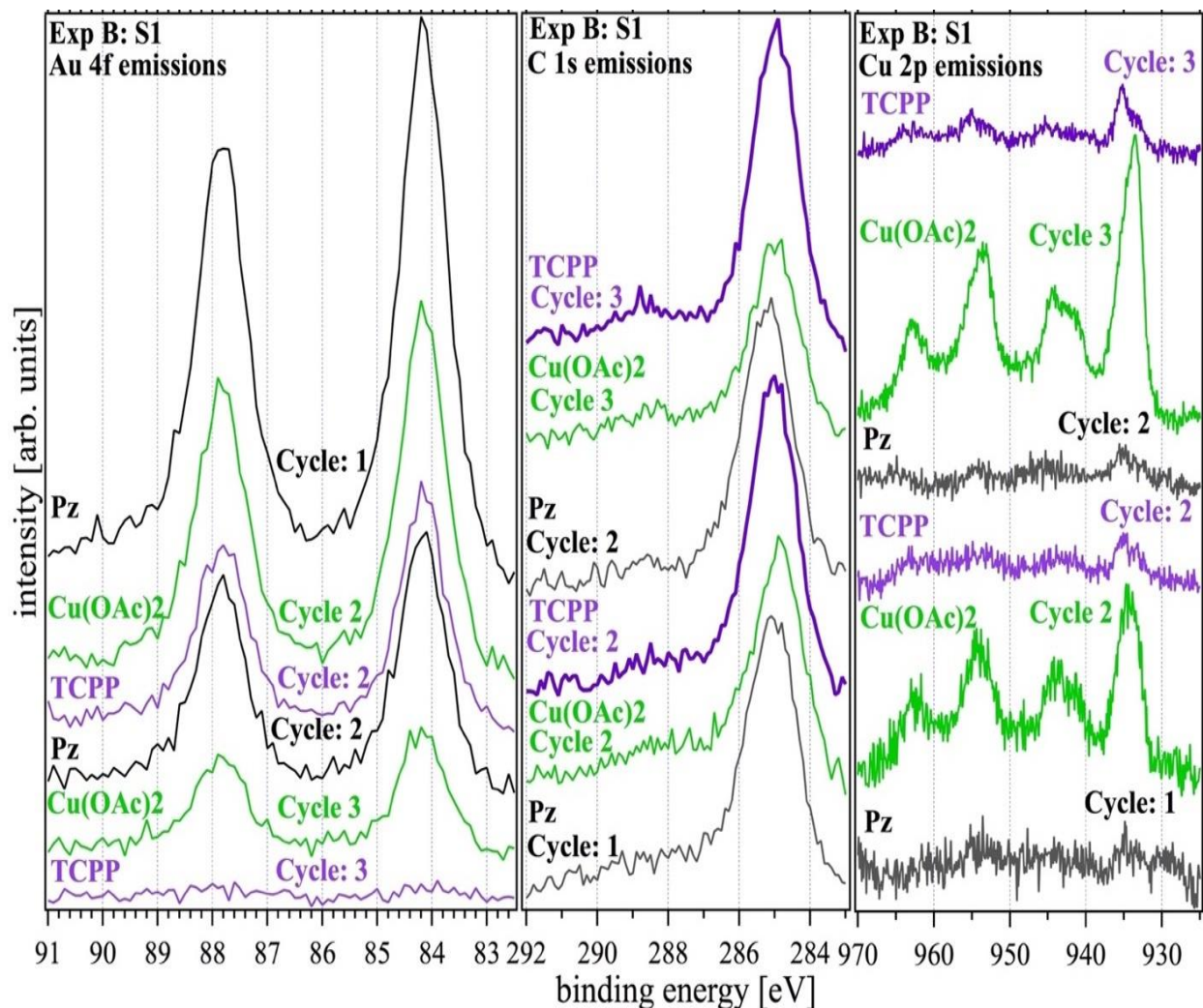


Figure 45 Au 4f, C 1s, and Cu 2p core level XPS spectra of 3D SURMOF thin film measured after incubation the prefunctionalized Au substrate in the $\text{Cu}(\text{OAc})_2$ solution, then in the corresponding organic ligand solution (TCPP) with the incorporation of pillaring linker solution (Pz) for three cycles sequentially.

The N 1s core level emissions measured after third deposition cycle of TCPP in Figure 46 (Exp B, S1) show emissions related to iminic or pyridinic features, and pyrrolic nitrogen species positioned at 398.4, and 400.2 eV respectively, the Cu-N species observed after the deposition of Pz molecule are positioned at 399.8 eV concurs with the metal-N interactions, these are close with

values reported from other experiments.[40, 85, 108, 126-132] These emissions are almost consistent with Exp B, S2 as shown in Figure 48, where pyridinic, pyrrolic, and Cu-N species are positioned at 398.6, 400.4, and 399.4 eV respectively. They exhibit a shift to higher binding energy value of 1 eV after the fourth incubation cycle as the MOF grows in thickness. The N 1s peak from Exp B, S3 in Figure 50 is positioned at lowest binding energy value of 398.9 eV corresponds to the iminic or pyridinic groups, and the Co-N species which are bonded to metal center of TCPP revealed binding energy value at 399.5 eV. The highest binding energy value of the peak positioned at 400.6 eV is attributed to the pyrrolic species from CoTCCP molecule.

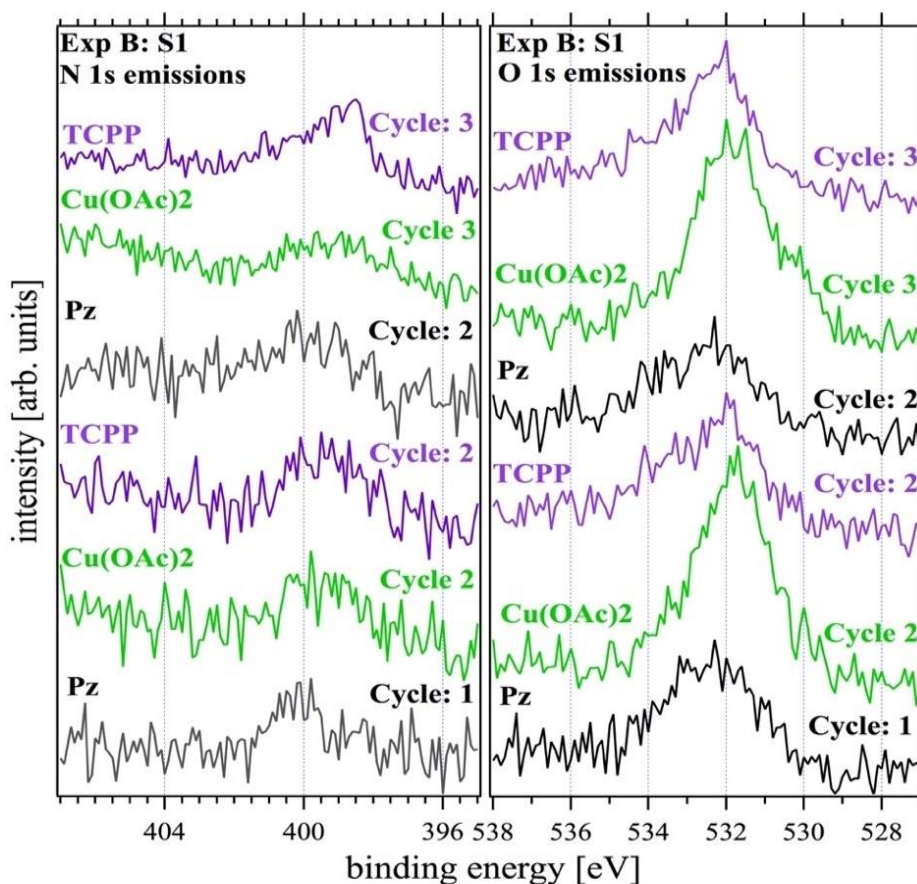


Figure 46 N 1s, and O 1s core level XPS spectra of 3D SURMOF measured after incubation the prefunctionalized Au substrate in the $\text{Cu}(\text{OAc})_2$ solution, then in the corresponding organic ligand solution (TCPP) with the incorporation of bridging ligand solution (Pz) for three cycles sequentially.

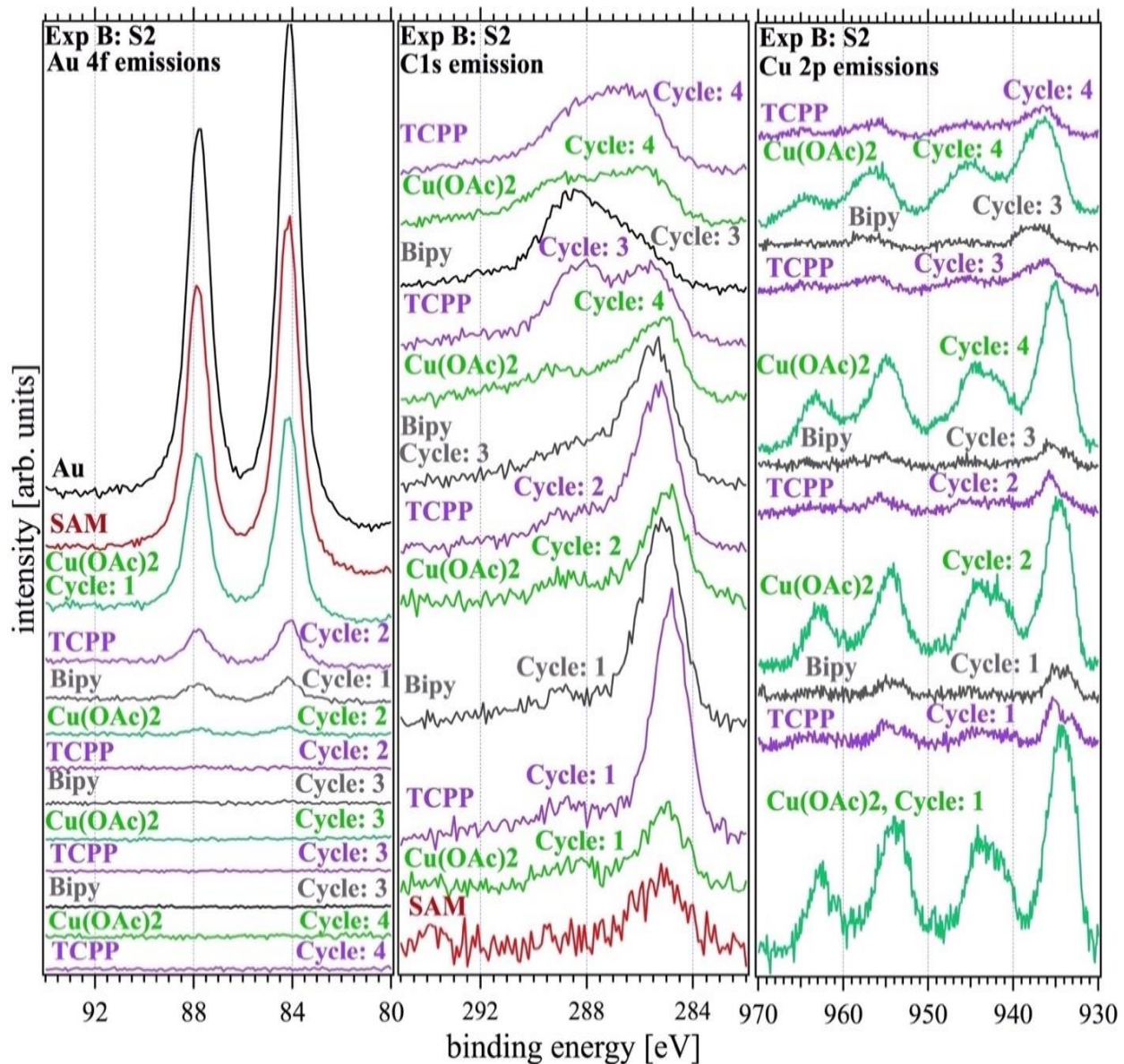


Figure 47 Au 4f, C 1s, and Cu 2p core level XPS spectra of 3D SURMOF thin film measured after incubation the prefunctionalized Au substrate in the $\text{Cu}(\text{OAc})_2$ solution, then in the corresponding organic ligand solution (TCPP) with the incorporation of pillaring linker solution (Bipy) for four cycles sequentially.

The analysis of the O 1s core level emissions sequence prior to the deposition of the pillaring linkers is consistent in comparison with the 2D MOF experiments (Exp A, S1-S4). The O 1s core level emission feature of Exp B, S1 in Figure 46 after the second deposition cycle of $\text{Cu}(\text{OAc})_2$ is positioned at 531.7 eV (green spectrum), and this has shifted to higher binding energy

value of 532 eV after the deposition of TCPP molecules (purple spectrum). The O 1s emission features after the first deposition of $\text{Cu}(\text{OAc})_2$ in Exp B, S2 located at 531.9 eV, and this peak has shifted to higher binding energy value of 532.3 eV when TCPP molecule was incorporated, larger shifts to higher binding energies observed after the third deposition cycle. The O 1s core level emission retained its binding energy value of 532 eV for CoTCPP in Exp B, S3 as shown in Figure 50.

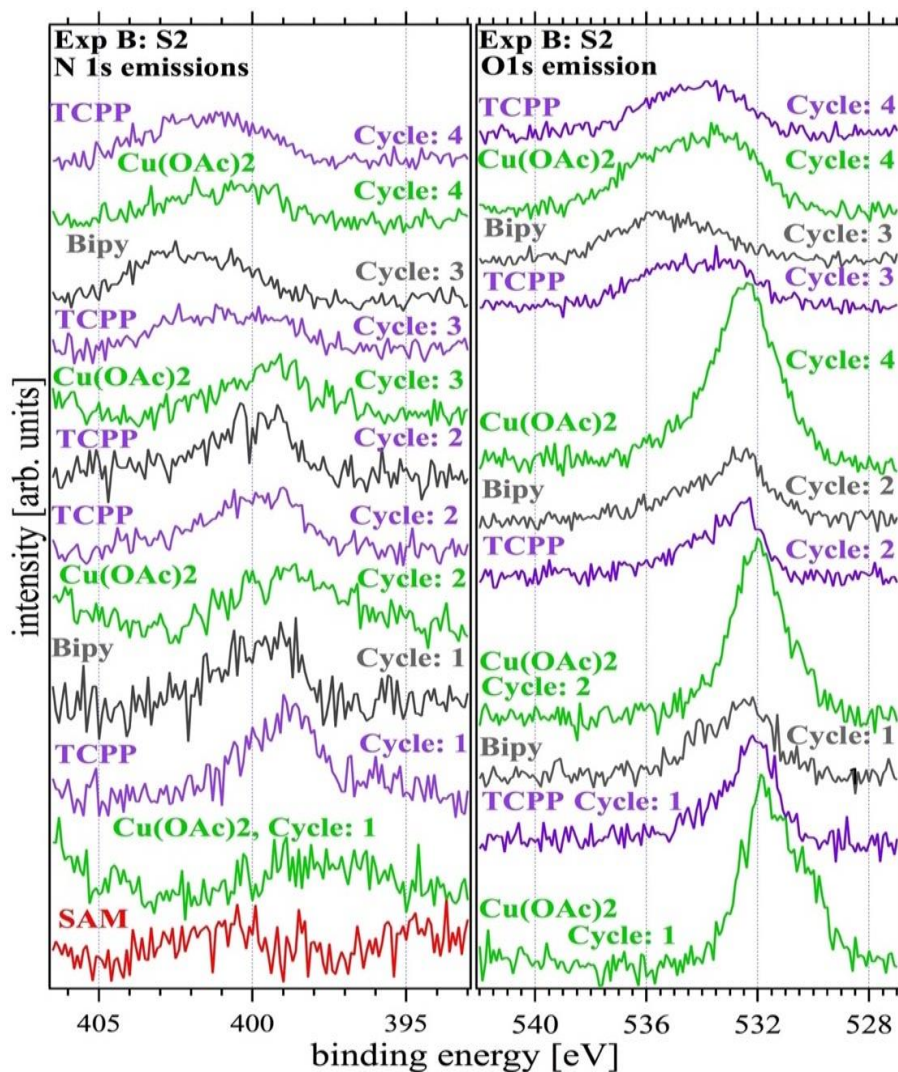


Figure 48 N 1s, and O 1s core level XPS spectra of 3D SURMOF thin film measured after incubation the prefunctionalized Au substrate in the $\text{Cu}(\text{OAc})_2$ solution, then in the corresponding organic ligand solution (TCPP) with the incorporation of pillaring linker (Bipy) for three cycles sequentially.

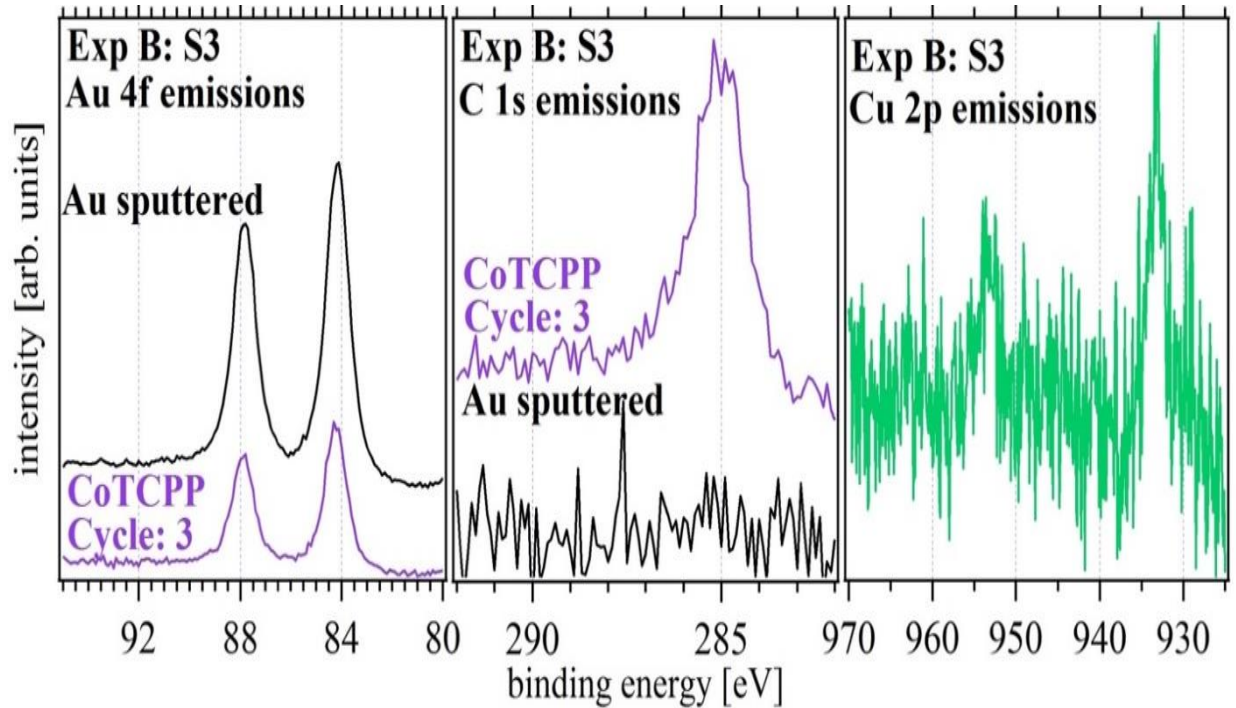


Figure 49 Au 4f, C 1s, and Cu 2p core level XPS spectra of 3D SURMOF measured after incubation the prefunctionalized Au substrate in the $\text{Cu}(\text{OAc})_2$ solution, then in the corresponding organic ligand solution (CoTCPP) with the incorporation of bridging ligand solution (Bipy) for three cycles sequentially.

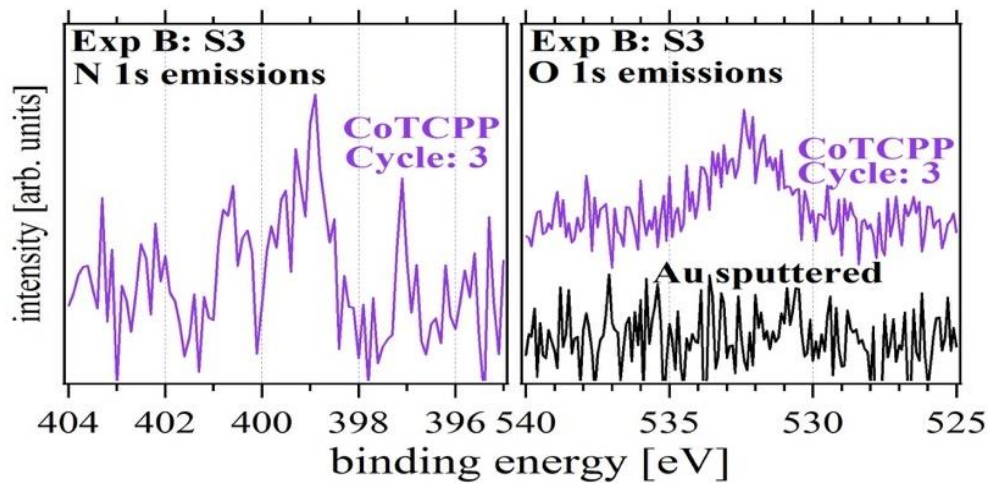


Figure 50 N 1s, and O 1s core level XPS spectra of 3D SURMOF thin film measured after incubation the prefunctionalized Au substrate in the $\text{Cu}(\text{OAc})_2$ solution, then in the corresponding organic ligand solution (CoTCPP) with the incorporation of bridging ligand solution (Bipy) for three cycles sequentially.

5.4.4 Crystal Structure Characterization

5.4.4.1 Grazing-Incidence X-ray Scattering of 2D MOFs

In Exp A, three additional cycles were deposited on S4 which was selected as a candidate for Grazing-incidence X-ray Scattering (GIXS) measurements to reveal the formation of 2D MOF thin films, and that can be inferred from the well-resolved in-plane diffraction peaks as shown in Figure 51 which assigned with the corresponding miller indices as (hk0) and these commensurate well with those found in the literature[72, 133]. The dimensions of the tetragonal cell, obtained from Figure S52 and Figure 53, are $a = b = 16.27 \text{ \AA}$, and $c = 9.1 \text{ \AA}$ respectively, and the space group is P4/mmm (No. 123). The unit cell parameters were loaded into GIXSUI software[134] to generate the simulated patterns (dashed lines) that matched well with the experimental in-plane and out-of plane diffraction peaks.

The spacing between lamella value is 4.55 \AA obtained from out-of-plane measurement shown in Figure 52 depicts the MOF growth is in planner direction with respect to the substrate which is consistent with the data found in literature[72, 133].

The qz linecut fitting finds the AB crystal along the c-direction is about $54.4 / 4.55 \cong 12$ monolayers or 6 unit cell size (if D_{\max} was chosen) as manifested in Figure 52(d). The projection of expected crystal structure of 2D MOF in Figure 53 was generated based on the crystal data published[72] and agrees well with unit cell parameters used in GIXSUI.

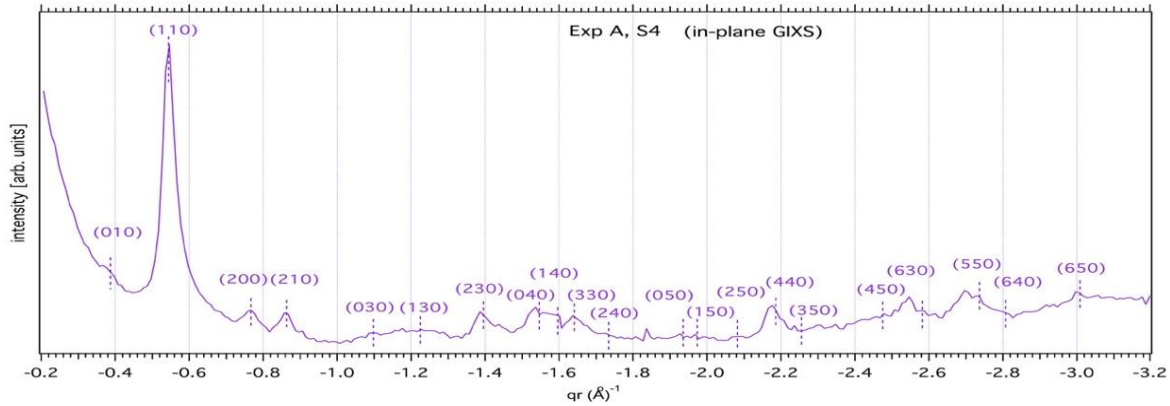


Figure 51 Grazing-incidence in-plane X-ray scattering of 2D MOF thin film of Exp A, S4. (wavelength= 1.1354 Å, incidence angle, $\alpha = 0.35^\circ$) showing the miller indices of the Bragg peaks in order with scattering angle that matched the simulated diffraction patterns generated by GIXSUI (dashed lines).

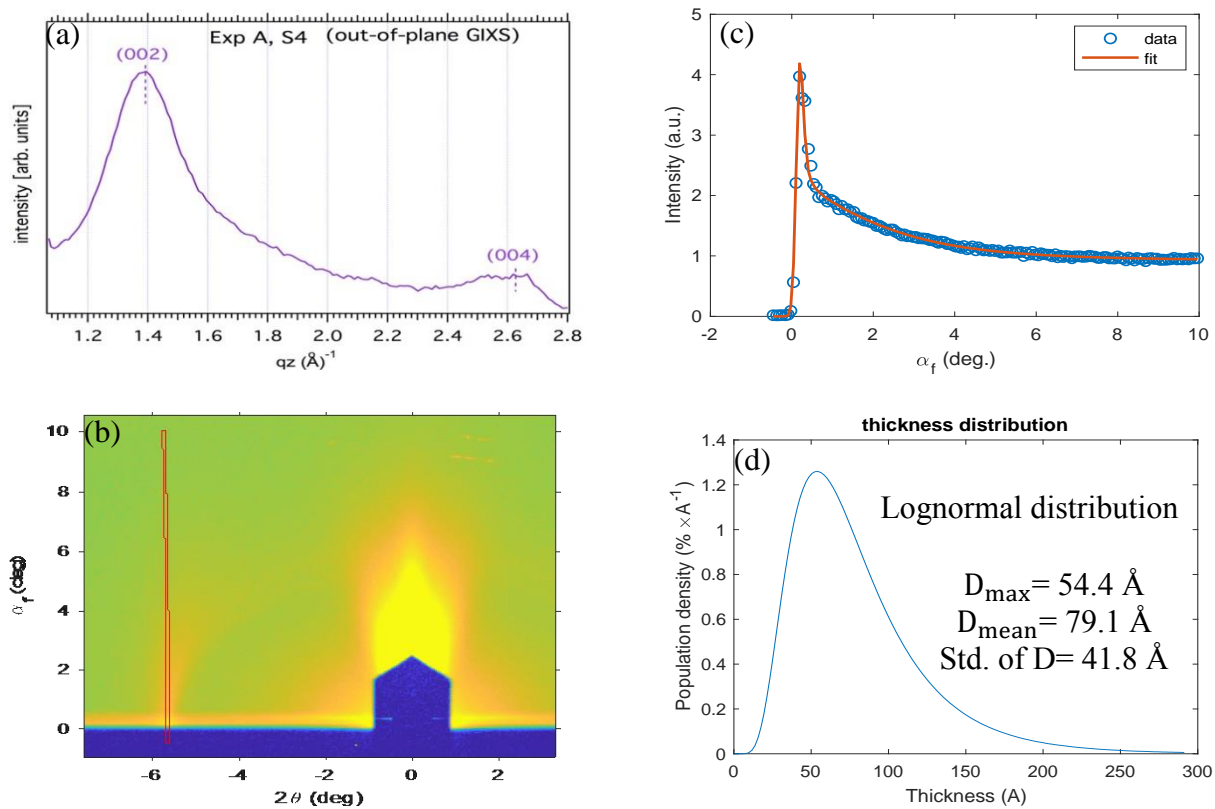


Figure 52 (a) Grazing-incidence out-of-plane X-ray scattering of 2D MOF film of Exp A, S4. (wavelength= 1.1354 Å, incidence angle, $\alpha = 0.35^\circ$). Miller indices of the Bragg peaks are (002), and (004) in order with scattering angle. (b), (c), and (d) thickness distribution showing the qz linecut fitting which finds the AB crystal along c -direction is about $54.4/4.8 = 12$ monolayers or 6 unit cell size (if D_{max} was chosen).

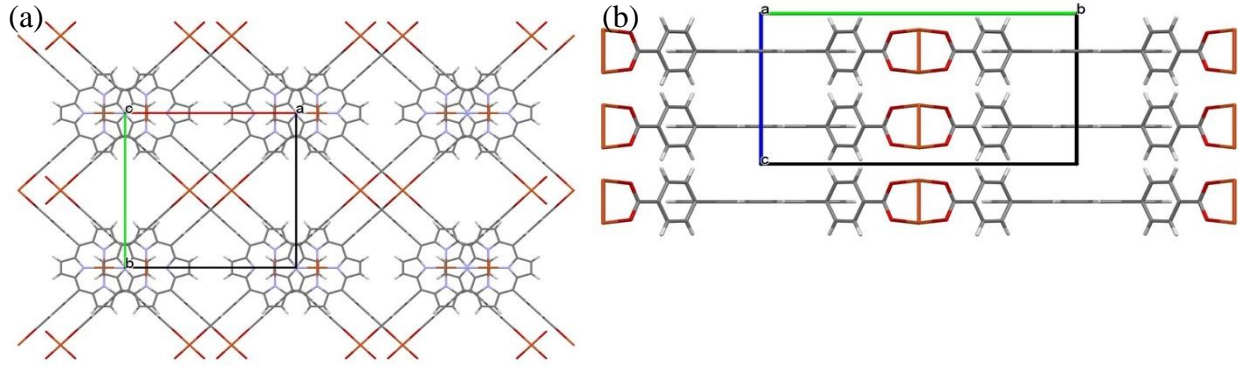


Figure 53 Projections of the expected crystal structure of the 2D MOF thin film (Exp A, S4) on the (a) ab plane, and (b) ac plane. C atoms are shown in gray, N atoms in purple, O atoms in red, and Cu atoms in orange. ($a = b = 16.27 \text{ \AA}$, and $c = 9.1 \text{ \AA}$)

5.4.4.2 Grazing-Incidence X-ray Scattering of 3D MOFs

The formation of 3D MOF thin films after nine deposition cycles can be observed from GIXS in Figure 54, in-plane peak diffractions are observed in Exp B, S2 and S3. Measurement on S2 was carried out on two different locations in and off the middle of the substrate as illustrated in the gold and green spectrum respectively, the resultant peak diffractions are orientation dependent because they show significant difference in diffraction patterns.

The dimensions of the tetragonal cell of Exp B, S2, are $a = b = 16.6 \text{ \AA}$, and $c = 13.39 \text{ \AA}$, and the space group is $P4/mmm$ (No. 123). Whereas, the dimensions of the tetragonal cell of S3 are $a = b = 16.6 \text{ \AA}$, and $c = 24.68 \text{ \AA}$. and the space group is $I4/mmm$. Exp B, S1, shows no significant in-plane diffractions because the fabricated film was measured after two deposition cycles, however, the film shows very broad out-of-plane diffraction peaks. The projections of expected crystal structures of 3D MOFs for Exp B, S2, and S3 are shown in Figure 55 and Figure 56 were generated based on the crystal data published[48] and agree well with unit cell parameters and the space groups used in GIXSUI.

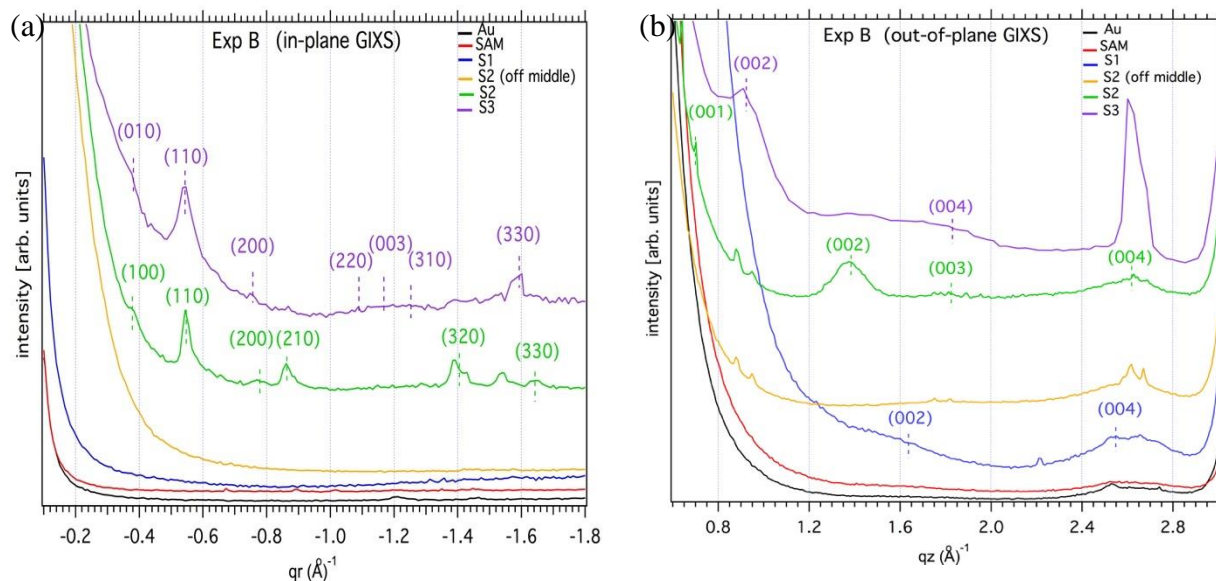


Figure 54 (a) Grazing-incidence (a) in-plane, and (b) out-of-plane X-ray scattering of 3D SURMOFs of Exp B, S1, S2, and S3. (wavelength= 1.1354 Å, incidence angle, $\alpha = 0.35^\circ$). Miller indices of the Bragg peaks are in order with scattering angle.

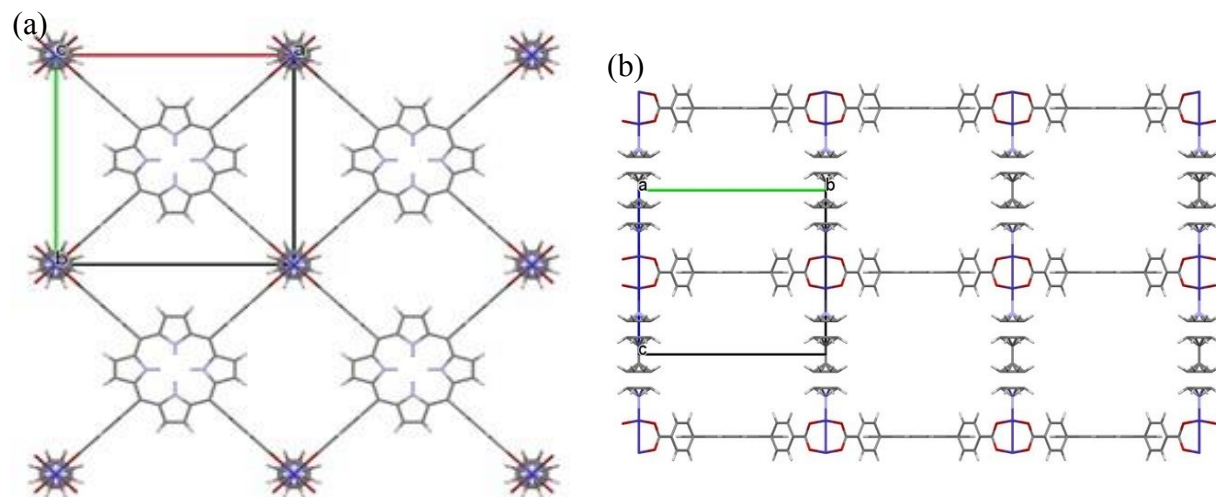


Figure 55 Projections of the expected crystal structure of the 3D MOF thin film (Exp B, S2) on the (a) ab plane, and (b) ac plane. C atoms are shown in gray, N atoms in purple, O atoms in red, and Cu atoms in orange. ($a = b = 16.6 \text{ \AA}$, and $c = 13.39 \text{ \AA}$)

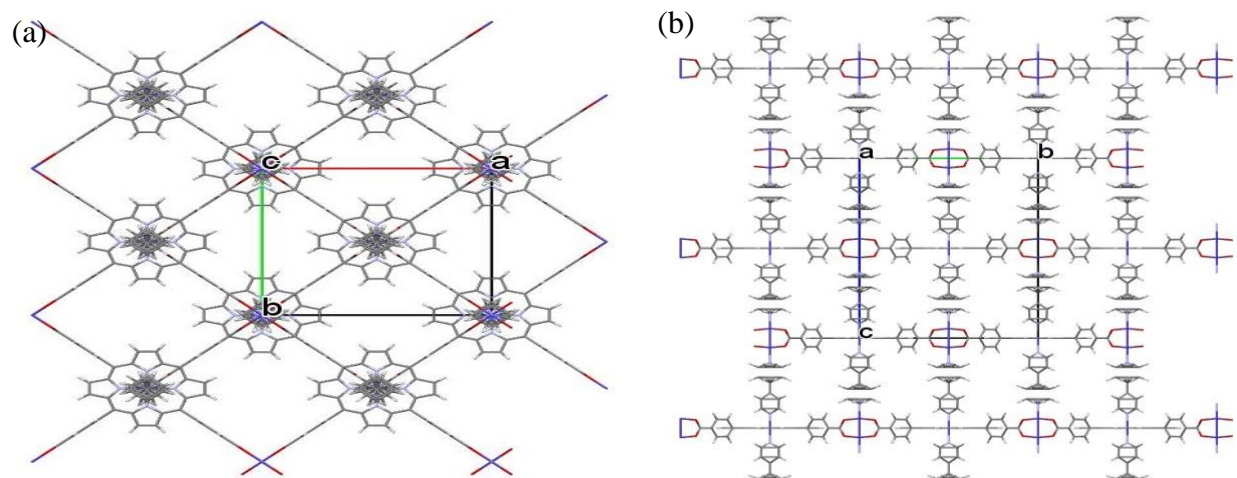


Figure 56 Projections of the expected crystal structure of the 3D MOF thin film (Exp B, S3) on the (a) ab plane, and (b) ac plane. C atoms are shown in gray, N atoms in purple, O atoms in red, and Cu atoms in orange. ($a = b = 16.6 \text{ \AA}$, and $c = 24.68 \text{ \AA}$)

5.5 Conclusion

Energy level alignments and modified interfacial electronic and chemical structures of MOF 2D- and 3D- thin films investigated successfully by direct and inverse PES system, delivering rich insights about their work functions, HOMO and LUMO levels, tunable transfer band gaps, interfacial dipoles, ionization potentials, and electron affinities. The surface, interfacial growth, and thicknesses of the fabricated thin films were confirmed by XPS. The results demonstrated transfer band gaps varied when the metals in the center of TCPP ring were changed in 2D MOF thin films. Tuning the bandgap was also feasible by incorporating and changing the length of the pillaring linker in 3D MOF thin films where a lengthier ligand produced a larger band gap. Thus, systematic electronic tunability via the core metalation of 2D SURMOF was observed, and incorporation of pillared linkers enabled to form the expected 3D SURMOF architectures with remarkable energy level alignments. Furthermore, the metalation provided an additional binding site to control the framework topology via axial ligations, and hence changed the electronic properties from p-type to n-type MOF film. Therefore, controlling the interfacial electronic

structures at the interface of SURMOF can remarkably help to develop and build molecular electronic junctions with enhanced performance, desired functionalities and behaviors is breakthrough for the next-generation molecular electronic materials and elaborated semiconductor technologies.

5.6 Acknowledgments

R.E. gratefully acknowledges the Dissertation Fellowship Award from University of South Florida. This research used of the Advanced Photon Source, a U.S. Department of Energy (DOE) office of Science by Argonne National Laboratory under Contract No. DE-AC02-06CH11357.

CHAPTER 6: CONCLUSIONS AND FUTURE OUTLOOK

6.1 Conclusions

This dissertation reports on direct and inverse PES studies on self-assembled 2D and 3D MOF thin films via sequential step-by-step incubation cycles on Au prefunctionalized surfaces. The resultant interfacial electronic structures of the fabricated films were obtained with their corresponding energy band diagrams which show band alignment phenomena due to the localization of charge density, and this represents unprecedented PES investigation on the conductive MOF thin films.

The orbitals line-up showed significant modifications of both hole and electron injection barriers of the MOF thin films grown on functionalized Au surfaces, and these properties at the interface are crucial to achieve efficient charge transfer. Hence, the successful PES measurements on porphyrin-based MOFs assessed the band alignment at the interface, and opened up an opportunity to design and develop further conductive MOF materials, and this can offer an important understanding for the foundation of molecular electronic heterojunctions and devices.

The growth of the MOF film components was determined by X-ray PES, GIXRD and GIXS. The UPS results revealed expected spectral features of the porphyrin MOF component. The combined results from the first onsets of UP- and IPE- spectra of 2D SURMOF revealed a transfer band gap which strongly agrees with the value obtained from DFT calculations as demonstrated in chapter 4.

The modifications of HOMO and LUMO energy levels along with other electronic structures of 2D and 3D SURMOF thin films are of significant novelty and impact due to

applications of electronically conductive MOF structures in electronic/optical devices as demonstrated in Chapter 5. MOF structures were self-assembled and tuned via the integration of organic ligands or pillaring linkers to have specific electronic or optical properties. The HOMO and LUMO energy levels and the correlated energy transfer band gaps were modified by the selection of free base and various metalloporphyrin derivatives, and this change is attributed to the porphyrin occupied and unoccupied molecular orbitals, and their redox state that are sensitive to the energy of 3d-orbitals of various core metals. The band banding of the HOMO and LUMO energy levels was due to the presence of the carrier concentration by dopants such as core metals or when pillaring linkers which were introduced with electron-donating abilities, therefore, there was a subsequent alignment of the energy levels upward or downward with respect to Fermi level.

According to the experimental transfer band gaps reported in chapter 4 and 5, can enable the materials to be suitable for optoelectronic applications which behave as semiconductor and undergo charge separation upon light excitation, and this is the hallmark of selective MOF component (i.e. organic ligand or pillaring linker) as semiconductor, and another (i.e. metal ion) that can behave simultaneously as an oxidizing or reducing agent.

The findings of this research promise the tailor-design of MOFs as electronic materials, promoting the fabricated SURMOF thin films to be favorable for electron or hole transport layers in energy harvesters such as Perovskite solar cells with the aim to enhance the power conversion efficiency, in energy storage systems such as conductive nanoporous electrodes for supercapacitors, as well as semiconductive MOF films as active materials in transistors and memristor devices.

6.2 Future Outlook

The conducted photoemission experiments on the self-assembled 2D and 3D MOF thin films revealed their physical electronic structure at the interface. The demonstrated HOMO and

LUMO energy level alignment phenomena at the MOF thin film interfaces achieved via judicious selection of organic conductive ligands and pillaring linkers. The study in this dissertation enables further research on electronic structure phenomena of other conductive and functional MOF films. An interesting extension of the research would be to study the incorporation of various metal ions and the insertion of anions or cations in the pores of the MOF film and reveal their resultant energy levels (i.e. band alignment phenomena) at their heterojunction interfaces, which is essential for devices and applications that require tunability while providing immediate impact to improve their overall performance.

REFERENCES

1. McKelvey, J.P., *Solid State Physics for Engineering and Materials Science*. 1993: Krieger Publishing Company.
2. Waldrop, M.M., *The chips are down for Moore's law*. *Nature*, 2016. **530**(7589): p. 144-7.
3. Cross, T., *AFTER MOORE'S LAW*, in *Economist*. 2016.
4. Kumar, S. *Fundamental Limits to Moore's Law*. 2015.
5. Markoff, J., *Smaller, Faster, Cheaper, Over: The Future of Computer Chips*, in *The New York Times*. 2015, A.G. Sulzberger.
6. Carroll, R.L. and B. Gorman Christopher, *The Genesis of Molecular Electronics*. *Angewandte Chemie International Edition*, 2002. **41**(23): p. 4378-4400.
7. Waser, R., *Nanoelectronics and information technology : advanced electronic materials and novel devices*. 2003, Weinheim: Wiley-VCH.
8. Reed, M.A. and J.M. Tour, *Computing with MOLECULES*. *Scientific American*, 2000. **282**(6): p. 86-93.
9. Joachim, C., J.K. Gimzewski, and A. Aviram, *Electronics using hybrid-molecular and mono-molecular devices*. *Nature*, 2000. **408**: p. 541.
10. Chen, J., et al., *Chapter 2 - Molecular Electronic Devices A2 - Morkoç, Hadis*, in *Advanced Semiconductor and Organic Nano-Techniques*. 2003, Academic Press: San Diego. p. 43-187.
11. Kuhn, H. and D. Möbius, *Systems of Monomolecular Layers—Assembling and Physico-Chemical Behavior*. *Angewandte Chemie International Edition in English*, 1971. **10**(9): p. 620-637.
12. Aviram, A. and M.A. Ratner, *Molecular rectifiers*. *Chemical Physics Letters*, 1974. **29**(2): p. 277-283.
13. Silvia, K., *Control of molecule-based transport for future molecular devices*. *Journal of Physics: Condensed Matter*, 2011. **23**(1): p. 013001.
14. Narayan, T.C., et al., *High Charge Mobility in a Tetrathiafulvalene-Based Microporous Metal–Organic Framework*. *Journal of the American Chemical Society*, 2012. **134**(31): p. 12932-12935.
15. Wu, G., et al., *Porous Field-Effect Transistors Based on a Semiconductive Metal–Organic Framework*. *Journal of the American Chemical Society*, 2017. **139**(4): p. 1360-1363.
16. Gu, Z.-G., et al., *Epitaxial Growth of MOF Thin Film for Modifying the Dielectric Layer in Organic Field-Effect Transistors*. *ACS Applied Materials & Interfaces*, 2017. **9**(8): p. 7259-7264.
17. Auwärter, W., et al., *Porphyryns at interfaces*. *Nat Chem*, 2015. **7**(2): p. 105-120.
18. Huh, S., S.-J. Kim, and Y. Kim, *Porphyrynic metal-organic frameworks from custom-designed porphyryns*. *CrystEngComm*, 2016. **18**(3): p. 345-368.
19. Hamad, S., et al., *Electronic structure of porphyryn-based metal-organic frameworks and their suitability for solar fuel production photocatalysis*. *Journal of Materials Chemistry A*, 2015. **3**(46): p. 23458-23465.

20. Love, J.C., et al., *Self-Assembled Monolayers of Thiolates on Metals as a Form of Nanotechnology*. Chemical Reviews, 2005. **105**(4): p. 1103-1170.
21. Gliemann, H. and C. Wöll, *Epitaxially grown metal-organic frameworks*. Materials Today, 2012. **15**(3): p. 110-116.
22. Hermes, S., et al., *Selective Nucleation and Growth of Metal–Organic Open Framework Thin Films on Patterned COOH/CF₃-Terminated Self-Assembled Monolayers on Au(111)*. Journal of the American Chemical Society, 2005. **127**(40): p. 13744-13745.
23. Biemmi, E., C. Scherb, and T. Bein, *Oriented Growth of the Metal Organic Framework Cu₃(BTC)₂(H₂O)₃·xH₂O Tunable with Functionalized Self-Assembled Monolayers*. Journal of the American Chemical Society, 2007. **129**(26): p. 8054-8055.
24. Li, J.-R., R.J. Kuppler, and H.-C. Zhou, *Selective gas adsorption and separation in metal-organic frameworks*. Chemical Society Reviews, 2009. **38**(5): p. 1477-1504.
25. Chae, H.K., et al., *A route to high surface area, porosity and inclusion of large molecules in crystals*. Nature, 2004. **427**: p. 523.
26. Long, J.R. and O.M. Yaghi, *The pervasive chemistry of metal-organic frameworks*. Chemical Society Reviews, 2009. **38**(5): p. 1213-1214.
27. Luo, J., et al., *Hydrogen Adsorption in a Highly Stable Porous Rare-Earth Metal-Organic Framework: Sorption Properties and Neutron Diffraction Studies*. Journal of the American Chemical Society, 2008. **130**(30): p. 9626-9627.
28. Suh, M.P., Y.E. Cheon, and E.Y. Lee, *Syntheses and functions of porous metallosupramolecular networks*. Coordination Chemistry Reviews, 2008. **252**(8): p. 1007-1026.
29. Desiraju Gautam, R., *Supramolecular Synthons in Crystal Engineering—A New Organic Synthesis*. Angewandte Chemie International Edition in English, 1995. **34**(21): p. 2311-2327.
30. Atwood, J.L. and J.M. Lehn, *Comprehensive supramolecular chemistry*. 1996, New York: Pergamon.
31. Lehn, J.M., *Supramolecular chemistry : concepts and perspectives : a personal account built upon the George Fisher Baker lectures in chemistry at Cornell University [and] Lezioni Lincee, Accademia nazionale dei Lincei, Roma*. 1995, Weinheim; New York: VCH.
32. Whitesides, G.M. and M. Boncheva, *Beyond molecules: Self-assembly of mesoscopic and macroscopic components*. Proceedings of the National Academy of Sciences, 2002. **99**(8): p. 4769.
33. Baker, H.R., E.G. Shafrin, and W.A. Zisman, *The Adsorption of Hydrophobic Monolayers of Carboxylic Acids*. The Journal of Physical Chemistry, 1952. **56**(3): p. 405-412.
34. Bigelow, W.C., D.L. Pickett, and W.A. Zisman, *Oleophobic monolayers: I. Films adsorbed from solution in non-polar liquids*. Journal of Colloid Science, 1946. **1**(6): p. 513-538.
35. Levine, O. and W.A. Zisman, *Physical Properties of Monolayers Adsorbed at the Solid–Air Interface. I. Friction and Wettability of Aliphatic Polar Compounds and Effect of Halogenation*. The Journal of Physical Chemistry, 1957. **61**(8): p. 1068-1077.
36. Sagiv, J., *Organized monolayers by adsorption. I. Formation and structure of oleophobic mixed monolayers on solid surfaces*. Journal of the American Chemical Society, 1980. **102**(1): p. 92-98.

37. Nuzzo, R.G. and D.L. Allara, *Adsorption of bifunctional organic disulfides on gold surfaces*. Journal of the American Chemical Society, 1983. **105**(13): p. 4481-4483.
38. Bain, C.D., et al., *Formation of monolayer films by the spontaneous assembly of organic thiols from solution onto gold*. Journal of the American Chemical Society, 1989. **111**(1): p. 321-335.
39. Ulman, A., *Formation and Structure of Self-Assembled Monolayers*. Chemical Reviews, 1996. **96**(4): p. 1533-1554.
40. Elzein, R., et al., *Advanced Photoemission Spectroscopy Investigations Correlated with DFT Calculations on the Self-Assembly of 2D Metal Organic Frameworks Nano Thin Films*. ACS Applied Materials & Interfaces, 2016. **8**(45): p. 31403-31412.
41. Shekhah, O., *Layer-by-Layer Method for the Synthesis and Growth of Surface Mounted Metal-Organic Frameworks (SURMOFs)*. Materials, 2010. **3**: p. 1302.
42. Zacher, D., et al., *Thin films of metal-organic frameworks*. Chemical Society Reviews, 2009. **38**(5): p. 1418-1429.
43. Seki, K., S. Takamizawa, and W. Mori, *Characterization of Microporous Copper(II) Dicarboxylates (Fumarate, Terephthalate, and trans-1,4-Cyclohexanedicarboxylate) by Gas Adsorption*. Chemistry Letters, 2001. **30**(2): p. 122-123.
44. Seki, K., S. Takamizawa, and W. Mori, *Design and Gas Adsorption Property of a Three-Dimensional Coordination Polymer with a Stable and Highly Porous Framework*. Chemistry Letters, 2001. **30**(4): p. 332-333.
45. Valentine, J.S., A.J. Silverstein, and Z.G. Soos, *Interdimer exchange in linear chain copper acetate-pyrazine*. Journal of the American Chemical Society, 1974. **96**(1): p. 97-103.
46. Morosin, B., R.C. Hughes, and Z.G. Soos, *Structural and e.p.r. search for exchange striction in pyrazine copper acetate*. Acta Crystallographica Section B, 1975. **31**(3): p. 762-770.
47. Koberl, M., et al., *From molecules to materials: Molecular paddle-wheel synthons of macromolecules, cage compounds and metal-organic frameworks*. Dalton Transactions, 2011. **40**(26): p. 6834-6859.
48. Choi, E.Y., et al., *Pillared porphyrin homologous series: intergrowth in metal-organic frameworks*. Inorg Chem, 2009. **48**(2): p. 426-8.
49. Shekhah, O., *Layer-by-Layer Method for the Synthesis and Growth of Surface Mounted Metal-Organic Frameworks (SURMOFs)* Materials, 2010. **3**: p. 1302.
50. So, M.C., et al., *Layer-by-Layer Fabrication of Oriented Porous Thin Films Based on Porphyrin-Containing Metal–Organic Frameworks*. Journal of the American Chemical Society, 2013. **135**(42): p. 15698-15701.
51. Stock, N. and S. Biswas, *Synthesis of Metal-Organic Frameworks (MOFs): Routes to Various MOF Topologies, Morphologies, and Composites*. Chemical Reviews, 2012. **112**(2): p. 933-969.
52. Deitch, R., *Molten metal solution growth*. Crystal Growth, 1975. **6**: p. 427.
53. Giess, E., et al., *2.6 Liquid-Phase Epitaxy*. Epitaxial growth, 1975: p. 183.
54. Konuma, M., *Feature and Mechanisms of Layer Growth in Liquid Phase Epitaxy of Semiconductor Materials*, in *Chemical Physics of Thin Film Deposition Processes for Micro- and Nano-Technologies*, Y. Pauleau, Editor. 2002, Springer Netherlands: Dordrecht. p. 43-68.
55. Hertz, H., *Ueber einen Einfluss des ultravioletten Lichtes auf die elektrische Entladung*. Annalen der Physik, 2006. **267**(8): p. 983-1000.

56. Bonzel, H.P. and C. Kleint, *On the history of photoemission*. Progress in Surface Science, 1995. **49**(2): p. 107-153.
57. Nordling, C., et al., *Possible finite nuclear size effect on the 279 keV transition in Tl203*. Nuclear Physics, 1956. **1**(5): p. 326-331.
58. Hüfner, S., *Introduction and Basic Principles*, in *Photoelectron Spectroscopy: Principles and Applications*. 2003, Springer Berlin Heidelberg: Berlin, Heidelberg. p. 1-60.
59. Piao, H. and N.S. McIntyre, *High-resolution valence band XPS studies of thin film Au–Al alloys*. Journal of Electron Spectroscopy and Related Phenomena, 2001. **119**(1): p. 29-33.
60. Zou, R.-Q., H. Sakurai, and Q. Xu, *Preparation, Adsorption Properties, and Catalytic Activity of 3D Porous Metal–Organic Frameworks Composed of Cubic Building Blocks and Alkali-Metal Ions*. Angewandte Chemie International Edition, 2006. **45**(16): p. 2542-2546.
61. Horcajada, P., et al., *Metal–Organic Frameworks as Efficient Materials for Drug Delivery*. Angewandte Chemie International Edition, 2006. **45**(36): p. 5974-5978.
62. Yoon, S.M., S.C. Warren, and B.A. Grzybowski, *Storage of Electrical Information in Metal–Organic-Framework Memristors*. Angewandte Chemie International Edition, 2014. **53**(17): p. 4437-4441.
63. Chua, L.O. and K. Sung Mo, *Memristive devices and systems*. Proceedings of the IEEE, 1976. **64**(2): p. 209-223.
64. Strukov, D.B., et al., *The missing memristor found*. Nature, 2008. **453**(7191): p. 80-83.
65. Wan, S., et al., *A Belt-Shaped, Blue Luminescent, and Semiconducting Covalent Organic Framework*. Angewandte Chemie, 2008. **120**(46): p. 8958-8962.
66. Wan, S., et al., *A Photoconductive Covalent Organic Framework: Self-Condensed Arene Cubes Composed of Eclipsed 2D Polypyrene Sheets for Photocurrent Generation*. Angewandte Chemie International Edition, 2009. **48**(30): p. 5439-5442.
67. Lukasczyk, T., et al., *Interaction of Cobalt(II) Tetraarylporphyrins with a Ag(111) Surface Studied with Photoelectron Spectroscopy*. The Journal of Physical Chemistry C, 2007. **111**(7): p. 3090-3098.
68. Rojas, G., *Self assembly and interface chemistry of non-metallated tetraphenyl porphyrin*, in *Department of Physics and Astronomy*. 2011, University of Nebraska-Lincoln.
69. He, C., et al., *Turn on fluorescence sensing of vapor phase electron donating amines via tetraphenylporphyrin or metallophenylporphyrin doped polyfluorene*. Chemical Communications, 2010. **46**(40): p. 7536-7538.
70. Wolak, M.u.A., et al., *Electronic Structure of Self-Assembled Peptide Nucleic Acid Thin Films*. The Journal of Physical Chemistry C, 2011. **115**(34): p. 17123-17135.
71. Wolak, M., *The Electronic Structure of Biomolecular Self-Assembled Monolayers*. 2012, University of South Florida.
72. Xu, G., et al., *Facile “Modular Assembly” for Fast Construction of a Highly Oriented Crystalline MOF Nanofilm*. Journal of the American Chemical Society, 2012. **134**(40): p. 16524-16527.
73. Seah, M.P. and D. Briggs, *Practical Surface Analysis: Auger and X-ray Photoelectron Spectroscopy*. 1990: John Wiley & Sons.
74. Manolova, M., et al., *Metal deposition onto thiol-covered gold: Platinum on a 4-mercaptopyridine SAM*. Surface science, 2005. **590**(2): p. 146-153.
75. Boeckl, M.S., et al., *Self-Assembly of Tetraphenylporphyrin Monolayers on Gold Substrates*. Langmuir, 2000. **16**(13): p. 5644-5653.

76. Bramblett, A.L., et al., *Determination of surface coverage for tetraphenylporphyrin monolayers using ultraviolet visible absorption and x-ray photoelectron spectroscopies*. Surface and Interface Analysis, 2002. **33**(6): p. 506-515.
77. *High Resolution XPS of Organic Polymers: The Scienta ESCA300 Database* (Beamson, G.; Briggs, D.). Journal of Chemical Education, 1993. **70**(1): p. A25.
78. Bai, Y., *Photoelectron Spectroscopic Investigations of Porphyrins and Phthalocyanines on Ag (111) and Au (111): Adsorption and Reactivity*. 2010, Friedrich-Alexander-Universität Erlangen-Nürnberg.
79. Pellegrino, G., et al., *Dye-Sensitizing of Self-Nanostructured Ti(:Zn)O₂/AZO Transparent Electrodes by Self-Assembly of 5,10,15,20-Tetrakis(4-carboxyphenyl)porphyrin*. The Journal of Physical Chemistry C, 2011. **115**(15): p. 7760-7767.
80. Li, Z., et al., *Measurement of the Internal Orbital Alignment of Oligothiophene-TiO₂ Nanoparticle Hybrids*. The Journal of Physical Chemistry C, 2013. **117**(27): p. 13961-13970.
81. Wiggins, B.C., *Structural and electronic properties of porphyrins and phthalocyanines self assembled on conductive surfaces*. 2013, Washington State University: Ann Arbor. p. 167.
82. Swadzba-Kwasny, M., et al., *Facile in situ synthesis of nanofluids based on ionic liquids and copper oxide clusters and nanoparticles*. Dalton Transactions, 2012. **41**(1): p. 219-227.
83. McIntyre, N.S. and M.G. Cook, *X-ray photoelectron studies on some oxides and hydroxides of cobalt, nickel, and copper*. Analytical Chemistry, 1975. **47**(13): p. 2208-2213.
84. Buchner, F., et al., *Coordination of Iron Atoms by Tetraphenylporphyrin Monolayers and Multilayers on Ag(111) and Formation of Iron-Tetraphenylporphyrin*. The Journal of Physical Chemistry C, 2008. **112**(39): p. 15458-15465.
85. Zeller, M.V. and R.G. Hayes, *X-ray photoelectron spectroscopic studies on the electronic structures of porphyrin and phthalocyanine compounds*. Journal of the American Chemical Society, 1973. **95**(12): p. 3855-3860.
86. Yi, Y., et al., *Characterization of indium tin oxide surfaces and interfaces using low intensity x-ray photoemission spectroscopy*. Journal of Applied Physics, 2006. **100**(9): p. 093719.
87. Schlaf, R., et al., *Organic semiconductor interfaces: Discrimination between charging and band bending related shifts in frontier orbital line-up measurements with photoemission spectroscopy*. Journal of Applied Physics, 1999. **86**(10): p. 5678-5686.
88. Rojas, G., et al., *Self-Assembly and Properties of Nonmetalated Tetraphenyl-Porphyrin on Metal Substrates*. The Journal of Physical Chemistry C, 2010. **114**(20): p. 9408-9415.
89. Nardi, M.V., et al., *Electronic properties of CuPc and H₂Pc: an experimental and theoretical study*. Physical Chemistry Chemical Physics, 2013. **15**(31): p. 12864-12881.
90. Coh, S., *Electronic structure and binding geometry of tetraphenylporphyrin-derived molecules adsorbed on metal and metal oxide surfaces*. 2012, Rutgers University-Graduate School-New Brunswick.
91. Koslowski, B., et al., *4-Mercaptopyridine on Au(111): a scanning tunneling microscopy and spectroscopy study*. Physical Chemistry Chemical Physics, 2011. **13**(9): p. 4045-4050.
92. Xu, G., et al., *Superprotonic Conductivity in a Highly Oriented Crystalline Metal–Organic Framework Nanofilm*. Journal of the American Chemical Society, 2013. **135**(20): p. 7438-7441.

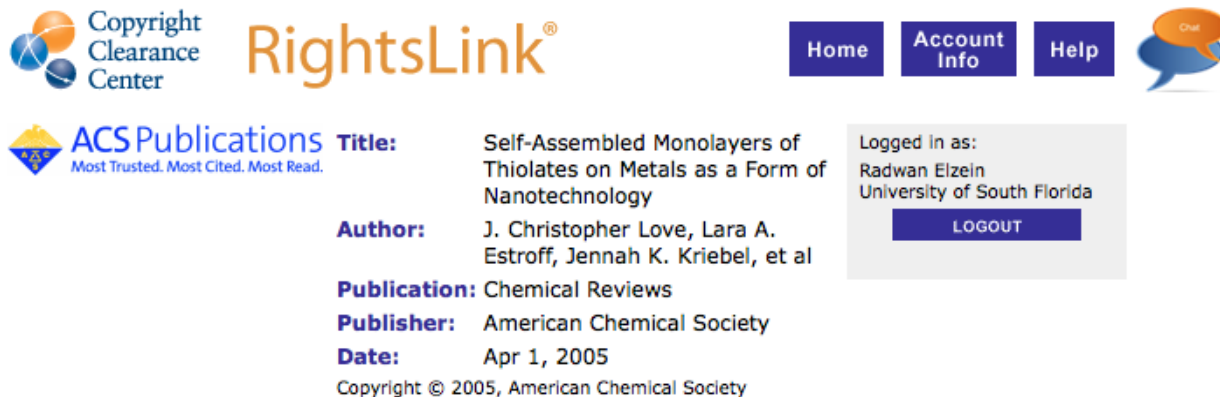
93. Hsu, S.-H., et al., *Platinum-Free Counter Electrode Comprised of Metal-Organic-Framework (MOF)-Derived Cobalt Sulfide Nanoparticles for Efficient Dye-Sensitized Solar Cells (DSSCs)*. 2014. **4**: p. 6983.
94. Lee, D.Y., et al., *Enhanced photovoltaic performance of Cu-based metal-organic frameworks sensitized solar cell by addition of carbon nanotubes*. 2014. **4**: p. 3930.
95. Lu, G. and J.T. Hupp, *Metal–Organic Frameworks as Sensors: A ZIF-8 Based Fabry–Pérot Device as a Selective Sensor for Chemical Vapors and Gases*. *Journal of the American Chemical Society*, 2010. **132**(23): p. 7832-7833.
96. Stassen, I., et al., *An updated roadmap for the integration of metal-organic frameworks with electronic devices and chemical sensors*. *Chemical Society Reviews*, 2017. **46**(11): p. 3185-3241.
97. Liu, J. and C. Woll, *Surface-supported metal-organic framework thin films: fabrication methods, applications, and challenges*. *Chemical Society Reviews*, 2017.
98. Wang, X., et al., *Structural, electronic and magnetic properties of metal-organic-framework perovskites [AmH][Mn(HCOO)3]: a first-principles study*. *RSC Advances*, 2016. **6**(54): p. 48779-48787.
99. Rogez, G., N. Viart, and M. Drillon, *Multiferroic Materials: The Attractive Approach of Metal–Organic Frameworks (MOFs)*. *Angewandte Chemie International Edition*, 2010. **49**(11): p. 1921-1923.
100. Wang, W., J.H. Alsmeier, and R. Schlaf, *Experimental Determination of the Charge Neutrality Level of Poly[2-methoxy-5-(2'-ethylhexyloxy)-p-phenylene vinylene] (MEH-PPV)*. *Langmuir*, 2013. **29**(21): p. 6341-6347.
101. Wang, W. and R. Schlaf, *Orbital line-up at poly[2-methoxy-5-(2'-ethylhexyloxy)-p-phenylene vinylene] (MEH-PPV)/poly(3-hexylthiophene) (P3HT) heterojunction*. *The Journal of Chemical Physics*, 2015. **142**(2): p. 024705.
102. Cascio, A.J., et al., *Investigation of a polythiophene interface using photoemission spectroscopy in combination with electrospray thin-film deposition*. *Applied Physics Letters*, 2006. **88**(6): p. 062104.
103. Magulick, J., et al., *Ionization Energy and Electronic Structure of Polycytidine*. *The Journal of Physical Chemistry B*, 2006. **110**(6): p. 2692-2699.
104. Magulick, J., M.M. Beerbom, and R. Schlaf, *Comparison of Ribonucleic Acid Homopolymer Ionization Energies and Charge Injection Barriers*. *The Journal of Physical Chemistry B*, 2006. **110**(32): p. 15973-15981.
105. Wolak, M.A., et al., *Electronic Structure of Self-Assembled Peptide Nucleic Acid Thin Films*. *The Journal of Physical Chemistry C*, 2011. **115**(34): p. 17123-17135.
106. Li, Z., et al., *Orbital alignment at the internal interface of arylthiol functionalized CdSe molecular hybrids*. *Journal of Applied Physics*, 2015. **117**(15): p. 155501.
107. Wang, Y.-Y., et al., *van der Waals Epitaxial Growth of 2D Metal–Porphyrin Framework Derived Thin Films for Dye-Sensitized Solar Cells*. *Advanced Materials Interfaces*. **0**(0): p. 1800985.
108. Bai, Y., et al., *Interfacial coordination interactions studied on cobalt octaethylporphyrin and cobalt tetraphenylporphyrin monolayers on Au(111)*. *Physical Chemistry Chemical Physics*, 2010. **12**(17): p. 4336-4344.
109. Bai, Y., *Photoelectron Spectroscopic Investigations of Porphyrins and Phthalocyanines on Ag(111) and Au(111): Adsorption and Reactivity*. 2010, Friedrich-Alexander-Universität Erlangen-Nürnberg (FAU).

110. Georey, R., *Self Assembly and Interface Chemistry of non-Metallated Tetraphenyl Porphyrin*, in *Physics and Astronomy*. 2011, University of Nebraska: Lincoln.
111. Coh, S., *Electronic structure and binding geometry of tetraphenylporphyrin-derived molecules adsorbed on metal and metal oxide surfaces*. 2012, Rutgers University.
112. Friesen, B.A., *An Investigation of Porphyrin Aggregation Using Spectroscopic and Microscopic Methods*, in *Department of Chemistry*. 2011, Washington State University. .
113. Liao, M.-S. and S. Scheiner, *Electronic structure and bonding in metal porphyrins, metal=Fe, Co, Ni, Cu, Zn*. *The Journal of Chemical Physics*, 2002. **117**(1): p. 205-219.
114. Clarke, S.E., C.C. Wamser, and H.E. Bell, *Aqueous Complexation Equilibria of meso-Tetrakis(4-carboxyphenyl)porphyrin with Viologens: Evidence for 1:1 and 1:2 Complexes and Induced Porphyrin Dimerization*. *The Journal of Physical Chemistry A*, 2002. **106**(13): p. 3235-3242.
115. Páez, C.A., et al., *Improvement in the methylene blue adsorption capacity and photocatalytic activity of H₂-reduced rutile-TiO₂ caused by Ni(II)porphyrin preadsorption*. *Applied Catalysis B: Environmental*, 2011. **106**(1): p. 220-227.
116. Safaei, E. and S. Mohebbi, *Photocatalytic activity of nanohybrid Co-TCPP@TiO₂/WO₃ in aerobic oxidation of alcohols under visible light*. *Journal of Materials Chemistry A*, 2016. **4**(10): p. 3933-3946.
117. Sonkar, P.K., et al., *Co(ii)-porphyrin-decorated carbon nanotubes as catalysts for oxygen reduction reactions: an approach for fuel cell improvement*. *Journal of Materials Chemistry A*, 2017. **5**(13): p. 6263-6276.
118. Tian, Y.-H. and M. Kertesz, *Low-Bandgap Pyrazine Polymers: Ladder-Type Connectivity by Intramolecular S...N(sp²) Interactions and Hydrogen Bonds*. *Macromolecules*, 2009. **42**(7): p. 2309-2312.
119. Sarkar, A. and S. Chakravorti, *Photophysics of phenyl pyridines and bipyridines in different media*. *Journal of Luminescence*, 1995. **65**(3): p. 163-168.
120. Shimin, H., et al., *First-principles calculation of the conductance of a single 4,4 bipyridine molecule*. *Nanotechnology*, 2005. **16**(2): p. 239.
121. Palmgren, P., et al., *Changing adsorption mode of FePc on TiO₂(110) by surface modification with bipyridine*. *The Journal of Chemical Physics*, 2008. **129**(7): p. 074707.
122. Gatzen, H.H., V. Saile, and J. Leuthold, *Deposition Technologies*, in *Micro and Nano Fabrication: Tools and Processes*, H.H. Gatzen, V. Saile, and J. Leuthold, Editors. 2015, Springer Berlin Heidelberg: Berlin, Heidelberg. p. 65-203.
123. Gu, Z.-G., et al., *Transparent films of metal-organic frameworks for optical applications*. *Microporous and Mesoporous Materials*, 2015. **211**(Supplement C): p. 82-87.
124. Ahvenniemi, E. and M. Karppinen, *In Situ Atomic/Molecular Layer-by-Layer Deposition of Inorganic–Organic Coordination Network Thin Films from Gaseous Precursors*. *Chemistry of Materials*, 2016. **28**(17): p. 6260-6265.
125. Beamson, G. and D. Briggs, *High Resolution XPS of Organic Polymers: The Scienta ESCA300 Database* *Journal of Chemical Education*, 1993. **70**(1): p. A25.
126. Eskelsen, J.R., et al., *Protonation state of core nitrogens in the meso-tetra(4-carboxyphenyl)porphyrin impacts the chemical and physical properties of nanostructures formed in acid solutions*. *Journal of Porphyrins and Phthalocyanines*, 2012. **16**(12): p. 1233-1243.

127. Yamashige, H., et al., *Local Structure of Nitrogen Atoms in a Porphine Ring of meso-Phenyl Substituted Porphyrin with an Electron-Withdrawing Group Using X-ray Photoelectron Spectroscopy and X-ray Absorption Spectroscopy*. Analytical Sciences, 2005. **21**(6): p. 635-639.
128. Watcharinyanon, S., et al., *Molecular orientation of thiol-derivatized tetraphenylporphyrin on gold studied by XPS and NEXAFS*. Surface Science, 2009. **603**(7): p. 1026-1033.
129. Niwa, Y., H. Kobayashi, and T. Tsuchiya, *X-ray photoelectron spectroscopy of tetraphenylporphyrin and phthalocyanine*. The Journal of Chemical Physics, 1974. **60**(3): p. 799-807.
130. Gottfried, J.M., et al., *Direct Synthesis of a Metalloporphyrin Complex on a Surface*. Journal of the American Chemical Society, 2006. **128**(17): p. 5644-5645.
131. Kretschmann, A., et al., *Tetraphenylporphyrin picks up zinc atoms from a silver surface*. Chemical Communications, 2007(6): p. 568-570.
132. Ghosh, A., et al., *Electronic Distinction between Porphyrins and Tetraazaporphyrins. Insights from X-Ray Photoelectron Spectra of Free Base Porphyrin, Porphyrazine, and Phthalocyanine Ligands*. Inorganic Chemistry, 1994. **33**(26): p. 6057-6060.
133. Makiura, R. and O. Konovalov, *Interfacial growth of large-area single-layer metal-organic framework nanosheets*. Scientific Reports, 2013. **3**: p. 2506.
134. Jiang, Z., *GIXSGUI: a MATLAB toolbox for grazing-incidence X-ray scattering data visualization and reduction, and indexing of buried three-dimensional periodic nanostructured films*. Journal of Applied Crystallography, 2015. **48**: p. 917-926.

APPENDIX A: COPYRIGHT PERMISSIONS

The permission below is for the use of material in Figure 1.



The screenshot shows the Copyright Clearance Center RightsLink interface. At the top left is the Copyright Clearance Center logo. To its right is the RightsLink logo. Further right are navigation buttons for Home, Account Info, and Help, along with a chat icon. Below the logos is the ACS Publications logo with the tagline "Most Trusted. Most Cited. Most Read." The main content area displays article details: Title: Self-Assembled Monolayers of Thiolates on Metals as a Form of Nanotechnology; Author: J. Christopher Love, Lara A. Estroff, Jennah K. Kriebel, et al; Publication: Chemical Reviews; Publisher: American Chemical Society; Date: Apr 1, 2005. A copyright notice for 2005, American Chemical Society is at the bottom. On the right, a user is logged in as Radwan Elzein from the University of South Florida, with a LOGOUT button.

PERMISSION/LICENSE IS GRANTED FOR YOUR ORDER AT NO CHARGE

This type of permission/license, instead of the standard Terms & Conditions, is sent to you because no fee is being charged for your order. Please note the following:

- Permission is granted for your request in both print and electronic formats, and translations.
- If figures and/or tables were requested, they may be adapted or used in part.
- Please print this page for your records and send a copy of it to your publisher/graduate school.
- Appropriate credit for the requested material should be given as follows: "Reprinted (adapted) with permission from (COMPLETE REFERENCE CITATION). Copyright (YEAR) American Chemical Society." Insert appropriate information in place of the capitalized words.
- One-time permission is granted only for the use specified in your request. No additional uses are granted (such as derivative works or other editions). For any other uses, please submit a new request.

If credit is given to another source for the material you requested, permission must be obtained from that source.

BACK

CLOSE WINDOW

Copyright © 2018 Copyright Clearance Center, Inc. All Rights Reserved. [Privacy statement](#). [Terms and Conditions](#).
Comments? We would like to hear from you. E-mail us at customercare@copyright.com

The permission below is for the use of material in Figure 2.



PLS clear permission request to use a Figure from an article

2 messages

Radwan Elzein <relzein@mail.usf.edu>
To: osama.shekhah@kaust.edu.sa

Dear Dr. Shekhah,

I would like to request a permission to use Figure 5 in my dissertation from the following article:

Osama Shekah, Layer-by-Layer Method for the Synthesis and Growth of Surface Mounted Metal-Organic Frameworks (SURMOFs), Materials 2010, 3(2), 1302-1315

Thank you for your consideration.

Sincerely,

Radwan

Radwan Elzein, MSc, MSEE
Doctoral Research Scholar

Electrical Engineering Department
University of South Florida,
Surface Science Laboratory
3720 Spectrum Blvd., IDRB, Suite 201
Tampa, FL 33620
Mobile: +1 (813) 898-7646
E-mail: relzein@mail.usf.edu

Osama Shekhah <Osama.Shekhah@kaust.edu.sa>
To: Radwan Elzein <relzein@mail.usf.edu>

Dear Radwan,
Thank you for citing my work
You have the permission to use it
Best regards
Osama

The permission below is for the use of material in Figure 3.



RightsLink®

Home

Account Info

Help



ACS Publications
Most Trusted. Most Cited. Most Read.

Title: Layer-by-Layer Fabrication of Oriented Porous Thin Films Based on Porphyrin-Containing Metal–Organic Frameworks
Author: Monica C. So, Shengye Jin, Ho-Jin Son, et al
Publication: Journal of the American Chemical Society
Publisher: American Chemical Society
Date: Oct 1, 2013
Copyright © 2013, American Chemical Society

Logged in as:
Radwan Elzeln
University of South Florida
Account #:
3001345674

LOGOUT

PERMISSION/LICENSE IS GRANTED FOR YOUR ORDER AT NO CHARGE

This type of permission/license, instead of the standard Terms & Conditions, is sent to you because no fee is being charged for your order. Please note the following:

- Permission is granted for your request in both print and electronic formats, and translations.
- If figures and/or tables were requested, they may be adapted or used in part.
- Please print this page for your records and send a copy of it to your publisher/graduate school.
- Appropriate credit for the requested material should be given as follows: "Reprinted (adapted) with permission from (COMPLETE REFERENCE CITATION). Copyright (YEAR) American Chemical Society." Insert appropriate information in place of the capitalized words.
- One-time permission is granted only for the use specified in your request. No additional uses are granted (such as derivative works or other editions). For any other uses, please submit a new request.

If credit is given to another source for the material you requested, permission must be obtained from that source.

BACK

CLOSE WINDOW

Copyright © 2018 Copyright Clearance Center, Inc. All Rights Reserved. [Privacy statement](#). [Terms and Conditions](#).
Comments? We would like to hear from you. E-mail us at customer care@copyright.com

The permission below is for the use of material in Figure 5 and Figure 8.

**Springer Science and Bus Media B V LICENSE
TERMS AND CONDITIONS**

Oct 08, 2018

This is a License Agreement between University of South Florida -- Radwan Elzein ("You") and Springer Science and Bus Media B V ("Springer Science and Bus Media B V") provided by Copyright Clearance Center ("CCC"). The license consists of your order details, the terms and conditions provided by Springer Science and Bus Media B V, and the payment terms and conditions.

All payments must be made in full to CCC. For payment instructions, please see information listed at the bottom of this form.

License Number	4444471475874
License date	Oct 08, 2018
Licensed content publisher	Springer Science and Bus Media B V
Licensed content title	Photoelectron spectroscopy : principles and applications
Licensed content date	Jan 1, 2003
Type of Use	Thesis/Dissertation
Requestor type	Academic institution
Format	Print, Electronic
Portion	chart/graph/table/figure
Number of charts/graphs/tables/figures	2
The requesting person/organization is:	Radwan Elzein/University of South Florida
Title or numeric reference of the portion(s)	Chapter 1 Figure 1.5., Chapter 1 Figure 1.11
Title of the article or chapter the portion is from	Introduction and Basic Principles
Editor of portion(s)	N/A
Author of portion(s)	N/A
Volume of serial or monograph.	N/A
Page range of the portion	Page 4, Page 9
Publication date of portion	2003
Rights for	Main product
Duration of use	Life of current edition
Creation of copies for the disabled	yes
With minor editing privileges	yes
For distribution to	Worldwide

The permission below is for the use of material in Chapter 4.



RightsLink®

Home

Account Info

Help



ACS Publications
Most Trusted. Most Cited. Most Read.

Title: Advanced Photoemission Spectroscopy Investigations Correlated with DFT Calculations on the Self-Assembly of 2D Metal Organic Frameworks Nano Thin Films

Author: Radwan Elzein, Chun-Min Chang, Inna Ponomareva, et al

Publication: Applied Materials

Publisher: American Chemical Society

Date: Nov 1, 2016

Copyright © 2016, American Chemical Society

Logged in as:
Radwan Elzein
University of South Florida

LOGOUT

PERMISSION/LICENSE IS GRANTED FOR YOUR ORDER AT NO CHARGE

This type of permission/license, instead of the standard Terms & Conditions, is sent to you because no fee is being charged for your order. Please note the following:

- Permission is granted for your request in both print and electronic formats, and translations.
- If figures and/or tables were requested, they may be adapted or used in part.
- Please print this page for your records and send a copy of it to your publisher/graduate school.
- Appropriate credit for the requested material should be given as follows: "Reprinted (adapted) with permission from (COMPLETE REFERENCE CITATION). Copyright (YEAR) American Chemical Society." Insert appropriate information in place of the capitalized words.
- One-time permission is granted only for the use specified in your request. No additional uses are granted (such as derivative works or other editions). For any other uses, please submit a new request.

BACK

CLOSE WINDOW

Copyright © 2018 Copyright Clearance Center, Inc. All Rights Reserved. [Privacy statement](#). [Terms and Conditions](#). Comments? We would like to hear from you. E-mail us at customercare@copyright.com